DISS. ETH NO. 22971

Spanning the unbridged imaging regime: Advances in mechanically detected MRI

A thesis submitted to attain the degree of

DOCTOR OF SCIENCES of ETH ZURICH

(Dr. sc. ETH Zurich)

presented by

Bradley Adam James Moores

M.Sc. in Physics, University of Waterloo

born on 21.10.1985

citizen of Canada

accepted on the recommendation of

Prof. Dr. Christian Degen, examiner

Prof. Dr. Martino Poggio, co-examiner

2015

Abstract

Nanoscale magnetic resonance imaging (nanoMRI) is a three-dimensional microscopy technique capable of resolving objects with nanometer spatial resolution. Advantages of nanoMRI include site-specific image contrasting, the absence of radiation damage, and the fact that only a single copy of an object is required. These qualities are particularly well-suited to provide structural information of large inhomogeneous systems, such as biomolecular complexes that are known to overwhelm nuclear magnetic resonance (NMR) spectroscopy and that evade crystallization for X-ray analysis.

A detection technique that has excelled in the development of nanoMRI is magnetic resonance force microscopy (MRFM). MRFM merges the high spatial resolution of scanning probe microscopy with the sensitive chemical spectroscopy of NMR. It consists of a sample attached to a soft mechanical cantilever ($\sim$200 μN/m), which is approached to within 100 nm of a nanoscale magnet in an external magnetic field ($>$2 T). A subset of nuclear spins within the sample are continuously inverted at the resonance frequency of the cantilever using adiabatic rapid passages. These inversions modulate the force between the cantilever and magnet with an amplitude given by the number of spins inverted. The cantilever deflection is read out by a laser interferometer, providing a direct measurement of the number of spins inverted.

In this thesis, we present a novel MRFM system design for nanoMRI imaging. Using this new probe design, we achieved imaging resolution of $\sim$4 nm. Furthermore, we measured sub-nanometer (0.6 nm) positional

accuracy owing to high stability and low mechanical noise. This is an essential prerequisite for imaging with sub-nanometer resolution.

We have also implemented several technical achievements that enabled new measurement types and improved imaging sensitivity. Among these advancements, we implemented a four-quadrant lock-in amplifier capable of detecting both the amplitude and phase of a statistically polarized nuclear spin signal. Using this technique, we developed a multiplexing method based on phase encoding for simultaneous acquisition of multiple spin signals. We demonstrated that the multiplexing technique can measure at least 6 signals simultaneously, either from different chemical species or different locations within the sample. Other technical advances include FPGA-based self-oscillation and feedback damping routines. We also tested several adiabatic inversion pulse types, and characterized their efficiency of inverting thin resonance slices, leading to improvements in nanoMRI resolution.

Several sample preparation techniques were explored in this work. This includes implementing a dysprosium nanomagnet that produced a field gradient on par with the best reported literature values. We developed a technique for attaching nanowires with diameters down to $60\,\mathrm{nm}$ onto the end of cantilevers. These hybrid sensors exhibited considerably lower non-contact friction compared to previous MRFM experiments. We also developed a platform for attaching biosamples to cantilevers using silicon nanorods formed with a focused ion beam. With this technique, we have detected nuclear spin signals from an Influenza virion, and are in the process of recording a full three-dimensional nano-MRI image of this medically important virus.

Zusammenfassung

Kernspintomographie im Nanometerbereich (nanoMRI) ist eine dreidimensionale Mikro-skopietechnik mit der Fähigkeit, Objekte mit einer Auflösung von wenigen Nanometern abzubilden. Die Vorteile von nanoMRI gegenüber anderen Technologien beinhalten ortsspezifischen Bildkontrast, die Abwesenheit von Strahlungsschäden und die Tatsache, dass nur eine einzelne Kopie eines Objektes benötigt wird. Diese Qualitäten sind besonders gut geeignet, um strukturelle Informationen über grosse, inhomogene Systeme zu liefern, welche bekanntermassen Kernspinresonanzspektroskopie (NMR) überfordern und sich nicht, wie für Röntgenstrahlenanalyse notwendig, als Kristall wachsen lassen.

Eine Detektionstechnik, die sich in der Entwicklung von nanoMRI besonders hervorgetan hat, ist Magnetresonanzkraftmikroskopie (MRFM). MRFM verbindet die hohe örtliche Auflösung von Rasterkraftmikroskopie mit der empfindlichen chemischen Spektroskopie von NMR. Eine Probe wird an der Spitze eines biegsamen mechanischen Cantilevers befestigt und innerhalb von 100nm an einen Nanomagneten in einem äusseren Magnetfeld herangefahren. Ein kleiner Teil der Kernspins im Sample wird mit Hilfe elektromagnetischer Pulse invertiert mit einer Rate, die der Resonanzfrequenz des Cantilevers entspricht. Diese Inversionen modulieren die Kraft zwischen dem Cantilever und den Nanomagneten mit einer Amplitude, die von der Anzahl Kernspins abhängt. Die Position des Cantilevers wird kontinuierlich mit einem Laserinterferometer ausgelesen, wodurch eine direkte Messung der Anzahl Spins möglich ist.

In dieser Dissertation präsentieren wir ein neuartiges MRFM-Design für nanoMRI. Mit diesem neuen Probendesign erreichen wir eine Bildauflösung

von ungefähr 4nm. Ausserdem messen wir eine Positionsgenauigkeit von 0.6nm dank hoher struktureller Stabilität und geringem mechanischen Rauschen. Diese Genauigkeit ist eine essentielle Voraussetzung, um Samples mit einer Auflösung von weniger als einem Nanometer abzubilden.

Wir haben auch verschiedene technische Errungenschaften implementiert, welche neue Messarten und bessere Bildempfindlichkeit erlauben. Zum Beispiel verwenden wir einen 4-Kanal Lock-in-Verstärker, um sowohl die Amplitude als auch die Phase eines statistisch polarisierten Spinsignals zu detektieren. Dank dieser Technik konnten wir eine Multiplexingmethode entwickeln, die auf der gleichzeitigen Messung verschiedener, phasen-kodierter Signale beruht. Wir haben demonstriert, dass die Multiplexingmethode mindestens 6 Signale gleichzeitig messen kann, die entweder von verschiedenen Elementen oder von unterschiedlichen Orten stammen. Zusätzliche technische Fortschritte beinhalten FPGA-basierte Eigenschwingung und Eigendämpfung mit einer Rückkopplungs-schlaufe. Wir haben auch verschiedene Inversionspulse getestet und ihre jeweilige Effizienz im Bereich sehr dünner Inversionsschichten charakterisiert, was zu verbesserter nano MRI-Auflösung führt.

Mehrere Sampleherstellungsmethoden wurden in dieser Arbeit erforscht. Unter anderem wurde ein Dysprosiummagnet verwendet, dessen Magnetfeldgradient den besten je gemessenen Werten entspricht. Wir entwickelten eine Methode, um Nanodrähte mit einem Durchmesser bis herunter zu 60nm an der Spitze eines Cantilevers anzubringen. Diese Hybridsensoren zeichnen sich durch stark verringerte kontaktlose Reibung aus im Gegensatz zu früheren MRFM-Messungen. Wir entwickelten auch eine Plattform, um Biosamples an Cantilevern zu befestigen mit Hilfe von Siliziumnanodrähten, die durch fokussierte Ionenstrahlen erzeugt wurden. Mit dieser Technik haben wir Kernspinsignale von einem Influenzavirus detektiert.

Mittlerweile sind wir dabei, ein dreidimensionales Bild dieses aus medizinischer Sicht so wichtigen Virus zu messen.

Acknowledgements

Contents

List of Figures

Abbreviations

AM	**A**mplitude **M**odulation
AFM	**A**tomic **F**orce **M**icroscopy
CT	**C**omputed **T**omography
FIB	**F**ocused **I**on **B**eam
FM	**F**requency **M**odulation
MRFM	**M**agnetic **R**esonance **F**orce **M**icroscopy
MRI	**M**agnetic **R**esonance **I**maging
NMR	**N**uclear **M**agnetic **R**esonance
NV	**N**itgroen **V**acancy
OCT	**O**ptically **C**omputed **T**omography
RF	**R**adio **F**requency
SEM	**S**canning **E**lectron **M**icroscopy
SNR	**S**ignal to **N**oise **R**atio
TMV	**T**obacco **M**osaic **V**irus

Physical Constants

Physical constant	Value	Description
$\frac{\gamma_e}{2\pi}$	$28024.95266(62)\,\text{MHz/T}$	Electron gyromagnetic ratio
$\frac{\gamma_n}{2\pi}$	$42.5774806(10)\,\text{MHz/T}$	Proton gyromagnetic ratio
μ_e	$9.2886 \cdot 10^{-24}\,\text{J/T}$	Electron magnetic moment
μ_p	$1.4112 \cdot 10^{-26}\,\text{J/T}$	Proton magnetic moment
$\hbar$	$1.05457 \cdot 10^{-34}\,\text{m}^2\text{kg/s}$	Planck's constant
k_B	$1.3806488 \cdot 10^{-23}\,\text{J/K}$	Boltzmann constant

Symbols

Symbol	Description
$\mathbf{A}$	Multiplexing phase encoding matrix
B_0	External magnetic field (T)
B_1	Radiofrequency magnetic field (T)
f_{center}	Adiabatic passage center frequency (Hz)
G	Magnetic field gradient from nanomagnet (T/m)
k	Cantilever spring constant (N/m)
m	Cantilever mass (kg)
N	Number of multiplexing pulses
p	Number of multiplexing phase slots
T_1	Spin lattice relaxation
T_P	Adiabatic passage pulse duration (s)
S_F	Spectral density (m^2/Hz)
Q	Quality factor
λ	Laser wavelength (1550 nm)
ν	Interferometer fringe visibility

Γ	Dissipation (kg/s)
Δf_{dev}	Adiabatic passage frequency deviation of (Hz)

Dedicated to my wife, Laken. . .

Chapter 1

Introduction

1.1 3D imaging methods

Several tomography methods have been developed for a wide range of biological imaging applications. Intense research has developed techniques for clinical use that tailor to resolving organs and tissues, such as computed tomography (CT), Optically computed tomography (OCT), and Magnetic resonance imaging (MRI). Several other techniques have remained mostly academic endeavours that are capable of resolving the location of atoms within biological structures down to sub-Angstrom resolution, including X-ray crystallography and Nuclear magnetic resonance (NMR).

Computed Tomography (CT) is well suited for 3D imaging inside the human body with approximately $1\,\mathrm{mm}$ resolution [1]. However, the method requires harmful radiation that can introduce hazardous consequences. Optically computed tomography (OCT) is a non-invasive technique for

imaging with resolution approaching $5\,\mu\mathrm{m}^3$, and imaging rates of 20,000-50,000 scans per second [2]. Despite this high resolution and speed, OCT is limited in applications due to its low penetration depth of only $2\,\mathrm{mm}$.

Magnetic resonance imaging (MRI) has become an essential diagnostic tool in clinical application for decades. It provides 3D structural [3] and functional [4] imaging with millimeter to submillimeter resolution. MRI can penetrate up to several meters, and does not require damaging radiation. Despite intense research efforts to improve the resolution, it still remains limited by detection sensitivity [5]. Consequently, the best MRI resolution has been fixed at approximately $40\ \mu\mathrm{m}^3$ for over a decade [6].

Outside of clinical environments, X-ray crystallography and Nuclear magnetic resonance spectroscopy (NMR) have become de facto techniques for resolving 3D structures. These methods are well suited for small proteins ($\sim 1\,\mathrm{nm}^3$), and can routinely obtain atomic resolution. X-ray crystallography has been used to determine nearly $100,000$ proteins structures, while NMR is responsible for just over $10,000$. However, larger structures such as transmembrane proteins tend to be challenging to crystallize. Furthermore, the complexity of these structures overwhelm both X-ray and NMR, inhibiting structure determination [7].

1.2   Unbridged imaging regime

The imaging resolutions of the methods described in the previous section are summarized in figure 1.1. These methods can be generally grouped into techniques that use light (CT, OCT and X-ray), electrons (electron microscopy), and nuclear magnetic resonance (NMR and MRI). Considering all the strengths and weaknesses of these methods, there is no general technique capable of 3-dimensionally resolving single $\sim 100\,\mathrm{nm}$ size
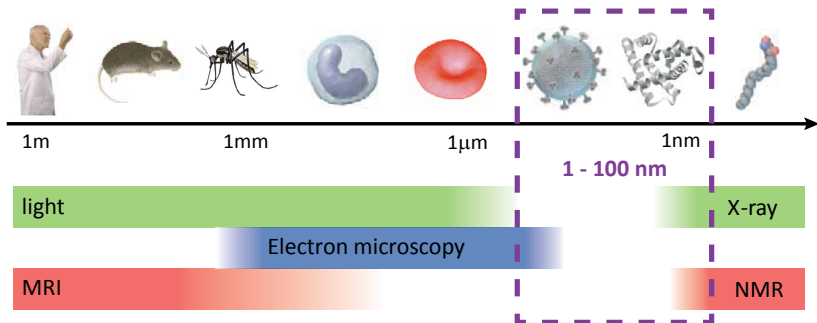
FIGURE 1.1: Imaging modalities according to resolution lengthscale. No method is capable of imaging between 1 and 100 nm, known as the unbridged imaging regime. In this work, we seek bridge the MRI and NMR gap with nanoMRI. Image adapted from [8].

objects with less than 5 nm resolution. This structure length scale is commonly referred to as the 'unbridged imaging regime' [8]. For this reason, there are many classes of structures that cannot be imaged, creating a blind spot for structural biologists. Several methods are under intense research and development to three-dimensionally resolve objects within this regime, including super-resolution microscopy, cryo-electron microscopy, and nanoMRI.

Super-resolution microscopy is a powerful technique owing to its simplicity. It relies on binding a fluorescent marker to a structure of interest, and using a laser source to activate the fluorescence [9]. The method has been used to image the interior of cells with sub-optical wavelength resolution. However, the fluorescent markers are bulky (~ 2 nm), and consequently modify the structure of the object being imaged. These structural changes are less significant for lower resolution imaging, but greatly hinder high resolution microscopy.

Cryo-electron microscopy has also received a lot of attention, and has

been shown to resolve objects on the order of several nanometers [10]. This method requires focusing high energy electron beams down to several nanometers, and consequently damages the object being imaged. In order to mitigate the destructive nature of these methods and obtain a sufficiently high signal-to-noise ratio (SNR), typically $10,000$ to $100,000$ copies of an object are imaged [11]. The structure is determined from computational reconstruction using the ensemble of measurements [12]. Although impressive resolution has been demonstrated with this technique, the validity of the determined structure is unclear due to averaging over a statistical ensemble. This is particularly an issue with large molecular complexes, where the sample density varies between copies of an object.

1.3   NanoMRI

Nanoscale magnetic resonance imaging (nanoMRI) is a promising, yet challenging microscopy technique for three-dimensionally imaging with nanometer spatial resolution [13–15]. The method has the potential to provide structural information of large biomolecular complexes that are known to overwhelm nuclear magnetic resonance (NMR) spectroscopy and that evade crystallization for X-ray analysis. Among the advantages of nanoMRI are the possibility of site-specific image contrast, the absence of radiation damage, and the fact that only a single copy of an object is required. Recent proof-of-concept experiments showed that nanoMRI is capable of 3D imaging individual virus particles at $\sim$10 nm spatial resolution [16] and isotope-specific image contrast [17], with a detection sensitivity between 10^1 to 10^4 statistically polarized nuclear spins [18–21].

High resolution MRI images can be recorded with several methods including coils/microcoils, Nitrogen vacancy (NV) centers, and mechanical resonators. Presently, the best MRI resolution has been obtained by mechanical detection of magnetic resonance, known as Magnetic Resonance Force Microscopy [22].

1.3.1   Coils and microcoils

Conventional MRI systems have become an essential diagnostic tool in hospital settings. However, despite extensive research since its conception, the imaging resolution of these systems have been limited to $> 40 \, \mu m^3$.

The spatial resolution of coil based MRI (LC electrical circuits) is directly dependent on SNR. The sensitivity of inductive coils is improved with decreasing diameters [23]. Additionally, SNR is improved by maximizing the filling ratio of the sample and coil, and therefore high spatial resolution favours smaller coil designs. However, the miniaturization of coils becomes very difficult when the diameter becomes comparable to the wire thickness. For this reason, coils have been limited to diameters of approximately 20 to $50 \, \mu m$ [7]. Lithographically defined coils have been demonstrated as a means of overcoming the wire width limitations [24, 25]. However, despite intense efforts, the best resolution reported with coils has been limited to a few microns [6, 26–29].

1.3.2   Mechanical detection

The concept of mechanically detecting magnetic resonance signals was first envisioned as a means of overcoming the limitations of coils and microcoils [13]. Instead of detecting oscillating flux with an inductive coil, mechanical

detection measures the force produced by nuclear spins within a magnetic field gradient. The spins are inverted at the resonance frequency of a very soft cantilever.

The SNR of both inductive coils and mechanical oscillators can be described by the same relationship

$$SNR \propto \sqrt{\frac{\omega_0 Q}{k_m}}$$

where ω_0 is the angular frequency of spin inversions, Q is the quality factor, and k_m is the spring constant response to a magnetic field [30].

An inductive coil achieves high SNR by operating at high frequencies, which is dependent on the magnetic field strength (between 0.1 and 1 GHz). Intense research efforts have improved field strengths, but development has plateaued in recent years [23]. Conversely, cantilevers are typically fabricated with low resonance frequencies (between 5 and 100 kHz).

The quality factors of inductive coils are generally low, on the order of $\sim$100 [30]. In comparison, cantilevers fabricated from single crystal silicon have Q factors up to 70, 000. Furthermore, our recent work has even demonstrated that single crystal electronic grade diamond cantilevers can have Q factors as high as 6 million [31].

The response of a coil to a magnetic field can be formulated in terms of a spring constant

$$k_{mag} = \frac{L}{|B_1|^2} = \frac{2V_{coil}}{\mu_0}$$

where B_1 is the RF power, L is the inductance, and V_{coil} is the volume [30]. For example, a microcoil consisting of four-turns with 1.8 mm, and 3 mm long would have a magnetic spring constant of $k_{mag} = 1.2 \cdot 10^{-2}$ J/T^2 [30]. In contrast, cantilevers can be fabricated with very low spring constants.

For instance, recent MRFM cantilevers have achieved mechanical values as low as $k_{mech} = 5 \cdot 10^{-5}$ N/m. The response of such a cantilever to a magnetic field is dependent on the local field gradient G

$$k_{mag} = \frac{k_{mech}}{G^2}$$

Field gradients have been demonstrated as high as $5 \cdot 10^6$ T/m, corresponding to $k_{mag} = 2 \cdot 10^{-18}$ J/T^2 for cantilevers.

This large difference in k_{mag} between coils and cantilevers corresponds to how each responds to a magnetic field. A mechanical resonator is displaced by the magnetic field force, whereas a field creates and annihilates current within a coil twice per oscillation cycle [30]. Each creation and annihilation of current has a corresponding irreversible energy loss proportional to the coil volume. Conversely, a cantilever converts the magnetic force to kinetic energy which is dissipated slowly according to the Q factor [30].

1.3.3 Nitrogen vacancy center

The Nitrogen Vacancy (NV) center has recently received a lot of attention as an NMR sensor. The NV center is composed of a nitrogen atom adjacent to a vacancy within a diamond lattice, which collectively acts as a single spin-1 defect. The quantum state of the NV center can be optically initialized and read-out using a green laser (532 nm). The NV center has been demonstrated to have a very high sensitivity to fluctuating magnetic fields (10 nT/$\sqrt{\text{Hz}}$), owing to its long coherence time. However, this long coherence is only exhibited by NV centers that are deep within the diamond lattice (> 5 nm). The ability of the NV to detect a nuclear spin depends on the relative separation through the dipole-dipole interaction, or $\propto r^3$, where r is the separation of the NV and nuclear spin. For this reason,

detecting nuclear spins requires shallow NV centers, which also decreases the NV coherence time and consequently diminishes the sensitivity.

Despite these demanding pre-requisites for signal detection, impressive progress has been made with nuclei detection. Several results have detected nuclear spin volumes of approximately $(5 \, \text{nm})^3$ nuclear spins [18–20]. Two dimensional nuclear spin data has been obtained [32], and a field gradient has been shown to encode multiple electron spins [33]. However, the method has not been demonstrated capable of imaging 3D structures, and it is unclear whether the demanding sample preparation can be overcome. Furthermore, even a shallow NV center with a long coherence time is only capable of detecting local magnetic fields, thus prohibiting depth resolution beyond a few nanometers. Consequently, no proposals have suggested how this method may be used to image within the unbridged regime.

1.4 Roadmap to atomic resolution

Imaging large three-dimensional objects with near-atomic-resolution is a difficult challenge, but such a tool would vastly aid many branches of science and technology, especially biology. Some examples of these structures include molecular machines, transmembrane proteins, viruses, and bacteria. X-ray crystallography and NMR spectroscopy are very powerful imaging techniques with sub-Angstrom resolution in this regime. However, these methods are typically limited to a subset of structures smaller than $\sim 1 \, \text{nm}$.

It was recently demonstrated that $\sim 5 \, \text{nm}$ resolution nanoMRI can be imaged with MRFM [22]. With improvements in sensitivity, this method should be capable of imaging with $1 \, \text{nm}$ resolution, corresponding to a

detection volume of approximately 50 nuclear spins. This means that the signal to noise ratio must be improved by nearly three orders of magnitude to achieve this goal.

Figure 1.2 shows a proposed scheme, consisting of two parallel strategies, aiming to atomically resolve large molecular complexes with nano-MRI. This proposal has served as a basic motivation for this thesis. The first approach is to detect chemically contrasted quaternary structures by introducing isotopic labels. Such contrast provides information about repeating unit cells, and would reveal structural organization. The second strategy aims to improve the sensitivity of MRFM to achieve 1 nm imaging resolution. Combining both strategies would provide sufficient information to fit atomically resolved sub-unit structures from X-ray and NMR data. Collectively, this strategy would provide atomically resolved three dimensional models of samples larger than 1 nm. In this thesis, we will present our steps toward fulfilling this goal. We developed a signal multiplexing technique that solves the contrasting strategy. Additionally, we present our steps toward achieving 1 nm resolution by optimizing all aspects of imaging, including an improved MRFM probe, optimally designed pulses, and improved sample preparation.

1.5   Outline of this thesis

This thesis is divided into 7 chapters:

- **Chapter 2** presents the design and construction of a novel MRFM probe for nanoMRI. This includes the instrumentation design, vibration isolation, low temperature aspects, and interferometer.
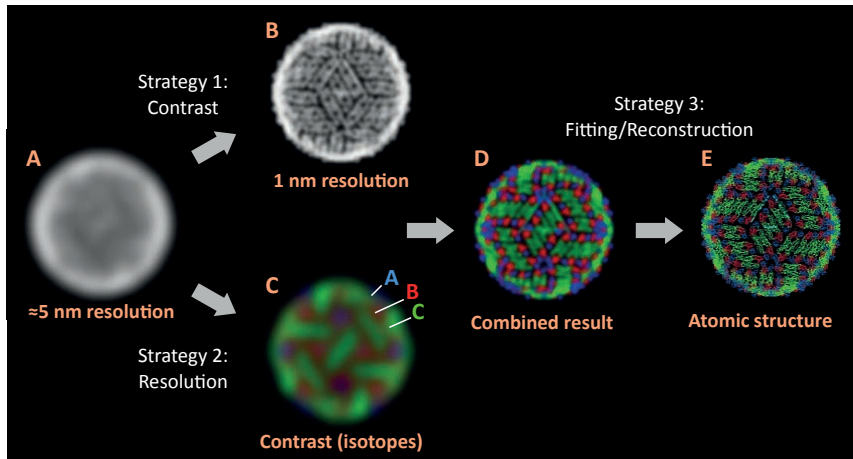
FIGURE 1.2: A proposed roadmap to achieve atomic resolution with MRFM. (a) The current state of the art imaging resolution is approximately 5 nm. (b) By improving the sensitivity of the technique, 1 nm resolution should be achievable. (c) In the past, MRFM has relied on long averaging time in order to achieve high spatial resolution. For this reason, recording a signal from several isotopes has been precluded. Chemical contrast would provide structural information from repeating patterns of substructures. (d) Combining higher resolution with chemical contrast data would provide an image that could have atomically known structures computationally fit, (e) which in turn would allow for atomically known structures to be inferred.

- **Chapter 3** introduces the ultrasensitive cantilevers used in this work. The mechanical properties, dissipation channels, and feedback circuits will be presented. We will describe the design considerations for nuclear spin detection, and how we obtain topographical images of the tip and surface.

- **Chapter 4** describes the radiofrequency pulses used in this work for inverting nuclear spins. NMR theory, MRFM spin detection, and the signal detection pathway will be introduced. Numerical simulations are presented that are in agreement with the acquired data.

- **Chapter 5** introduces a multiplexing method used to record several statistically polarized nuclear spin signals simultaneously. This phase encoding method allows for faster acquisition times of multiple isotopes or locations within a sample.

- **Chapter 6** describes an attempt of imaging a single influenza virus. The early work towards obtaining an image is presented such as sample preparation, topographical imaging of viruses, and preliminary MRFM results. This acquisition is ongoing during the writing of this thesis.

- **Chapter 7** concludes by stating the main advances of the MRFM field during this work.

Chapter 2

Instrumentation

This chapter presents the design and construction of the MRFM system built in this work.

2.1   Introduction

In this work, we have designed, built, and operated a novel MRFM based on a system originally designed by the IBM group [22]. Figure 2.1a shows a schematic representation of the measurement configuration. The system uses a cantilever in a pendulum geometry, with a non-magnetic sample attached to the unclamped end. The cantilever is approached to within 100 nm of a magnetic pillar that is on top of a gold stripline. The pillar produces a magnetic field gradient that permeates through the sample, and produces a static force on the cantilever due to the polarization of nuclear spins in the sample. This force can be alternated at the cantilever resonance frequency by inverting the sample's nuclear spins at twice the
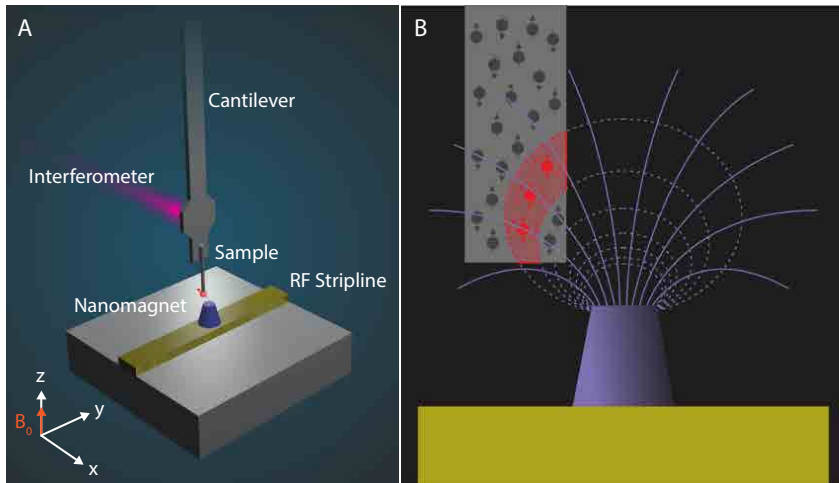
FIGURE 2.1: (a) Schematic representation of an MRFM cantilever positioned over a cone-shaped nanomagnet, located on top of a gold stripline. An interferometer measures the cantilever deflection. The measurement is performed in an external magnetic field B_0. (b) The magnetic field gradient produced by the nanomagnet creates a distribution of Larmor frequencies within the sample. Radiofrequency pulses are applied using the stripline, which selectively invert a subset of nuclear spins (depicted in red) within the sample.

oscillation period. The force is proportional to both the gradient and the square root of the number of spins flipped. The magnetic field gradient also creates a distribution of Larmor frequencies within the sample, as shown in figure 2.1b. This enables the ability to selectively invert spins according to their Larmor frequency, which is the central concept of MRI. By inverting only a subset of the sample, the nuclear spin density can be measured as a function of position, providing a means of three-dimensionally resolving a sample.

FIGURE 2.2: Photo of the 4 Kelvin MRFM system built in this work: a cryostat is on the right, and the electronics rack is on the left. The dewar is suspended by a pneumatic suspension that decouples the system from room vibrations.

2.2 System design

Figure 2.2 shows a photo of the MRFM system and the electronics rack built in this work. A schematic representation of the system is shown in figure 2.3a. A Cryomagnetics helium dewar was supported on a three-legged TMC optical table. The dewar consists of a liquid helium holding chamber, and an outer liquid nitrogen jacket. The jacket and inner chamber were thermally coupled such that the nitrogen jacket could be filled to pre-cool the inner chamber to ~120 K. The helium hold time was approximately 8 days with the nitrogen jacket, and the boiled off helium was collected with an in-house recovery system.
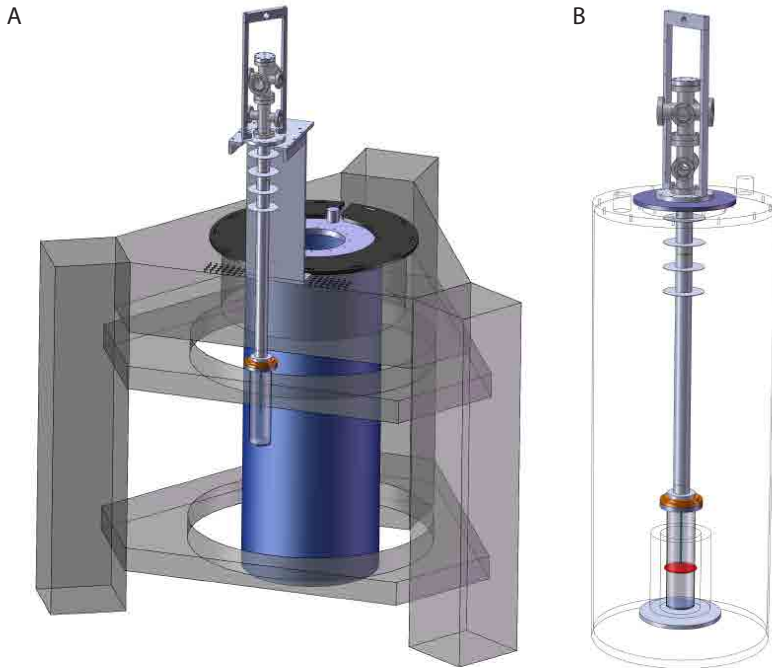
FIGURE 2.3: (a) Schematic of the MRFM system built in this work. The table was a tripod with pneumatic pistons to raise and lower the dewar. The MRFM insert is shown on a stand, where it was positioned when worked on. (b) Schematic of the insert placed inside the dewar. A red disk at the bottom indicates the position of the MRFM probe. The probe was thermally anchored to the copper flange with braids also made of copper.

The cryostat insert consists of a long vacuum chamber that leads to the MRFM probe at the lower end, where the cantilever and nanomagnet were located. The cryostat insert is shown in figure 2.3a on a support stand, where it sits when worked on outside the dewar. The support positioned the end of the insert at desk level for convenient access to the MRFM probe. Photos of the probe are shown in figure 2.4. The insert was closed
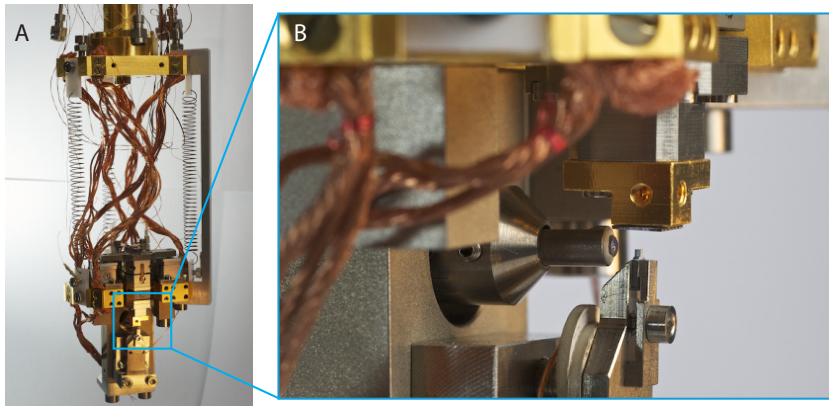
FIGURE 2.4: (a) The MRFM probe consisting of an upper and lower triangular platform. The upper triangular piece is fixed to the rest of the system, and holds wiring feed-throughs. The lower triangle contains all the measurement components. The two triangular pieces are thermally coupled with copper braids, and mechanically coupled with springs. The springs vibrationally isolate the lower triangle from the rest of the system. A bracket on the right fixes the triangles together when the probe is being worked on, and is removed during measurements. (b) A zoomed in photo of the cantilever chip, laser interferometer lens, and sample stage supported by a stack of attocubes. The cantilever chip is clamped by titanium pieces, and is directly connected to two piezo disks for mechanical feedback. Photos taken by H. Hostettler.

with a can that raised over the probe, up to a copper flange. Between the can and flange was a ring of kapton polyimide film to serve as a gasket. The flange was tightly sealed with 12 stainless steel screws. Four teflon half-cones were screwed onto the flange to help direct the insert into the dewar. A turbo-pump (Pfeiffer Vacuum HiCube) was connected with a KF bellows to a valve located at the top of the insert.

The insert was pre-cooled by raising a liquid nitrogen dewar around the can for ~ 4 hours prior to moving into the cryostat. The insert was raised with a crane attached to the ceiling, and lowered into the dewar. Figure

2.3b shows the final position of the insert within the dewar. Four heat shields near the top of the dewar lined up with four disks on the insert. The MRFM probe was located in the center of a superconducting magnet, depicted with a red bar. The magnet was capable of operating up to 6 Tesla, and was uniform over 10 cm.

2.3 MRFM probe

We designed the MRFM probe such that the cantilever and interferometer remained fixed with respect to each other, while the stripline/nanomagnet could be moved in 3-dimensions around the cantilever. Figure 2.5a shows a schematic representation of the positioning system. The probe consists of an attocube nano-positioning stack suspended over a cantilever, with the interferometer in behind. Two RF semi-rigid coax lines were fixed by a copper holder on the left side. The attocube stack was fixed to a copper triangular base plate that was gold plated to prevent oxidation. Nearly all other components were fabricated from titanium to decrease relative thermal contraction during cooldown.

The stripline chip was fixed with Torrseal glue to a gold plated (copper) sample holder. Flexible copper leads electrically contacted the stripline with indium, and electrical caps were soldered to the opposite sides of the leads. The conductors within the semi-rigid lines were exposed, and the caps were crimped before sliding onto the conductor. RF transmission for 10 MHz was ∼50% and dropped to ∼30% at 100 MHz.

The sample holder was fixed to a titanium extension with brass screws. This extension piece attached to an open loop Attocube ANSxy50 XY stage (blue). The XY stage could scan up to $30 \times 30~\mu m^2$ at room temperature, but the range was reduced to $12 \times 12~\mu m^2$ at 4.2 K. The XY
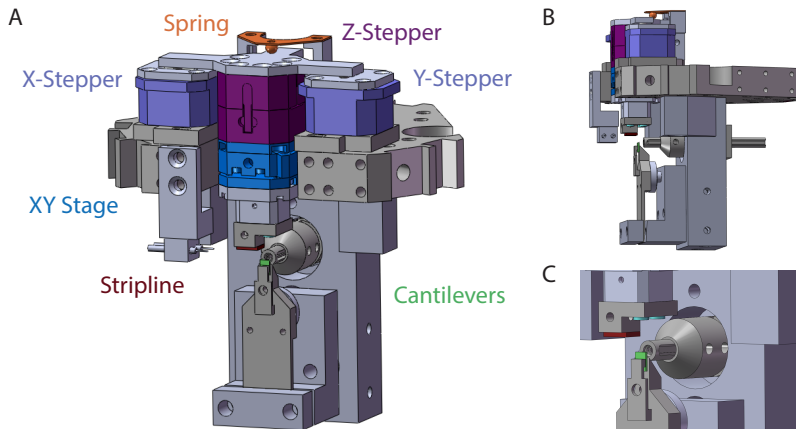
FIGURE 2.5: (a) Schematic representation of the Attocube position-
ers used to move the stripline in 3-dimensions around the stationary
cantilever. (b) Side projection. (c) Zoom in of the stripline plate,
cantilevers, and lens.

stage was fixed to an Attocube ANPz51 (purple). This Z-positioner could
be used as a stepper with a travel range up to $2.5\,\mathrm{mm}$. It could also be
used to finely position the height with a DC voltage, and had a range up
to $5\,\mu\mathrm{m}$ at room temperature, and $800\,\mathrm{nm}$ at $4.2\,\mathrm{K}$.

The center Attocube stack was hung with a titanium bridge over two
Attocube ANPx51 stick-slip positioners. One positioner stepped along the
X-axis, while the other moved along the Y-axis. Each had a travel range of
$3\,\mathrm{mm}$. Sapphire spheres were attached under the left and right sides of the
bridge with Torrseal glue. These spheres sat inside grooves on titanium
pieces attached to the X and Y-steppers. A spring made of beryllium
copper applied a downward force on the bridge and kept it fixed against
the X and Y Attocubes. A Sapphire sphere is glued (with Torrseal) to the
spring that contacts the bridge.

2.4 Vibration isolation

Pneumatic pistons were placed between the table legs and the optical table, providing a means of isolating the dewar from room vibrations. The pistons could be independently raised and lowered to tilt the table by a small angle in any direction. The system was operated in the basement, within a vibrationally isolated room.

The vacuum pump was mechanically decoupled from the system by sitting on a table attached to the wall. The bellows between the pump and MRFM was connected through two 40 kg brass plates to damp vibrations.

The MRFM probe was mechanically isolated from the rest of the insert with three springs, as shown in figure 2.4a. A 'touch sensor' was placed at each of the three corners of the lower triangular base plate. Each sensor corresponds to a screw with an electrical lead that applied ∼2.7 V. If the screw touched the cryostat insert sidewall, then it completed a circuit that turned on an LED indicator. The tilt of the table was adjusted until the probe hung without contacting the sidewalls.

2.5 Low temperature

Working at low temperatures significantly improves measurement stability. Room temperature AFM systems suffer from thermal drift, which causes the cantilever and surface to move relative to each other. These fluctuations can be on both short and long time scales, causing spatial drift to distort individual images. Operating at low temperatures is a way to reduce this drifting issue.

Decreasing the temperature of silicon cantilevers significantly improves the minimum detectable force. One factor is the reduced thermal noise which consequently decreases the vibration amplitude. Previous work has also demonstrated that low temperatures improve the mechanical quality factor of single crystal silicon cantilevers [34]. At room temperature, these cantilevers have quality factors in the range of 5,000 to 10,000, but typically improve to 50,000 to 70,000 at 4 K. It was found that a high room temperature Q factor is typically indicative of a high base temperature Q factor, and vice versa.

Proper thermal anchoring is imperative for the mechanical sensor and surface to operate at low temperatures. Copper braids were tightly screwed from the lower triangle to positions close to the stripline surface and cantilever. Additionally, all pieces (other than the sample holder) were fabricated from titanium to reduce relative thermal expansion/compression between components.

2.6   Experimental conditions

Our MRFM operates at a pressure of $<10^{-6}$ mbar and at a temperature of 4 K. All components shown in figure 2.4 are mounted on a sample plate and suspended on soft springs inside a ^{4}He cryostat. An optical fiber is fixed with respect to the cantilever, while the position of the magnet and the stripline can be controlled via an attocube micropositioner. The laser has a wavelength of 1550 nm and an intensity of 100 nW. An interferometer forms between the end of the optical fiber and the cantilever. The fiber is coated with a thin film ($\sim$50 nm) of silicon to give it a reflectivity of about 50%. The cantilever has an estimated spring constant of $2.5 \cdot 10^{-4}$ N/m and a resonance frequency close to 5 kHz. Its mechanical quality factor

drops from $70,000$ to about $30,000$ when it is brought to within $100\,\mathrm{nm}$ of the magnet surface due to non-contact friction. In order to increase the measurement bandwidth, we actively damp the cantilever with a feedback loop whose phase is adjusted to $-\pi/2$. The damped quality factor is on the order of 400, but can vary from $200-500$ as a consequence of the position-dependent coupling to the surface (which slightly detunes the feedback loop). Importantly, the active damping equally affects the cantilever vibrations in response to small forces (which is our signal) and the thermal vibration background (which is unwanted noise). Therefore, it does not change the SNR as long as thermal vibrations are the dominant source of noise. Figure 2.6 shows an overall schematic of our MRFM system.

2.7 Cantilevers

Cantilevers were specifically designed to detect the extremely small forces produced by nuclear spins flipping within a magnetic field gradient [35]. To illustrate the sensitivity required, a single nuclear spin flipped in a magnetic field gradient of $5 \cdot 10^6\,\mathrm{T/m}$ produces a $7.6 \cdot 10^{-20}\,\mathrm{N}$ force.

In order to detect such small forces, MRFM cantilevers were designed to have low spring constants and fundamental frequencies [35]. These cantilevers were fabricated with shaft lengths of $90\,\mu\mathrm{m}$, $105\,\mu\mathrm{m}$, and $120\,\mu\mathrm{m}$, and spring constants ranging from $50-250\,\mu\mathrm{N/m}$. With such low spring constants, these cantilevers can routinely detect forces of approximately $10\,\mathrm{aN}$, corresponding to about $5,000$ nuclear spins. The most commonly used cantilever in this work was $120\,\mu\mathrm{m}$ long since it has the lowest spring constant, and the resonance frequency is high enough to evade low frequency noise sources, such as the turbo-pump running at $1500\,\mathrm{Hz}$.
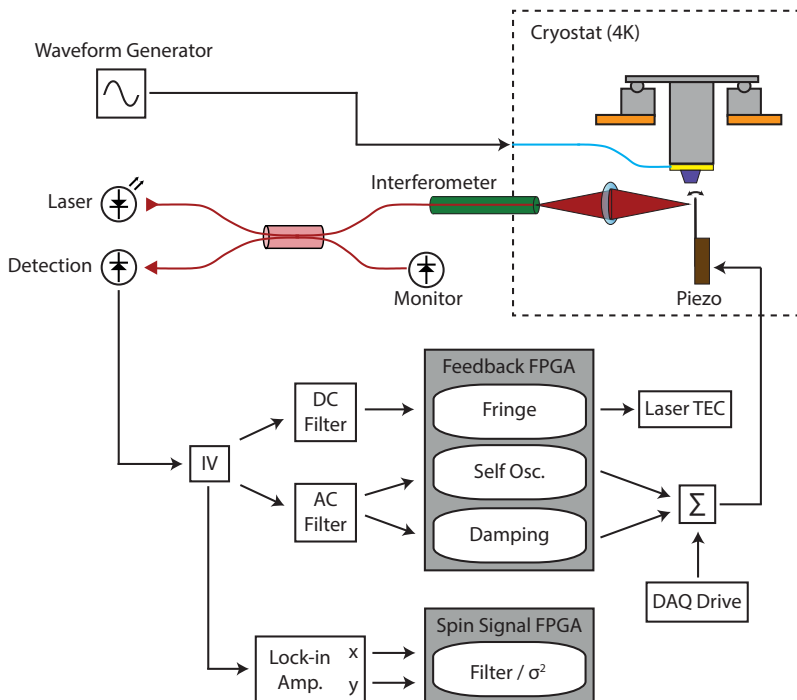
FIGURE 2.6: An overall schematic of the MRFM components built in this work. RF waveforms are applied to a strip line, which drive the cantilever proportional to the number of spins inverted. The interferometer measures the position of the cantilever. The signal is detected by a photodiode, which is amplified by an IV converter. The signal is split three ways, to a lock-in amplifier, and two filters for AC and DC. These signals are input into FPGA routines for feedback and spin signal detection.
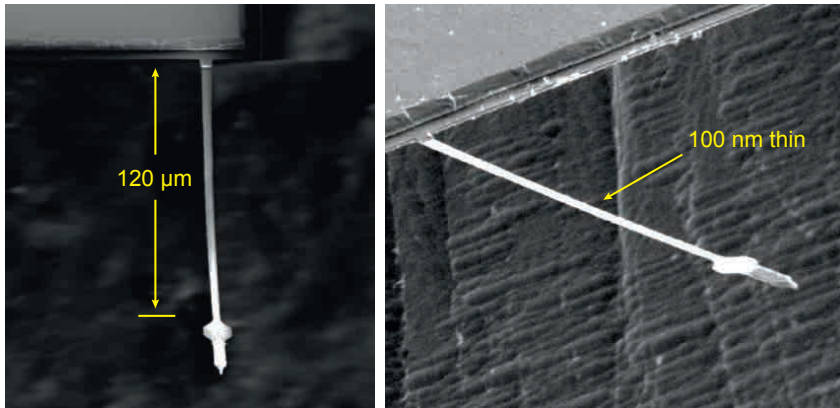
FIGURE 2.7: Scanning electron microscopy images of cantilevers fabricated in house. The cantilever shaft length is $120\,\mu$m and $135\,$nm thin. The entire cantilever length is $150\,\mu$m including the paddle ($10\,\mu$m) and mass.

Figure 2.7 shows SEM images of a cantilever with a $120\,\mu$m long and $4\,\mu$m wide shaft. A $10 \times 10\ \mu$m^2 paddle is located near the end of the cantilever for reflecting the laser interferometer. The increased surface area increases the reflection, and the device thickness of $135\,$nm maximizes reflectivity for a $1550\,$nm laser. Some cantilevers were fabricated with an additional mass on the end to damp higher harmonics.

2.8 Optical interferometer

The cantilever position is read out using a laser interferometer that is formed between the end of an optical fiber and the cantilever. Figure 2.8 shows a schematic of the interferometry setup. A $1550\,$nm wavelength diode laser with an intensity of approximately $100\,\mu$W was used. An FC optical fiber connector was partially connected to the laser source to couple
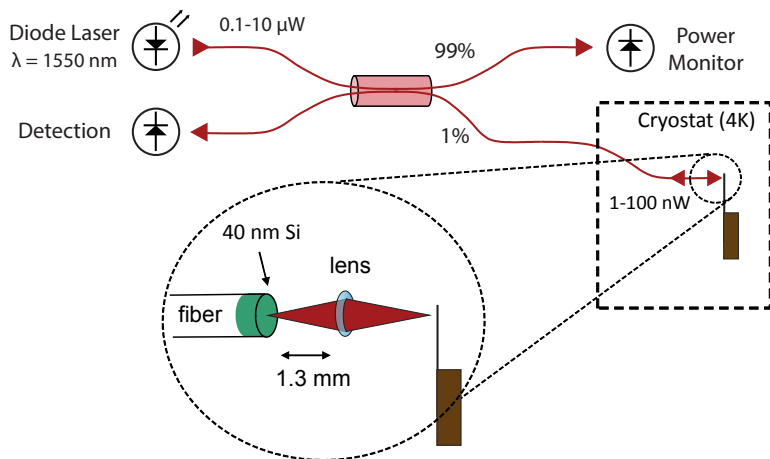
FIGURE 2.8: Schematic representation of the interferometer pathway.

$< 10\,\mu$W into the optical pathway. A directional splitter sent 99% of the intensity to a monitor photodiode, and the remaining 1% was passed down a branch to the cantilever. The laser quickly diverged when it exited the fiber, and therefore a lens was used to focus the beam back down onto the cantilever paddle.

Figure 2.9 shows a schematic representation of the interferometer formed between the fiber and cantilever. The end of the fiber was coated with approximately 60 nm of evaporated silicon that acts like a half silvered mirror. For a laser intensity of I_0 sent down the fiber, a fraction I_1 was reflected back from the silicon. The remaining fraction I_2 was transmitted, focused down by a lens, and reflected off the cantilever paddle. The intensity of the laser that reached the cantilever was approximately 100 nW. Higher laser powers than this cause increased Brownian motion [36]. Intensity I_3 accounts for intensity lost in the lens, and misalignment preventing 100% reflection. I_3 is focused back into the fiber, with part of it reflecting off
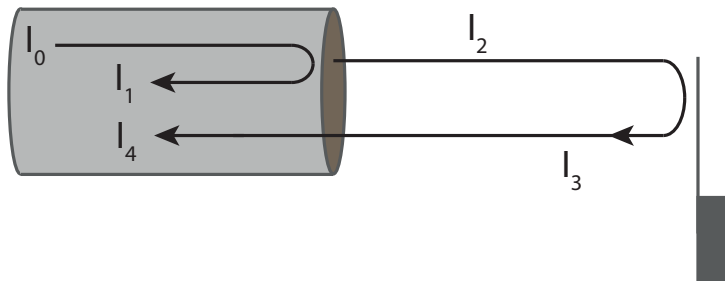
FIGURE 2.9: Schematic of the laser power intensities between the optical fiber and cantilever.

the fiber mirror. The interferometry signal is formed by the difference of I_1 and the intensity re-entering the fiber after reflecting off the cantilever I_4. Therefore maximum visibility is achieved when I_1 and I_4 are equal in magnitude.

At room temperature, the laser was finely adjusted using a 'fiber bender' to position the interferometer on the cantilever paddle. When the system is cooled, components thermally contract by different amounts, causing the fiber to de-align from the cantilever. This drift is reproducible, and therefore intentionally misaligning the optics at room temperature provides a means of having aligned optics at base temperature. Later the fiber bender was replaced by a set of Attocubes that can move the fiber in the YZ plane. However, this requires very low vibrations otherwise the vibrations to avoid oscillations of the fiber.

An interferometer performs best with high laser powers to avoid shot noise. However, high laser powers (typically above $\sim$100 nW for MRFM) cause the cantilever thermal motion to increase, resulting in reduced force sensitivity. This is caused by electron-hole pair generation, which then relaxes

to phonon excitations. The optimum laser power is operated as high as possible, but low enough that the thermal motion is not influenced.

2.8.1 Interferometer fringes

The intensity of the laser detected by the signal photodiode is described to first order by

$$I = I_o \left(1 - \nu \cdot cos(\frac{4\pi d}{\lambda}) \right)$$

where I_o is the incident laser intensity, d is the distance between the fiber and cantilever, and λ is the laser wavelength. The fringe visibility ν is a quantification of the interference signal calculated by

$$\nu = \frac{\text{fringe amplitude}}{\text{fringe DC}} = \frac{max - min}{max + min}$$

For a fixed displacement, the ideal visibility occurs when fully destructive interference is achieved, which is when the fringe minimum reaches 0 during an oscillation.

In the case of a fixed optical cavity length (i.e. stationary fiber and cantilever) fringes can be measured by sweeping the laser wavelength. A built-in thermoelectric cooler provides a means of adjusting the laser temperature, which in turn changes the laser wavelength. Figure 2.10 shows an example of fringes by sweeping the laser wavelength. Constructive interference, or a fringe maximum, occurs when I_4 is exactly in phase with I_1, whereas a fringe minimum corresponds to destructive interference, and is when the two beams are out of phase by π radians. Additionally, if the intensities of the two beam paths are out of phase by π radians, and are of equal intensities, then complete destructive interference occurs, corresponding to maximum visibility.
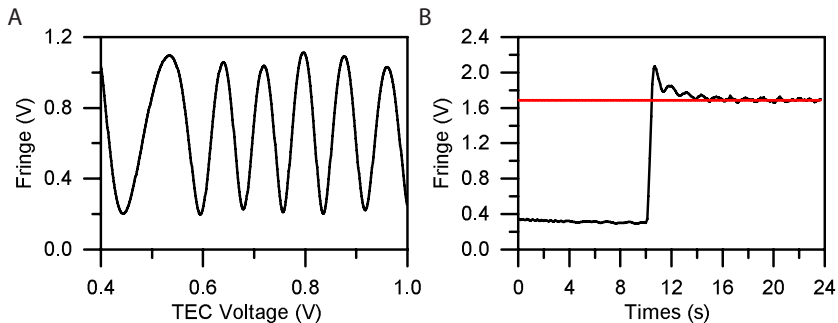
FIGURE 2.10: (a) Interferometer fringes after normalizing for the variation in laser intensity as a function of TEC voltage. (b) Fringe locking PID as a function of time. The red line corresponds to a setpoint, and the black curve is the DC value of the fringe. The PID is activated at $\sim 10\,$s, and the PID locks to the setpoint after $5\,$s.

The x-positional sensitivity of the interferometer is very high. Assuming that the cavity length is initially at the midpoint of a fringe, then a small displacement of the cantilever along the direction of the cavity perturbs the light intensity by

$$\frac{\partial I}{\partial d} = \frac{4\pi I_o \nu}{\lambda} \ .$$

The interferometer can also be used to calibrate the cantilever's oscillation amplitude. Since one fringe corresponds to a change of π radians, or half a wavelength, then displacing the cantilever by one fringe is half a wavelength.

2.8.2   Fringe locking

The laser diode wavelength is very sensitive to room temperature changes, which in turn modifies the optical cavity length. In order to stabilize the

interferometer wavelength against thermal drift of the room, a thermo-electric cooler (TEC) is used to adjust the diode temperature. The diode is maintained at a constant temperature with a feedback controller that applies a voltage to the TEC. An interferometer DC value is assigned as a setpoint, which is typically close to the fringe inflection point to achieve maximum positional sensitivity. The feedback output is proportional to deviation of the interferometer DC relative to the setpoint. In this work, we implemented a proportional-integral (PI) feedback controller with lab-view FPGA that runs independently of the computer, and consequently uses fewer resources. See appendix B.3 for more information about the implementation of the FPGA controller.

2.9 Stripline and magnet surface

A magnetic nano-pillar is used to produce a local magnetic field and a large gradient ($\approx 5 \cdot 10^6$ T/m). The pillar's field permeates through the sample, and produces a distribution of Larmor frequencies within a sample located on the cantilever. The second role of the pillar is to produce a very sharp magnetic field gradient. The larger this field gradient, the stronger the force that the cantilever feels when the spins are inverted. Underneath the pillar is a stripline that is used to generate AC currents. These currents produce an alternating B_1 magnetic field, which can be exploited to invert nuclear spins within the sample.

2.9.1 Design and fabrication

The initial generation of striplines used in this work were defined with optical lithography. Gold was evaporated through a PMMA mask, producing

electrical pads connected by a stripline of 2.7 μm in length, 0.8 μm wide, and 0.8 nm thick. The mask was removed, and a second PMMA layer was applied. A stepper motor was used to define holes in the PMMA directly over the striplines. A thin film ($\sim$270 nm) of magnetic material was evaporated over the entire surface. When the mask was removed using warm NMP (N-Methyl-2-pyrrolidone at 120° C), only magnetic pillars over the striplines remain. The surfaces were further cleaned with acetone, and isopropyl alcohol to remove any residues from the solvent. Figure 2.11 shows SEM images of a stripline chip at various length scales. Electrical leads for RF input were glued on with silver epoxy, or mechanically pressing them into indium. A second generation of striplines were designed with both mask steps using e-beam lithography. This method provides more control over the stripline geometry.

Many stripline materials were tested to decrease the surface roughness. This roughness must be minimized since it translates into a rougher magnetic pillar, which in turn decreases the magnetic field gradient. Gold, silver, platinum, and palladium were tested, but gold was found to have the lowest root-mean-squared (RMS) roughness. The RMS roughness of the stripline in figure 2.12 is approximately 1.7 nm. Thicker striplines also correspond to higher RMS roughness.

Conductive glue (Epotek H20e) was used to contact the stripline with thin copper wires. An electrically insulating glue (Epotek H70e) coated the electrical connections to increase mechanical strength. However, this approach was abandoned since each glue step required heating the substrate, and could potentially exacerbate oxide layers of the nanomagnet. Indium was found to provide great mechanical and electrical contacts. The pillar/stripline was imaged with a commercial AFM to determine the shape and roughness of the nanomagnet. SEM was avoided to prevent damage and carbon deposition from electron beams.
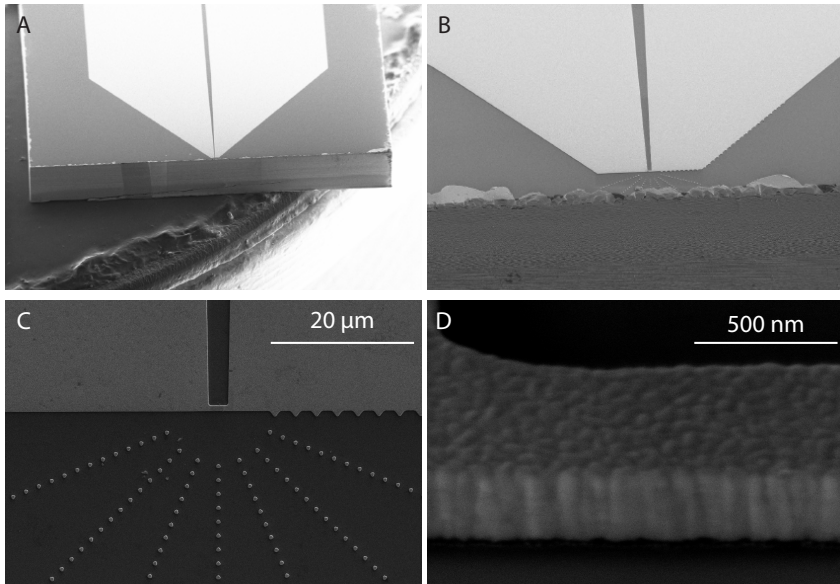
FIGURE 2.11: SEM image of a stripline chip showing the pads and edge of the sample. The stripline must be within about $50\mu m$ from the edge of the sample for the laser to not be cut off. Markers are placed between the sample edge and stripline to help guide the user to the stripline center. One side is also patterned with ridges to know where the user is located. The stripline height is 300 nm.

It was found that the second mask had a limited shelf life time. After a few years of storage in dry nitrogen, the mask became difficult to dissolve, likely due to cross-linking within the polymer. Removing the mask required sonicating for long times in NMP.

2.9.2   Magnetic pillar

Figure 2.12 shows an AFM image of two dysprosium pillars on a stripline. The two magnets were intentionally designed to have different shapes: one
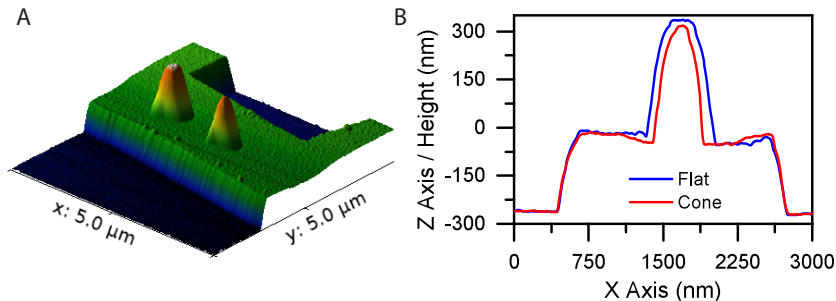
FIGURE 2.12: (a) Atomic force microscopy image of two dysprosium pillars. (b) Cross sections of the two magnets. The height of the stripline is $\approx 250\,\text{nm}$, the width is $\approx 2\,\mu\text{m}$. The two magnets are $365\,\text{nm}$ and $380\,\text{nm}$ tall above the stripline. The RMS roughness of the stripline is $1.7\,\text{nm}$ measured within a $2.3\,\mu\text{m}^2$ area. The roughness of the two magnets are under $5\,\text{nm}$.

with a flat top surface and the other with a sharp peak. The flat top magnet produces a large $\frac{dBz}{dx}$ magnetic field gradient, and is used for MRFM detection. The sharp tip can be used for high resolution topographic imaging (frequency-maps and touch-maps) of the cantilever surface.

The shape of the pillar is determined by the size of the hole over the stripline in the mask prior to evaporating magnetic material. The conical shape arises from the hole gradually closing during the evaporation of magnetic material [37]. If a hole is defined small enough, it completely closes up and forms a sharp peak. Conversely, a flat top pillar is created by defining a larger hole in the mask. The hole will gradually decrease in size, but the top surface is truncated when the evaporation is stopped.

Several magnetic materials were tested, including iron cobalt (FeCo), holmium (Ho), and dysprosium (Dy). Presently, Dy pillars have been demonstrated to produce the highest magnetic field gradients [38].
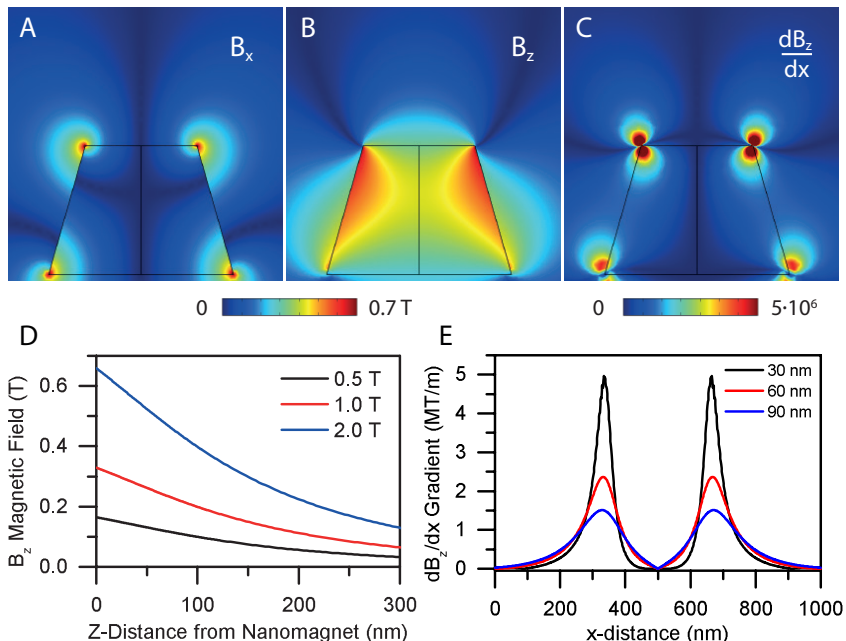
FIGURE 2.13: Simulation of the field components produced by a pillar magnetized to $1.5\,T$. The nanomagnet is $250\,nm$ wide at the top, and $300\,nm$ tall. The (a) B_x and (b) B_z field components in the x-z plane. (c) The dB_z/dx magnetic field gradient, indicating that the highest gradient is located over the edges of the pillar. (d) The B_z magnetic component directly over the magnet as a function of z-position and magnetization. (e) X-axis cross sections of the magnetic field gradient at various heights above the magnet: 30, 60, and $90\,nm$.

2.9.3 RF/B_1 magnetic field

The stripline geometry determines the shape of the B_1 magnetic field profile. Figure 2.14 shows the x-component of the B_1 field as a function of z-height above the center of a strip line.

Nuclear spins are inverted using waveforms composed of frequencies in the
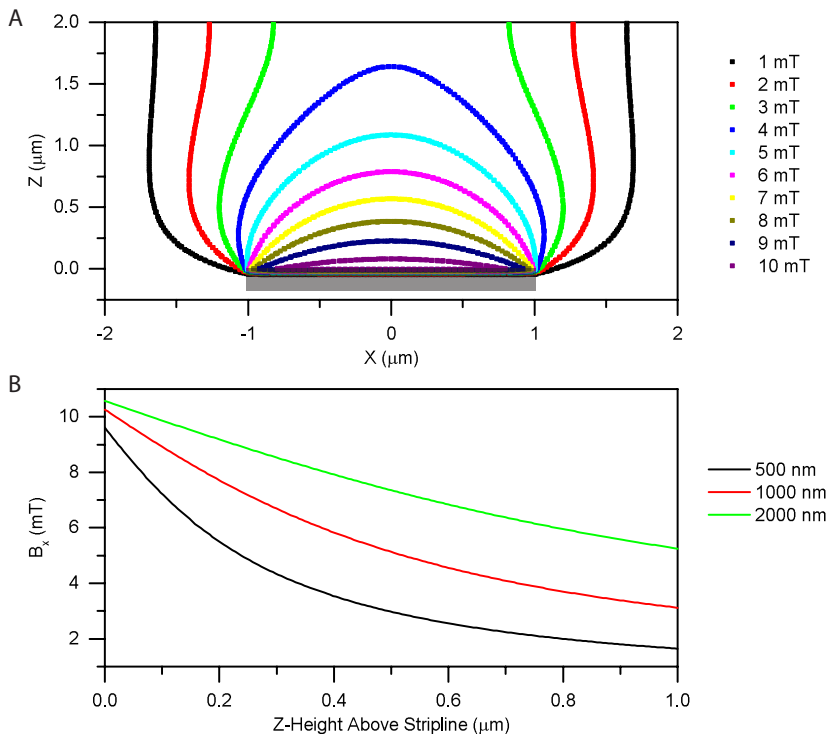
FIGURE 2.14: (a) The B_x component of the magnetic field contour lines produced by a 2000 nm wide stripline and 100 nm tall (indicated in grey). The stripline is infinitely long in the out of plane direction. The current density was set to $1.75 \cdot 10^{11} \, \mathrm{A/m^2}$, to produce roughly 8 mT magnetic field at 300 nm above the center of the stripline. This was found to be the peak B_1 field strength in this work. (b) The B_x component of the B_1 magnetic field as a function of z position. The profile was recorded directly over the center of the stripline (at $x = 0 \, \mu\mathrm{m}$ in a). Each line profile corresponds to a different stripline width. This simulation indicates that wider striplines produce more uniform B_1 fields.
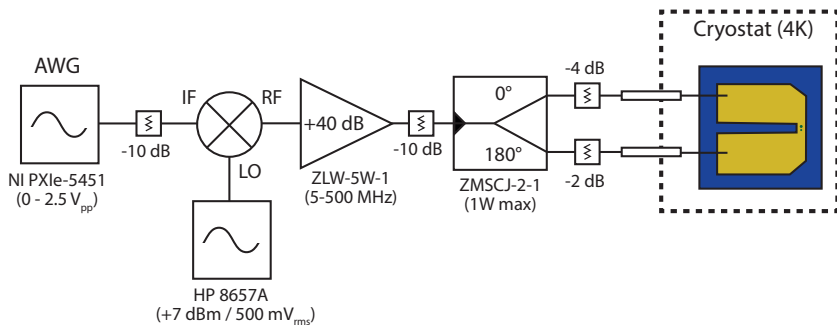
FIGURE 2.15: Circuit for producing RF waveforms that invert nuclear spins. A mixer is used to up-convert waveforms produced by the AWG.

range of $100 - 250$ MHz depending on the strength of the external magnetic field. Figure 2.15 illustrates the circuit used to produce these RF waveforms. The arbitrary waveform generator (AWG) produces frequencies from DC up to 150 MHz, which is sufficient for magnetic fields up to about 3.3 T. For higher fields, the AWG must be mixed up to reach up to 6 T. For example, in order to invert ^{1}H spins at 5 T corresponding to 212 MHz, a local oscillator of 300 MHz and AWG center frequency of 88 MHz to produce sidebands at 212 MHz and 388 MHz. The higher sideband is heavily attenuated by the stripline transmission.

The waveform is amplified, and then divided in two by a '0-180 degree' splitter [39]. The two sides of the splitter each carry a signal up to $10\,V_{p-p}$, which enter the cryostat and are applied to both sides of the stripline. If the voltages are exactly out of phase when they reach the stripline, then a voltage node forms in the middle of the stripline. This voltage node minimizes the electric field over the stripline, while the current can still oscillate.

Chapter 3

Nanomechanical Sensor

In MRFM, the detector consists of a micromechanical cantilever that is coupled to the nuclear magnetization by the sharp magnetic gradient G of a nanoscale ferromagnetic tip. This chapter describes the properties of the silicon cantilevers used in this work.

3.1 Mechanical properties

3.1.1 Bending motion

The slope s of a cantilever is given by

$$\frac{1}{s} = \frac{M_z(x)}{EI_z}$$

where s is the slope of the cantilever, E is the Young's modulus, I_z is the moment of inertia, and M_z is the bending moment. Figure 3.1 shows a
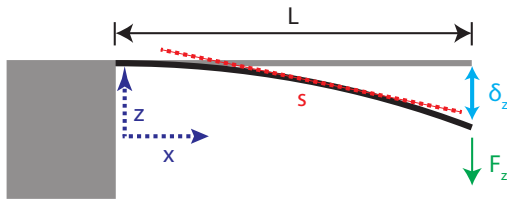
FIGURE 3.1: Cantilever model schematic.

schematic representation. The curvature κ of a general function $y = f(x)$

$$\kappa = \frac{|y''|}{(1 + y'^2)^{3/2}}$$

For small displacements, we can assume y'^2 is small, so that

$$\kappa \approx \left| \frac{d^2 y}{dx^2} \right|$$

For small cantilever deflections, $1/s = \kappa$ and therefore

$$\frac{d^2 y}{dx^2} = \frac{M(x)}{EI_z} \tag{3.1}$$

A force F_z induces a bending moment (M_z),

$$M_z(x) = (L - x)F_z \tag{3.2}$$

where L is the length of the beam. The axial moment of inertia:

$$I_z = \int_A z^2 dA = \int_{-d/2}^{d/2} \int_{-w/2}^{w/2} z^2 dx dz$$

$$I_z = \frac{wd^3}{12} \tag{3.3}$$

Combining equations (3.2), (3.3) and (3.3) provides a differential equation of displacement δ_z due to a force applied to the free end of a cantilever:

$$\frac{d^2}{dx^2}\delta_z(x) = 12\frac{L-x}{Ewd^3}F_z \tag{3.4}$$

The angular response of the cantilever as a function of x can be determined by integrating (3.4) along the lever to get

$$\theta_z(x) = 6\frac{(2L-x)x}{Ewd^3}F_z \tag{3.5}$$

This equation allows us to determine the angular spring constant: the ratio of the force acting on the end of the lever and the resulting slope

$$k_{\theta_z}(x) = \left|\frac{F_z}{\theta_z(x)}\right|$$

$$k_{\theta_z}(x) = \frac{Ewd^3}{6(2L-x)x}$$

so that at $x = L$,

$$k_{\theta_z}(L) = \frac{Ewd^3}{6L^2}$$

the displacement of the cantilever due to a force can be obtained by integrating equation (3.5)

$$\delta_z(x) = \frac{2x^2(3L-x)}{Ewd^3}F_z$$

3.1.2 Resonance frequency and amplitude

A cantilever's elastic response to an external force can be modeled with the Euler-Bernoulli differential equation [40]

$$EI\frac{d^4y(x,t)}{dx^4} + \rho A\frac{d^2y(x,t)}{dt^2} + C\frac{dy(x,t)}{dt} = F(x,t)$$

where y is the displacement at position x on the cantilever, E is Young's modulus, I is the bending moment ($I = \frac{wd^3}{12}$ for a beam), F is the applied force, ρ is the mass density, and C is a damping coefficient. This equation can be solved by separating the spatial and temporal parts of the displacement $y(x,t)$

$$y(x,t) = \sum_{j=1}^{\infty} \phi_j(x)q_j(t)$$

where $\phi_j(x)$ are the cantilever's normalized orthogonal modes [41]. This change of variable simplifies the equation to

$$\ddot{q}_j + \frac{C}{m}\dot{q}_j + \omega_j^2 q_j = \frac{1}{m}\int \phi_j(x)F(x,t)dx = p_j'(t) \tag{3.6}$$

An exact solution for the resonance frequencies of a beam can be obtained giving the harmonics of the cantilever [42]

$$\omega_i = \alpha_i\sqrt{\frac{EI}{\rho AL^4}}$$

where $\alpha_i = 1.875$, 4.694, and 7.885 correspond to the fundamental, first, and second harmonics respectively.

Equation (3.6) demonstrates that the mechanical resonance can be well approximated by a one dimensional driven simple harmonic oscillator [42]

$$m\ddot{x} + \Gamma\dot{x} + kx = F_d e^{i\omega_d t} \tag{3.7}$$

where $\Gamma = \frac{k}{\omega_0 Q}$ is the damping coefficient, ω_0 is the resonance frequency, F_d is a drive amplitude, and ω_d is the angular frequency of the drive force. Fourier transforming this differential equation provides

$$x(\omega) = \frac{F_d/m}{(\omega_0 - \omega_d)^2 + (\frac{\omega_0 \omega_d}{Q})^2} \ . \tag{3.8}$$

which describes a Lorentzian lineshape for cantilever motion as a function of frequency.

Although a simple beam provides a good approximation for the resonance properties of a cantilever, the paddle and mass extensions modify these results. Numerical simulations (such as Comsol) provide a means of determining the resonance frequency, c-factor, and spring constant of each eigenmode. Figure 3.2 shows simulations of the resonance modes of a cantilever with a fundamental mode of 6 kHz.

Figure 3.3 shows a plot of the interferometer power spectral density up to 500 MHz. The harmonics are assigned according to whether the peak could be mechanically driven.

3.1.3 Minimum detectable force

The dominant noise source for MRFM cantilevers is thermomechanical noise, which can be characterized using equation 3.8 and a flat force noise power spectral density S_F [43]

$$\langle x_{th}^2 \rangle = \int_0^\infty S_F(\omega) |\chi(\omega)|^2 d\omega \ .$$

where $\chi(\omega) = x(\omega)/F_d$ is the cantilever transfer function, and $\langle x_{th}^2 \rangle$ is the mean-square displacement of the cantilever due to thermal excitations.
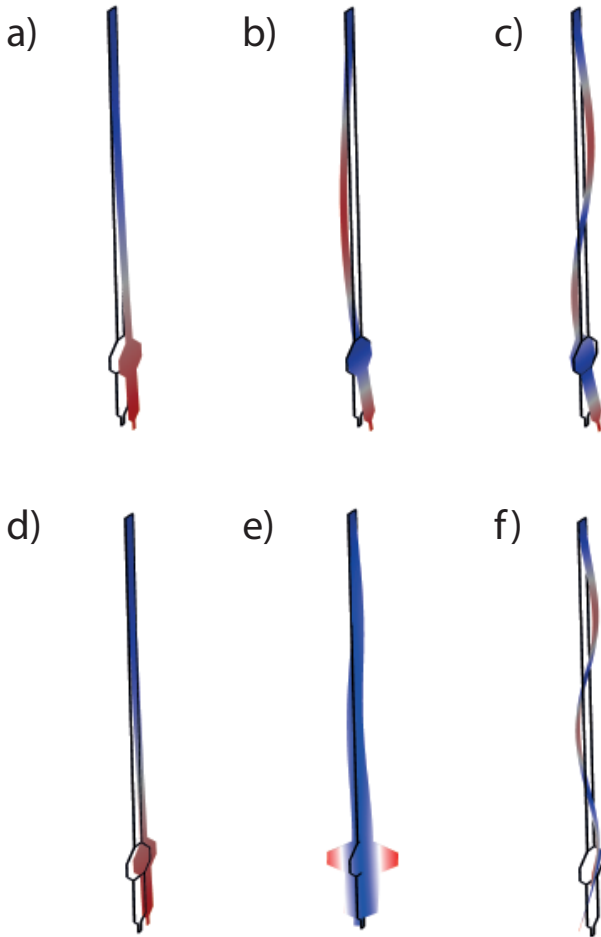
FIGURE 3.2: Cantilever modes simulated with Comsol (non mass loaded): a) fundamental mode (6.054 kHz), b) first harmonic (45.014 kHz), c) second harmonic (130.03 kHz), d) first y-axis mode (197.88 kHz), e) first torsional mode (253.78 kHz), d) third harmonic (256.36 kHz).
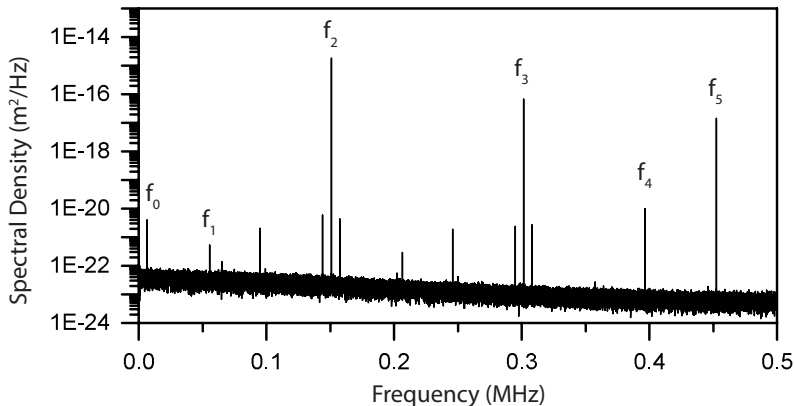
FIGURE 3.3: A spectral density plot showing several cantilever modes. The f_2 frequency was strongly driven during acquisition for better visibility of the modes. All other peaks are sum and difference frequencies due to mixing.

This integral simplifies when $Q \gg 1$, and the spectral density can be solved in terms of the cantilever thermal fluctuations

$$S_F^{1/2} = \left(\frac{4}{Q\omega_0}\right)^{1/2} k \langle x_{th}^2 \rangle \ .$$

When the cantilever is in thermal equilibrium with its environment, then $\langle x_{th}^2 \rangle$ can be described by the fluctuation-dissipation theorem [44]

$$\frac{1}{2} k \langle x_{th}^2 \rangle = \frac{1}{2} k_B T$$

where k_B is the Boltzmann constant and T is the temperature. Consequently, the spectral density simplifies to

$$S_F^{1/2} = \left(\frac{4 k k_B T}{Q\omega_0}\right)^{1/2}$$

$$S_F = 4\Gamma k_B T \ .$$

The minimum force detectable by a mechanical resonator is dependent on the bandwidth ΔB over which a force is acting on the oscillator

$$F_{min} = \sqrt{S_F \Delta B} = \sqrt{\frac{4k k_B T \Delta B}{\omega_0 Q}} \ . \tag{3.9}$$

Equation 3.9 states that the force resolution can be improved by operating at low temperatures, with a cantilever having a low spring constant and high resonance frequency [45].

Since the fluctuation-dissipation theorem provides a direct relationship between oscillation amplitude and temperature, we can use it to measure the cantilever temperature. This can be performed by recording the power spectral density of the cantilever motion (such as figure 3.3), and converting it from V^2/Hz to m^2/Hz using the fringe calibration. The temperature of a cantilever mode is calculated with

$$T = \frac{\left(k \langle x_{th}^2 \rangle c\right)^2}{k_B}$$

where c is the c-factor of the cantilever. The c-factor is the length of the cantilever, divided by the length between the base and the position of the laser on the cantilever.

3.1.4 Quality factor

The quality factor is a dimensionless quantity indicating how long energy can be stored in a mechanical oscillator before it dissipates. The quality

factor is calculated

$$Q = \frac{\omega_o}{\Delta\omega}$$

where ω_o is the resonance frequency, and $\Delta\omega$ is the spectrum linewidth. This equation corresponds to the amount of energy in the system, divided by the amount of energy lost per oscillation cycle. An oscillator with no dissipation has an infinitely thin spectrum (or corresponds to a delta function), and therefore has an infinite quality factor.

The quality factor of a cantilever can be measured in two ways: the spectrum linewidth or a ring-down curve. Experience has found that ring-down curves more accurately measure high quality factors, whereas measuring linewidths are preferential for low quality factors. This is because the spectral linewidth can include effects like dephasing, nonlinearity, and frequency noise.

A ring-down curve is measured by driving a cantilever at its resonance frequency by applying an AC voltage to two piezoelectric disks stacked together. The drive signal is abruptly turned off, and the cantilever motion is measured until the amplitude decays to zero. An exponential function is fit to the envelope of the amplitude. Within a $1/e$ decay time τ_0, the quality factor is given by $Q = \pi\tau_0 f_0$ [34]. Multiple ring-down curves are measured and averaged together to improve the signal-to-noise ratio, and therefore improve the fit accuracy. Typical Q-factor precision is within a few percent. Care must be taken to not drive the cantilever into the non-linear regime, otherwise this calculation does not hold true.

3.2 Dissipation mechanisms

Energy in a cantilever can be dissipated through several damping mechanisms including impurities, viscous air damping, clamping loss, and thermoelastic dissipation. Each of these dissipation channels acts in parallel to give the measured quality factor Q

$$\frac{1}{Q} = \sum_i \frac{1}{Q_i} = \frac{1}{Q_{intrinsic}} + \frac{1}{Q_{viscous}} + \frac{1}{Q_{clamping}} + \frac{1}{Q_{ted}} + ... \quad (3.10)$$

where $Q_{intrinsic}$ is intrinsic damping dependent on the material and geometry, $Q_{viscous}$ results in energy lost to a surrounding medium, $Q_{clamping}$ is clamping loss due to energy transferred to the supporting structure, and Q_{ted} is thermolectric dissipation caused by irreversible conversion of mechanical motion to heat. The consequence of equation (3.10) is that the largest dissipation channel determines the overall measured quality factor [34], and therefore they must all be minimized to increase the measured quality factor.

3.2.1 Material defects

Impurities within the cantilever volume have been identified as a primary source of energy dissipation. Eliminating these volume defects by using materials with low impurity densities leads to higher quality factors. The computer industry has highly refined silicon processing to extreme qualities. In this work, we use in-house fabricated cantilevers from single crystal silicon to achieve high mechanical quality factors. At room temperature, the quality factor of silicon MRFM cantilevers typically range from $5,000$ to $20,000$. When cooled to $4\,\mathrm{K}$, quality factors typically rise proportional to their room temperature values in the range of $20,000$ to $70,000$.

As mechanical oscillators are decreased in size, their surface to volume ratio rapidly increases. In general, quality factors decrease with smaller device volumes indicating the importance of surface dissipation mechanisms [34, 42]. Therefore, further improvement is achieved by eliminating surface defects, such as native oxide layers and organic material from the fabrication process. Organic contaminants can be easily removed using high energy (i.e. $400 - 600$ Watts) oxygen plasma for a few minutes. Oxide layers can be removed using HF vapor treatment, but regrowth occurs under ambient conditions within a matter of hours. We have developed a technique to avoid oxide layers by using high quality (electronic grade) diamond instead of silicon [31]. However, since diamond is much more expensive and difficult to process, it is currently not feasible to replace silicon cantilevers.

Magnetic impurities are another form of surface contamination that can be introduced during fabrication processes. Experience has shown that evaporators and critical point driers are the primary sources of magnetic impurities. The quality factors of affected cantilevers drop proportional to the square of the external magnetic field strength. This is also the reason why recent MRFM experiments have moved away from attaching a magnet to the cantilever [39]. Figure 3.4 shows an example of a cantilever with magnetic contamination. For fields above approximately $1\,\mathrm{T}$, the quality factor was reduced by a factor of 2 or 3.

3.2.2 Viscous damping

Viscous damping results from a cantilever interacting with its surrounding medium. At atmospheric pressure, air acts like a continuous medium, causing the cantilever to drag air with its oscillations. As the pressure

A

B
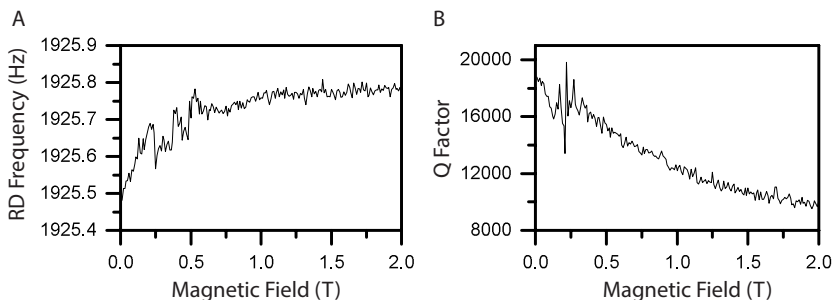
FIGURE 3.4: The response a magnetically contaminated cantilever. (a) The ringdown frequency (RD) changes as a function of magnetic field strength. As the field is ramped up, the spring constant becomes stiffer which is reflected in an increasing ringdown frequency. This effect levels off above 1 T as the magnetization saturates. A few jumps appear in the frequency below 0.75 T are due to magnetic domain reorganization [46, 47]. (b) Unlike the spring constant, the quality factor continues to decrease with higher fields.

is decreased, the interaction is well modeled by the cantilever transferring momentum to individual air molecules, since the air molecules do not strongly interact. Within this low pressure regime, the amount of damping is dependent on the mean free path of the air molecules compared to the resonator's size [48]. Higher surface roughness also decreases cantilever quality factors in this low pressure regime, but the effect is reduced with lower pressure [49]. Viscous damping can be readily overcome by reducing the chamber pressure to low vacuum pressures. Generally the cantilever quality factor is unchanged by further pumping below pressures of 10^{-5} mbar.

3.2.3 Clamping loss

Clamping loss is dissipation due to insufficient anchoring at the resonator's hinge. Oscillations of the cantilever produces strain in the hinge, which in turn can excite modes in the support material. This effect can be separated into in-plane and out-of-plane dissipation channels. For a 2D surface

$$Q_{clamping} = \alpha \frac{L^3}{w^3}$$

where w is the resonator width, L is the length, and α is a material-dependent parameter [42]. Calculations indicate that $\alpha = 2.17$ for a singly clamped silicon beam [50]. With MRFM cantilevers of $150 \, \mu$m in length, and $4 \, \mu$m, $Q_{in-plane} \approx 114,000$. Therefore, since measured quality factors are generally at least a factor of two lower than this, we can ignore clamping loss. Furthermore, higher order modes are less susceptible than the fundamental mode as energy is stored in nodes further from the clamping [42, 51].

3.2.4 Thermoelastic

Thermoelastic dissipation is the result of irreversible heat flow induced by mechanical strain. An oscillating cantilever mode can induce regions of compression and expansion. This volume compression produces local heating, and expansion induces local cooling. The system attempts to reach equilibrium by thermal flow, causing irreversible energy loss [48].

Previous work has demonstrated that $10 \, \mu$m thick cantilevers can be dominated by thermoelastic dissipation [52]. However, submicron-thick MRFM cantilevers are virtually unaffected by this dissipation channel [34].

3.3 Surface interaction forces

When a cantilever is approached to a surface, it experiences additional conservative and dissipative forces. These interactions add additional force terms ($F_{ts}(t)$) to the simple harmonic oscillation equation (3.7)

$$m\ddot{x} + \Gamma\dot{x} + kx = F_{signal}(t) + F_{noise}(t) + F_{ts}(t) \qquad (3.11)$$

In MRFM, the cantilever and magnetic tip strongly interact when brought close together. These interactions influence the cantilever dynamics and cause a large shift in resonance frequency. Furthermore, dissipative interactions dramatically decrease quality factors, and limit how close the cantilever can be operated relative to the magnetic tip.

3.3.1 Electrostatic forces

Any two surfaces that are imbalanced in charge experience long-range electrostatic interactions. For example, an electrostatic potential difference U between a sphere and a planar surface with radius R leads to a force equal to

$$F_e(z) = \frac{-\pi\epsilon_0 R U^2}{z}$$

where z is the separation of the two surfaces.

Typically in MRFM, long-range forces manifest through trapped charges in the tip and/or sample. These interactions can be observed as a frequency shift of the cantilever even at micron tip-sample separations. Trapped charges can be neutralized with a radioactive source that emits alpha-particles. Aiming the radioactive source at the tip and sample for approximately 10 seconds neutralizes trapped charges. This treatment is performed at room temperature before closing the system.

Any polarizable material in an electric field gradient also experiences a force

$$F_\epsilon = \vec{p} \cdot \nabla \vec{E}$$

Since all dielectrics experience this force, it has been proposed as a universal method to oscillate nanomechanical systems [53]. In MRFM, RF pulses drive nuclear spin inversions at the cantilever frequency f_0 while modulating the RF amplitude at $2 \times f_0$. Consequently, a strong RF amplitude can lead to parametric driving that influences the cantilever motion at f_0.

3.3.2 van der Waals

The van der Waals force is a generalization of three forces: orientation (Keesom), induction (Debye) and dispersion (London). Each of these interactions is proportional to $1/r^6$. In the simplified case of a sphere of radius R interacting with a flat surface, the van der Waals potential is

$$V_{VDW} = \frac{-A_H R}{6z}$$

where A_H is the Hamaker constant that depends on the atomic polarizability and density of the tip and sample. As an example, a $100\,\mathrm{nm}$ sphere, separated from a surface by $z = 0.5\,\mathrm{nm}$, experiences a force of $\sim 10\,\mathrm{nN}$ [54]. Therefore, since MRFM is generally operated with tip-sample separations greater than $10\,\mathrm{nm}$, this interaction is negligible.

3.3.3 Non-contact friction

When two objects are close enough to chemically interact, they influence each other with contact friction. However, when they are further away

but still dissipating energy from one another, this is referred to as non-contact friction. Although this remains an on-going research subject, three primary sources of non-contact friction have been identified: phononic friction, joule dissipation, and van der Waals friction [54].

Phononic friction occurs due to a deformation in the tip or surface, which in turn relaxes and emits a phonon [54]. Since MRFM cantilevers have such low spring constants, they are more likely to be deflected (and produce frequency noise) than to to dissipate energy through this friction channel.

Joule dissipation is a consequence of electrostatic forces between a tip and sample. Fluctuating charges within the stripline can impart an image charge on the cantilever, or vice versa. Energy is dissipated if the image charge experiences a resistive loss with the tip-sample motion [54, 55]. It has been shown that this electronic friction can be eliminated using a superconducting substrate (see section C.1 for supplementary details) [56], however it is difficult to implement this with MRFM since high magnetic fields generally destroy superconductivity.

In MRFM, van der Waals fluctuations have been identified as the primary source of non-contact friction [57, 58]. This interaction results from both thermal and zero-point quantum fluctuations in a dielectric that form short-lived dipoles [59]. These fluctuations can induce a dipole through space to a nearby object. If this induced dipole relaxes the energy to a phonon, then the energy is dissipated. These interactions can be reduced by evaporating a metal layer (typically gold) on the cantilever to screen dielectric materials from fluctuating dipoles [57].

3.3.4 Dependence on tip-sample geometry

In this work, we attached InAs and GaAs nanowires to cantilevers to decrease the interaction between tip and surface [17, 60]. Figure 3.5 shows some representative images of an InAs nanowire attached to a cantilever. The surface interaction between the nanowire and surface was dramatically reduced using such a high aspect ratio probe.

The non-contact friction coefficient Γ influencing a cantilever can be measured with a ringdown curve

$$\Gamma = \frac{2k}{\omega_c^2 \tau}$$

where k is the spring constant, ω_c is the cantilever frequency, and τ is the ringdown time [58, 61]. Figure 3.6 shows an approach curve of an InAs nanowire to a gold substrate. The quality factor is measured at sequential heights above the surface, and is virtually unaffected by non-contact friction until ~ 30 nm from the surface.

3.4 Feedback control

A feedback loop is used to coherently control the cantilever vibrational amplitude. The feedback can be operated in two ways: i) self oscillation mode (or positive feedback), which sustains a constant oscillation amplitude, and ii) damping (or negative feedback) which reduces the cantilever motion. Self oscillation is a necessary pre-requisite for imaging surface topography, whereas negative feedback is essential for spin signal detection. Conveniently, both of these methods are implemented with the same feedback circuit.
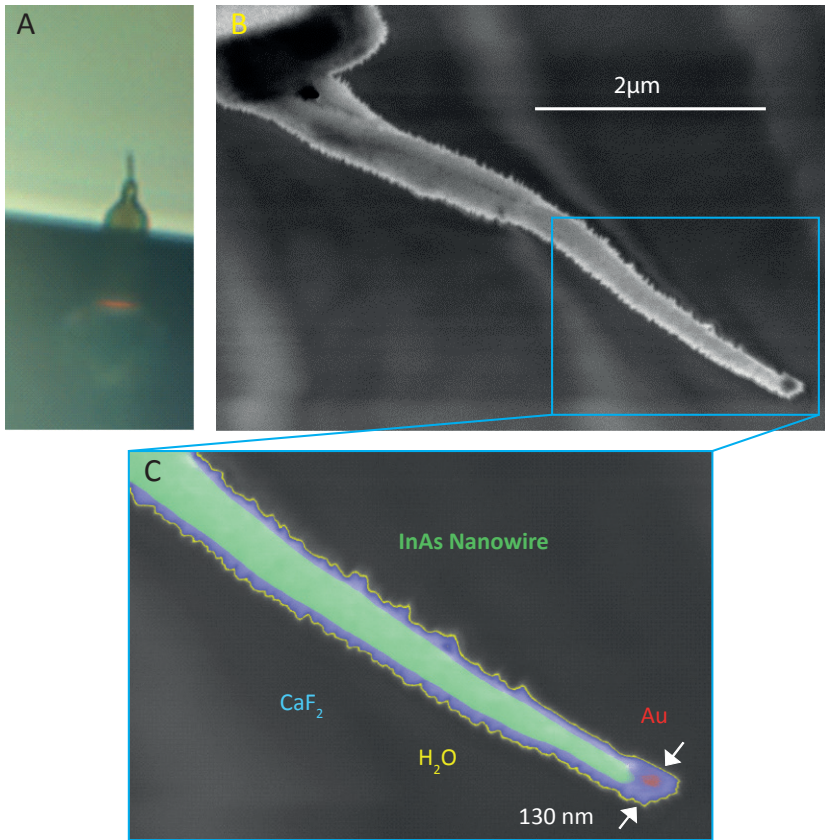
FIGURE 3.5: (a) Optical image of a nanowire attached to the end of a cantilever. The cantilever is fixed against a blade, just above the paddle. (b) Large scale SEM image of an InAs nanowire attached to a cantilever. (c) SEM image with false colours indicating the material layers. The InAs nanowire is 120 nm in diameter and has a gold catalyst fixed at the end. A 60 nm layer of CaF_2 was thermally evaporated onto the nanowire before it was attached to the cantilever. The nanowire was placed in the cryostat and cooled to 4 K, which always produces a $\sim$1 nm ice layer on the outer surface.
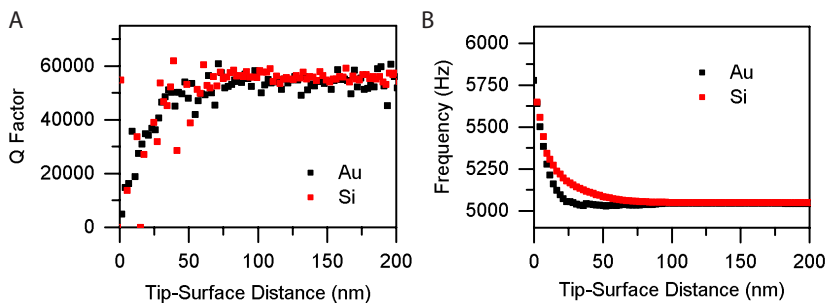
FIGURE 3.6: Approach curves showing the mechanical dissipation as a function of tip-sample separation. (a) The quality factor is virtually unaffected until approximately 30 nm above both silicon and gold surfaces. Below 30 nm, the quality factor quickly drops off for both materials. (b) The frequency response of both approach curves. The silicon surface more strongly interacts with the cantilever, and causes a larger shift than gold.

3.4.1   Feedback circuit

Self oscillation and damping feedback modes both use the cantilever detection as an input for excitation. Figure 3.7 shows a schematic representation of this feedback circuit. The cantilever's motion is measured by an interferometer and detected with a photodiode. The photocurrent is amplified by 10^6 to 10^7 and converted to a $\pm 10\,\text{V}$ signal by a Femto IV converter. An SRS 560 bandpass filters around the cantilever resonance, and amplifies the AC signal by $100 - 500$. An additional low-pass filter heavily attenuates above 20 kHz to prevent higher cantilever harmonics from being influenced. The signal is passed into a Laview FPGA which performs a phase shift, and then is multiplied by a gain factor g. A high-pass filter eliminates any DC offset produced by the FPGA. The output signal is applied to a piezo actuator to excite to the cantilever and complete the feedback loop.
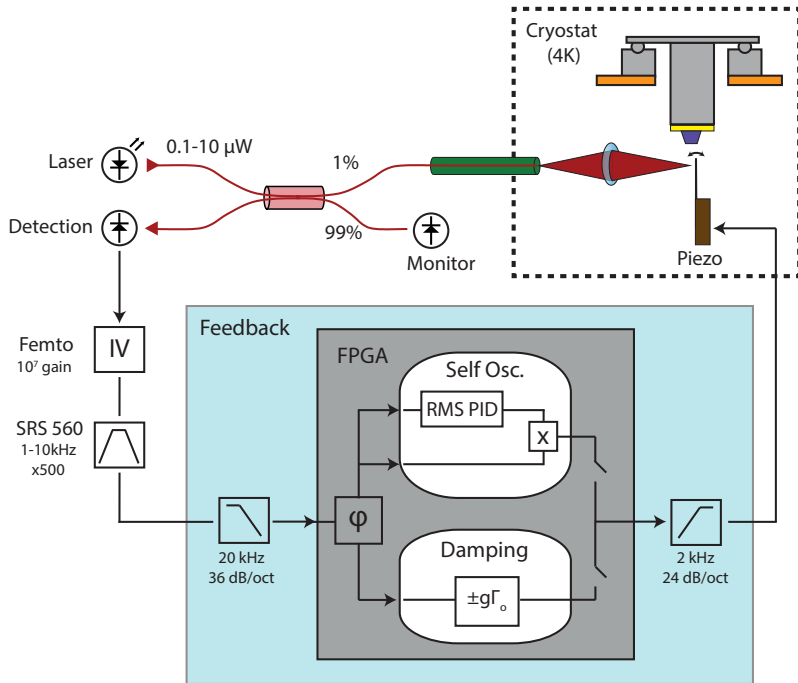
FIGURE 3.7: Schematic representation of the cantilever motion feedback loop. The cantilever's motion is detected by an interferometer, phase shifted, and a gain is applied before using the signal to drive a piezo actuator.

3.4.2 Self oscillation

As a cantilever is moved around a surface, the tip experiences conservative and dissipative interactions that shift the resonance frequency. For soft MRFM cantilevers, these interactions shift the resonance frequency up to several hundred Hz. Additionally, the cantilever must be strongly driven to overcome highly dissipative interactions. Therefore, to overcome the large

frequency shifts and dynamic amplitude required, a constant frequency and amplitude drive (as used with standard AFM) is unusable.

The cantilever motion and excitation are $90°$ out of phase. Therefore, when the phase shifter is set to $90°$, the feedback loop operates in self oscillation mode, and optimally drives the cantilever. If the output voltage driving the piezo is not limited, the cantilever will be continuously driven up. This runaway process can be avoided with a PID feedback that controls the gain factor to maintain a constant amplitude.

3.4.3 Damping feedback

A cantilever with a high mechanical quality factor is well isolated from its environment. An excitation signal must be precisely tuned to the cantilever's resonance frequency to actuate it. Therefore, when using a cantilever with a high quality factor to detect an excitation signal, the cantilever acts like a narrow bandpass filter proportional to its Lorentzian line shape. Additionally, high quality factors have inherently slow response times to drive tones, which translates to requiring long acquisition times for spin signal detection.

This slow response time and narrow excitation bandwidth issue can be mitigated by damping the cantilever to decrease the quality factor. A convenient damping method is using the self oscillation feedback loop. When the feedback phase is matched to the excitation phase, approximately $90°$, then cantilever is optimally driven up. If this excitation is inverted, or equivalently if an additional phase of $180°$ is applied, then the feedback loop damps the motion.

Figure 3.8 shows the cantilever's response to the damping circuit. At room temperature $(300\,\mathrm{K})$, the mechanical quality factor is approximately
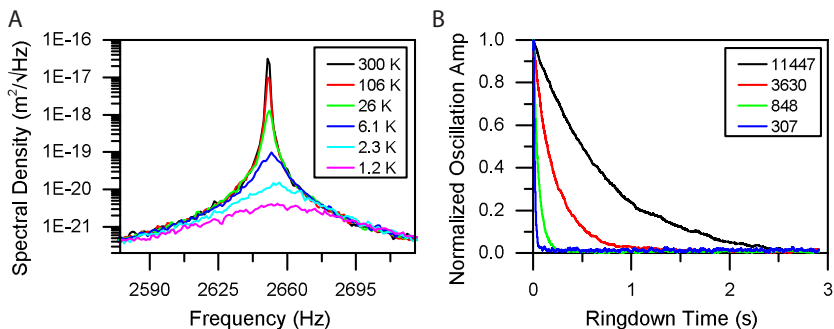
FIGURE 3.8: (a) Cantilever spectra for various damping gains. 300K corresponds to no damping gain, and the oscillation amplitude is increasingly damped as a function of damping gain. The effective mode temperature is given by the plot legend. (b) Ringdown curves for the first four damping gains plotted in the spectra. The curves are fit, and extracted quality factors are given in the legend.

12,000, and consequently has a very narrow peak. By damping the cantilever harder, the response time of the cantilever decreases, and the spectra become flatter. The effective temperature of the cantilever, measured by its mechanical fluctuations according to the fluctuation-dissipation theorem, can be decreased by over two orders of magnitude down to $1.2\,\mathrm{K}$. At a base temperature of $4.2\,\mathrm{K}$, the cantilever can be damped to mK temperatures [39].

This feedback equally damps the mechanical response to both noise and drive signals. Consequently, no loss in signal to noise is measured unless the cantilever is damped below the optical detector noise floor. Figure 3.9a shows the undamped cantilever response with and without a drive tone, whereas figure 3.9b shows the damped case. The magnitude of the drive tone is the same for both the damped and undamped cases.
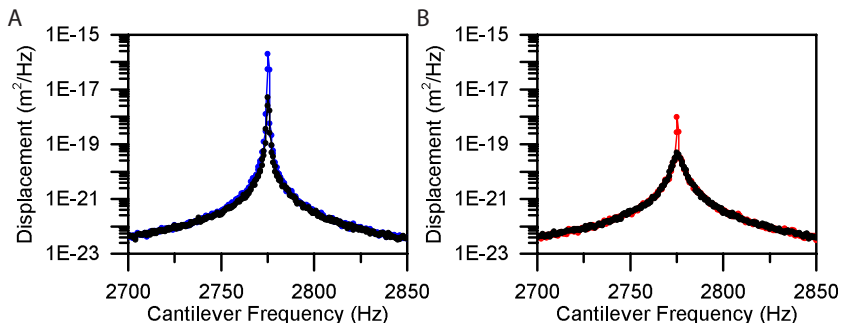
FIGURE 3.9: (a) Spectrum of an undamped cantilever with a quality factor of $\sim 15,000$. The spectrum is shown with (blue) and without (black) a drive tone of $100\,\text{mV}$ set to the resonance frequency of the cantilever. (b) The same spectra were recorded with the cantilever damped to a quality factor of 300. The signal (drive tone) and thermal noise are equally damped.

3.4.4 Phase shifter

The optical detection and piezoelectric drive are in principle $90°$ out of phase. In order to optimally excite the cantilever with the detection signal, a phase shift must be applied to compensate for this phase difference. To this end, we have implemented an all-pass filter to arbitrarily shift the phase of an input signal without attenuating its amplitude.

An analog transfer function $H(s)$ linearly maps a continuous input $X(t)$ to an output $Y(t)$

$$Y(t) = H(s)X(t)$$

where s is a continuous variable in Laplace space. In the case of an all-pass filter, this transfer function is

$$H(s) = \frac{s\tau - 1}{s\tau + 1}$$

where $\tau = RC$ is a time constant set by resistance R and capacitance C. A digital transfer function maps a discretely sampled time series $X(z)$ to an output $Y(z)$ by a complex frequency domain function $H(z)$

$$Y(z) = H(z)X(z)$$

and the corresponding discrete all-pass filter is

$$H(z) = \frac{z^{-1} - \bar{z}_0}{1 - z_0 z^{-1}} \tag{3.12}$$

where $\bar{z}_0$ is a complex pole. In order to implement this function, equation 3.12 can be converted to have real coefficients through multiplying by its complex conjugate to give

$$H(z) = \frac{z^{-2} - 2\Re(z_0)z^{-1} + |z_0|^2}{1 - 2\Re(z_0)z^{-1} + |z_0|^2 z^{-2}} \; . \tag{3.13}$$

This all-pass filter function was implemented as a standalone Labview FPGA process. See appendix B.4.1 for more information on the details of this implementation.

The phase shift produced by the all-pass filter (equation (3.12)) is determined by the complex pole z_0 and the frequency of the input signal z

$$z = \exp(i\omega T_s) = \cos(T_s\omega) + i\sin(T_s\omega)$$

where T_s is the sampling time and $\omega = 2\pi f$ is the signal frequency, or in this case the cantilever angular frequency. We seek to adjust the complex pole to produce a desired phase shift θ. The complex phase angle is

$$\tan\theta = \frac{\Im\{H\}}{\Re\{H\}} = \frac{2\left(z_0^2 - 1\right)\sin(T_s\omega)\left(\left(z_0^2 + 1\right)\cos(T_s\omega) - 2z_0\right)}{(z_0^4 + 1)\cos(2T_s\omega) - 4\left(z_0^3 + z_0\right)\cos(T_s\omega) + 6z_0^2} \; .$$
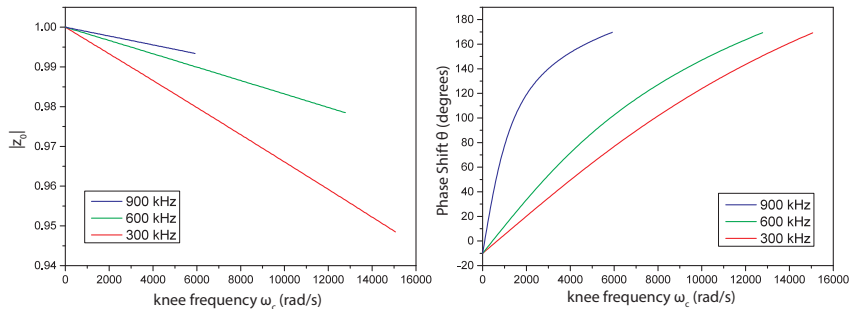
FIGURE 3.10: (a) The magnitude of the complex pole $|z_0|$ as a function of the knee frequency ω_c. (b) The corresponding phase shift produced by each $|z_0|$ value from (a). The FPGA loop rate changes the range that the pole must be shifted in order to cover the entire phase shift range.

Solving this equation to produce a phase shift $\theta = 180°$ (and $|z_0| <= 1$) with Mathematica yields two solutions

$$|z_0| = \sec(T_s\omega_c) \pm \tan(T_s\omega_c) \tag{3.14}$$

where ω_c is a characteristic knee frequency. Assigning a constant pole phase $\psi = 0°$ simplifies the all-pass filter to a one parameter system, and shifts the phase according to ω_c. Figure 3.10 shows sample plots of $|z_0|$ and phase shift θ as a function of the knee frequency ω_c. For more details about this implementation, see appendix B.4.2.

3.4.5   Feedback function derivation

The feedback function of this circuit can be derived starting from the equation of a harmonic oscillator driven by a thermal force and a feedback force

$$m\ddot{x} + \Gamma_0\dot{x} + kx = F_{th} - F_{fb} \ .$$

The displacement of the cantilever can be written in the form

$$x(\omega) = \hat{\mathbf{x}}(\omega)e^{i\omega t} \ .$$

In this feedback circuit, the feedback force is the cantilever's motion with a phase (or delay)

$$F_{fb} = ge^{i(\omega t - \pi/2 - \phi)}$$

where $\phi = 0$ corresponds to ideal feedback damping, and g is the feedback gain by scaling the amplitude. The feedback force can be rewritten in terms of $x(\omega)$

$$F_{fb} = g\cos(\phi)\Gamma_0(\dot{x} + \dot{x}_n) - g\sin(\phi)\omega\Gamma_0(x + x_n)$$

where the $cos(\phi)$ term corresponds to a spring softening, and the $sin(\phi)$ term corresponds to spring hardening. x_n is the measurement noise in the displacement signal.

Combining these equations we obtain

$$m\ddot{x} + \Gamma_0\dot{x} + kx = F_{th} - g\cos(\phi)\Gamma_0(\dot{x} + \dot{x}_n) - g\sin(\phi)\omega\Gamma_0(x + x_n)$$

and rewriting this in the form

$$-m\omega^2 x + i\omega\Gamma_0\left(1 + g\cos(\phi)\right)x + k_0\left(1 + g\sin(\phi)\frac{\omega}{\omega_0 Q_0}\right)x$$
$$= F_{th} - i\omega g\cos(\phi)\Gamma_0 x_n - \omega g\sin(\phi)\Gamma_0 x_n \quad (3.15)$$

provides a convenient form to obtain the complex transfer function

$$\hat{\mathbf{x}}(\omega) = \frac{\frac{1}{m}\hat{\mathbf{F}}_{th} - g\sin(\phi)\omega_0\omega Q_0\hat{\mathbf{x}}_n - ig\cos(\phi)\omega_0\omega Q_0\hat{\mathbf{x}}_n}{\omega_0^2(1 + g\sin(\phi)\frac{\omega}{\omega_0 Q_0}) - \omega^2 + i\omega_0\omega Q_0(1 + g\cos(\phi))}$$

3.5 Imaging surface topography

Commercial atomic force microscopes generally image surface topography by moving a cantilever tip over a surface and monitoring the change in amplitude. A PID feedback loop maintains a constant oscillation amplitude by moving the cantilever away from the surface if the amplitude decreases, and towards the surface when the amplitude increases. An image obtained corresponds to the z-heights over each position of the surface.

A less common approach to imaging surfaces is monitoring the frequency of the cantilever as a function of position [44]. A phase-locked loop (PLL) monitors the frequency shift of the cantilever as it scans over the surface. The tip-sample separation is changed to maintain a constant frequency, and the tip-sample separation gives an image of the surface. This method is particularly useful for cantilevers with high quality factors. However, this method also requires cantilevers with very high spring constants, and very small oscillation amplitudes.

In the case of MRFM, the cantilever has a very soft spring constant. For this reason, the resonance frequency can change by hundreds of hertz from position to position, which makes it very difficult to use a PID feedback loop to maintain a constant frequency or amplitude. One approach is to modulate the height based on the mechanical dissipation measured by the amplitude PID [62]. However, this approach incorrectly reports topography when imaging across two materials with high and low dissipation, such as SiO_2 and gold respectively. In order to circumvent these issues, we use two imaging modes referred to as 'frequency-maps' and 'touch-maps.'

3.5.1 Frequency maps

When a harmonic oscillator is influenced by tip-sample forces, the cantilever exhibits an elastic response. These forces influence the cantilever such that for small oscillations

$$F = F_0 + \frac{dF}{dz}(z - z_0) \ .$$

The force gradient modulates the spring constant of the cantilever, producing an effective spring

$$k_e = -\frac{dF}{dz} = k - \frac{dF_{ts}}{dz} \ .$$

Consequently, the resonance frequency of the cantilever is shifted by [59]

$$\omega_e = \Big(\frac{k - dF_{ts}/dz}{m}\Big)^{1/2}$$

$$\omega_e = \omega_o - \sqrt{\frac{1}{m}\frac{dF_{ts}}{dz}} \ .$$

Therefore, the tip-sample interaction forces can be monitored through the change in resonance frequency [44]. In scanning probe microscopy, this frequency shift is often measured using a phase-locked loop.

In this work, we moved the tip over a surface at a constant height, while self oscillating the cantilever. For each X and Y location, the cantilever motion was recorded by the DAQ for ∼5 ms. This data was Fourier transformed, and the frequency with the largest amplitude was read out to provide a frequency shift a particular location. We referred to the resulting image as a 'frequency-map.' Figure 3.11 shows an example of a frequency-map over a stripline surface.
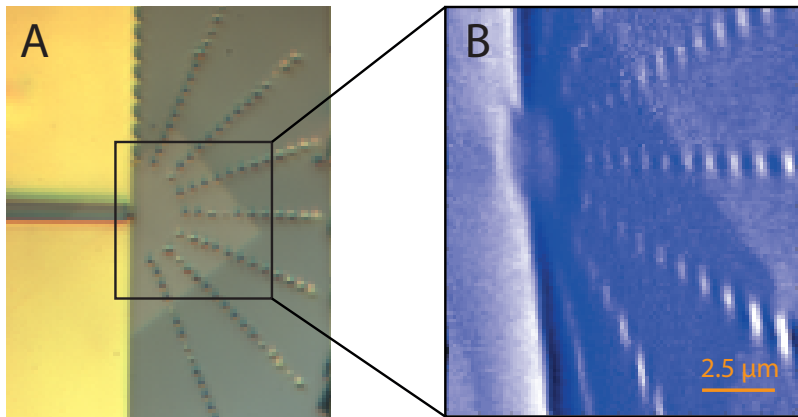
FIGURE 3.11: (a) An optical image of a stripline and rows of markers. Prior to placing the stripline in the MRFM, the surface was imaged with an SEM, and a tungsten compound $W(CO)_6$ was deposited with a focused ion beam on the stripline. (b) A frequency map of the area indicated in the optical image. The silicon dioxide surface was modified by the SEM and FIB, creating a square in both the optical and frequency images.

3.5.2 Approach curves

The frequency shift of the cantilever can provide topographical information if the sample is moved relative to the cantilever. However this is difficult to achieve with soft spring constants used with MRFM. Another way to measure the topography is to measure an approach curve. In this mode, the cantilever is self oscillated, while the surface is moved in small increments towards the cantilever. At each sample step, the cantilever frequency is measured as a function of z-position. The cantilever is influenced by tip-sample interactions, which shifts the frequency of the lever. The z-position is increased until the frequency of the cantilever is shifted by a setpoint amount, for example by 1000 Hz relative to the bare resonance frequency.

3.5.3 Touch-maps

A touch-map is obtained by recording a grid of approach curves. Each approach curve measures the z-height at which the cantilever 'touches' the surface. This touch is defined by a cantilever frequency shift relative to the free resonance frequency by a set amount, typically about 1000 Hz. When the cantilever tip gets very close to the surface, the frequency rapidly increases and decreases according to the interacting forces. When the frequency change is greater than a setpoint value, typically about 20% of the free resonance, the approach is stopped, and this height is recorded as the 'touch' height. Combining all of these heights in an XY grid provides a topographical image of the surface similar to an AFM scan. An example touch-map is shown in figure 3.12d.

Similar to AFM, a touch-map image is a convolution of the cantilever tip and substrate topography. Consequently, the spatial resolution of touch-maps are dependent on the probe sharpness. To obtain high resolution touch-maps, we use an array of cones fabricated from silicon as shown in 3.12a and 3.12b. The cantilever is approached to the cones, and a single cone is used to record a touch-map.

3.5.4 Higher harmonic frequency map

The fundamental frequency of the cantilever is designed to have a low spring constant, which is desirable for detecting weak forces. For this reason, it is also highly susceptible to non-contact friction, and must be driven with a large amplitude to overcome the damping and avoid 'jump-to-contact'. Conversely, it has been demonstrated that high spring constants are much better for achieving high resolution scanning probe images [63].
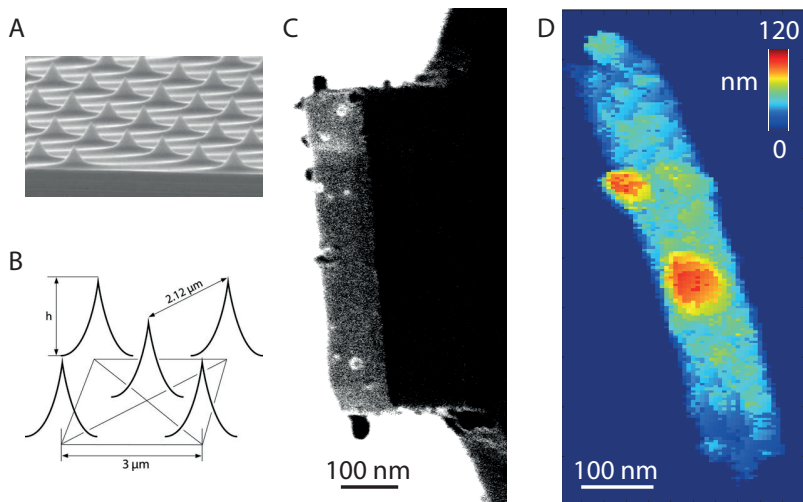
FIGURE 3.12: (a) SEM image of a silicon surface with an array of sharp cones fabricated by NT-MDT. (b) A schematic drawing of the cones on the surface. The height h are approximately 400 nm, and they are separated by about 3 μm. The cone sharpness is on the order of 50 nm. (c) SEM image of a cantilever with influenza viruses attached to the surface. The cantilever was cut with a FIB close to the end to create a larger surface area for the virus attachment. It then had gold evaporated on the surface, was UV irradiated, and the viruses were deposited with a micropippette. This image was taken by Hiroki Takahashi. (d) An example touch-map of a similar cantilever as in figure (c). The surface contains two viruses with heights close to 100 nm.

In order to circumvent the low spring constant of the fundamental resonance frequency, higher harmonics can be used for frequency map images. The cantilever harmonics have much higher spring constants as a result of having a lower mass participation. Figure 3.13(a) shows a frequency map using the first harmonic, and 3.13(b) shows an image using the second harmonic with all other variables kept constant. The second harmonic shows less contrast, indicating the higher harmonics are less susceptible to long
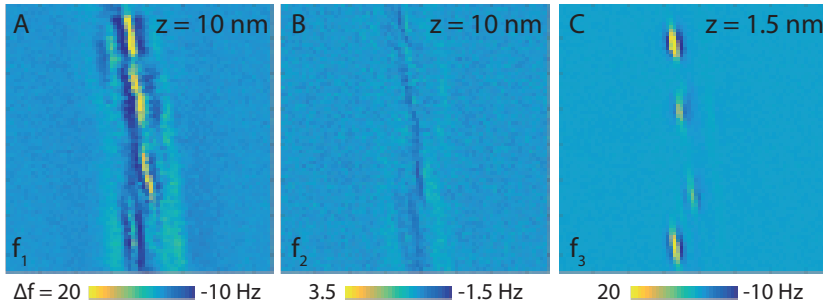
FIGURE 3.13: (a) A frequency map recorded while self oscillating the fundamental frequency ($\sim 2.7\,\text{kHz}$). The image was measured with a constant height ($10\,\text{nm}$) above a silicon cone. This image was recorded as close to the cone as possible before the dissipation could not be overcome by driving the cantilever harder. Four features are distinguishable, but the image is noisy. This can be attributed to the high dissipation caused by non-contact friction. The surface behind the four objects is also prominent. The displayed frequency range was decreased from the peak-to-peak values of $-26\,\text{Hz}$ and $37\,\text{Hz}$. (b) A frequency map using the first harmonic ($\sim 31\,\text{kHz}$). This image was recorded at the same height as panel (a). The first harmonic frequency is shifted by a fraction ($\sim 10\%$) compared to the fundamental mode, owing to the higher spring constant. This indicates that the first harmonic is much more sensitive to short range interactions compared to the fundamental frequency. (c) The higher spring constant of the first harmonic prevents snap-to-contact, and enables imaging up to $1.5\,\text{nm}$ from the surface. The four features are better resolved, and relative heights can be discerned from the colour contrast. The displayed frequency range was decreased from the peak-to-peak values of $-60\,\text{Hz}$ and $80\,\text{Hz}$.

range forces. When the cantilever is self oscillating with the second harmonic, it can approach much closer to the surface. Figure 3.13(c) shows a frequency map that was recorded at $1.5\,\text{nm}$ from the surface.

Chapter 4

Spin Signal

This chapter introduces nuclear magnetic resonance and how it is measured with MRFM. We tested different adiabatic passage profiles, and support our findings with numerical simulations.

4.1 Magnetic resonance

When a magnetic moment is placed in a magnetic field, the field produces a torque on the moment [64]. The torque τ is perpendicular to both the field direction and the magnetic moment

$$\vec{\tau} = \vec{\mu} \times \vec{H}$$

and causes the moment to align with the direction of the field. Many atomic nuclei have an additional angular momentum. Equating the torque with the rate of change of angular momentum J gives the equation of

motion of a nuclear magnetic moment

$$\frac{d\vec{J}}{dt} = \vec{\mu} \times \vec{H}$$

where $\vec{\mu} = \gamma \vec{J}$ giving

$$\frac{d\vec{\mu}}{dt} = \mu \times (\gamma \vec{H}) \ .$$

This equation of motion indicates that the spin precesses about the H field. The gyromagnetic ratio γ is the sensitivity of a spin to the magnetic field, and depends on the type of spin (for an electron $\gamma_e = 28.02\,\text{GHz/T}$, and for a proton $\gamma_n = 42.58\,\text{MHz/T}$). The frequency at which the spin precesses about the magnetic field is the Larmor frequency

$$\omega_L = \gamma_p H \ .$$

4.1.1 Thermal polarization

When a volume of nuclear spins is placed in a magnetic field, the spins exchange energy with the surrounding environment and reach a thermal equilibrium. In the case of spin $I = \frac{1}{2}$ nuclei, a fraction of the spins align (spin-up) with the field and the remaining spins align anti-parallel (spin-down). The energy difference between these two states is

$$\Delta E = \hbar \Delta \omega_L = \gamma \hbar B_0$$

where ω_L is the Larmor frequency, and B_0 is the magnetic field (Tesla). From statistical mechanics, the equilibrium distribution of the system is described by

$$\frac{N_+}{N_-} = e^{\Delta E / k_B T} = e^{-\gamma \hbar B_0 / k_B T} \tag{4.1}$$

where N_+ and N_- are the numbers of spins aligned parallel and anti-parallel respectively, and k_B is the Boltzmann constant.

The net difference of aligned and anti-aligned spins $\Delta N = N_+ - N_-$ produces a net magnetization vector, which is detectable using methods sensitive to magnetic fields like Nuclear magnetic resonance (NMR) and Magnetic resonance imaging. The magnetization can be described by a fractional population

$$P = \frac{\Delta N}{N_+ + N_-} = \frac{N_+ \left(1 - \frac{N_-}{N_+} \right)}{N_- \left(1 + \frac{N_-}{N_+} \right)} \ . \tag{4.2}$$

For a small magnetic field, the exponent in equation (4.1) can be approximated by

$$e^{\pm \frac{\mu B_0}{k_B T}} \approx 1 \pm \frac{\mu B_0}{k_B T} \ .$$

Substituting this into equation (4.2) provides a temperature dependent polarization

$$P = \frac{\mu B_0}{k_B T} \ ,$$

or in terms of the total number of spins contributing to the net magnetization vector

$$\overline{\Delta N} = N \frac{\mu B_0}{k_B T} \ . \tag{4.3}$$

Since this polarization is produced by the nuclear spins thermalizing with their environment, this is referred to as the thermal or Boltzmann polarization.

Equation (4.3) indicates that the number of spins contributing to the magnetization vector is exceedingly small because $\mu B_0 \ll k_B T$ for all practical fields and temperatures. This relationship is plotted in figure 4.1. For this reason, techniques like NMR and MRI rely on large spin volumes to detect

an appreciable signal. Typical MRI measurements are capable of detecting micron-to-millimeter scale, with state of the art resolution approaching $\sim$40 μm^3 [6]. Several MRFM measurements have demonstrated that the thermal polarization can be detected down to volumes of approximately $(100\,nm)^3$ [65]. In all of these experiments, the volume is large such that the number of spins is $\gtrsim 10^{11}$. For example, at 4 K, the number of spins detectable by the Boltzmann polarization is about 0.01% of that volume. At room temperature, this detectable volume would decrease by 2 more orders.

4.1.2   Statistical polarization

The thermal polarization of a large ensemble of spins can be treated with a constant polarization. In reality, thermal excitations cause spins to fluctuate between the up and down states. These fluctuations average out in large ensembles. However, as the volume of spins is decreased, spin fluctuations become more significant, and cause the thermal polarization to fluctuate by an appreciable amount [65]. Bloch predicted these fluctuations in 1946 [66], but the first experimental evidence of spin noise was not measured until 1985 with a Superconducting quantum interference device (SQUID) [67]. The first detection of spin noise at room temperature with an NMR spectrometer was made in 1989 [68].

For spin volumes smaller than $\sim(100\,nm)^3$ the thermal polarization becomes exceedingly small, and is dominated by statistical fluctuations [65]. This cross-over region at 4 K is plotted in figure 4.1. With resolution exceeding $\sim(100\,nm)^3$, the variance of these statistical fluctuations is the preferred signal for imaging [16]. The nuclear spin noise is characterized by slow fluctuations of net magnetization, with time constants typically
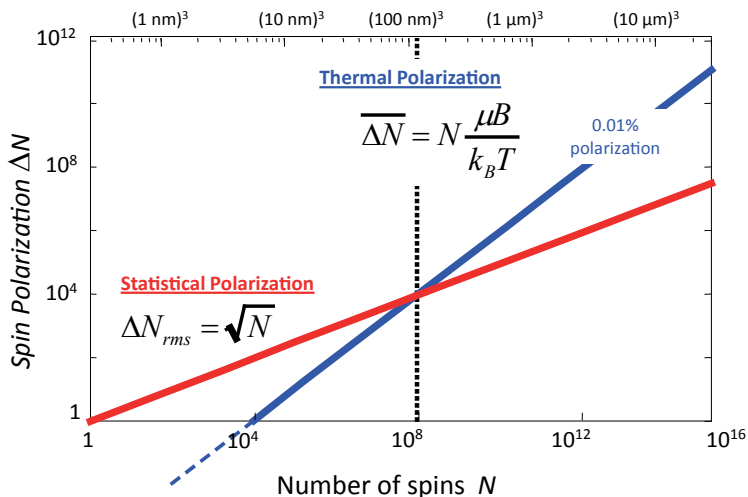
FIGURE 4.1: Comparison of the number of spins contributing to nuclear magnetic resonance for thermal polarization (Boltzmann) and statistical polarization. This plot corresponds ^{1}H nuclear spins at $T = 4\,\text{K}$ and magnetic field $B = 3\,\text{T}$. A Boltzmann polarization detected signal consists of the net nuclear spins that do not cancel, whereas statistical polarization scales with the total number of spins. For spin ensembles larger than $(100\,\text{nm})^3$, thermal polarization has many more contributing spins. However, for ensembles smaller than $(100\,\text{nm})^3$, the Boltzmann polarization becomes small, and in fact is less than 1 spin below $(5\,\text{nm})^3$. Therefore, statistical polarization has a significantly larger number of spins contributing to the spin signal. Image adapted from [15].

ranging between $\tau_{\text{m}} = 10\,\text{ms} - 10\,\text{s}$. These fluctuations are dictated by the spin-lattice relaxation time of a spin in an alternating magnetic field.

4.1.3 Spin relaxation

Statistical fluctuations are the result of spins absorbing or losing energy, which displaces the thermal polarization from equilibrium. The primary

relaxation channel that drives the system back towards equilibrium is spin-lattice relaxation (or longitudinal relaxation), resulting from spins interacting with their surrounding lattice. This relaxation mechanism can be characterized by applying an RF pulse to excite the system out of equilibrium, and observing the time scale required for the thermal polarization to recover. In an NMR experiment, this corresponds to applying a $\frac{\pi}{2}$ pulse to tilt the thermal population into the transverse (x-y) plane, and measuring the gradual recovery of the thermal polarization along the z-axis. The time scale required for $(1 - \frac{1}{e})$ (or $\sim$63%) to return along the z-axis is characterized by the time scale T_1.

4.1.4 Continuous wave spin inversions

An RF pulse is a time varying magnetic field that oscillates in the x-y plane [64],

$$\vec{B}_1(t) = B_1\Big(cos(\omega_z t)\hat{\mathbf{i}} + sin(\omega_z t)\hat{\mathbf{j}}\Big)$$

where B_1 is the pulse amplitude (mT), and oscillates at a frequency ω_z in the clockwise ($\omega_z = +\omega$) or counterclockwise ($\omega_z = -\omega$). The RF pulse modifies the equation of motion of a spin in an external field

$$\frac{d\mu}{dt} = \vec{\mu} \times \gamma\Big[\vec{B}_o + \vec{B}_1(t)\Big] \tag{4.4}$$

where $\vec{B}_o = B_o\hat{\mathbf{k}}$. A more convenient way to describe this system is by converting to a reference frame ($\hat{\mathbf{i}}'$ and $\hat{\mathbf{j}}'$) that rotates around the $\hat{\mathbf{k}}$ axis. The stationary reference frame can be described by a time dependent rotating angle $\theta(t)$

$$\hat{\mathbf{i}}(t) = \Big(\cos\theta(t), \sin\theta(t)\Big)$$

$$\hat{\mathbf{j}}(t) = \Big(-\sin\theta(t), \cos\theta(t)\Big)$$
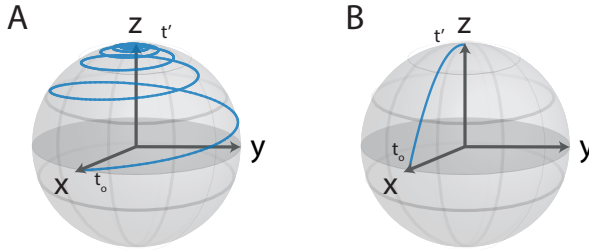
FIGURE 4.2: (a) Stationary reference frame: a spin begins oriented at an initial position at time $t = t_0$. The external field applies a torque on the spin, causing it to precesses about the z-axis with a continuously smaller amplitude. At $t = t'$, the spin is oriented along the z-axis. (b) In the rotating reference frame, the coordinate system revolves at the same frequency as the spin precession ($\Omega = \omega_0$), such that spin relaxation is reduced to a 2-dimensional motion.

The time derivative of $\hat{\mathbf{i}}$ and $\hat{\mathbf{j}}$ are

$$\hat{\mathbf{i}}' = \frac{d\hat{\mathbf{i}}(t)}{dt} = \Omega\Big(-\sin\theta(t), \cos\theta(t) \Big) = \Omega\hat{\mathbf{j}}(t)$$

$$\hat{\mathbf{j}}' = \frac{d\hat{\mathbf{j}}(t)}{dt} = \Omega\Big(-\cos\theta(t), -\sin\theta(t) \Big) = -\Omega\hat{\mathbf{i}}(t)$$

where $\Omega \equiv \frac{d\theta(t)}{dt}$. Changing the basis from the stationary reference frame

$$\frac{d\mu}{dt} = \vec{\mu} \times \Big[(\omega_z + \gamma B_o)\hat{\mathbf{k}} + \gamma B_1(t)\hat{\mathbf{i}} \Big]$$

to the rotating reference frame eliminates the time dependence such that

$$\frac{d\mu}{dt} = \vec{\mu} \times \gamma\Big[(B_o - \frac{\omega}{\gamma})\hat{\mathbf{k}} + B_1\hat{\mathbf{i}} \Big] \tag{4.5}$$
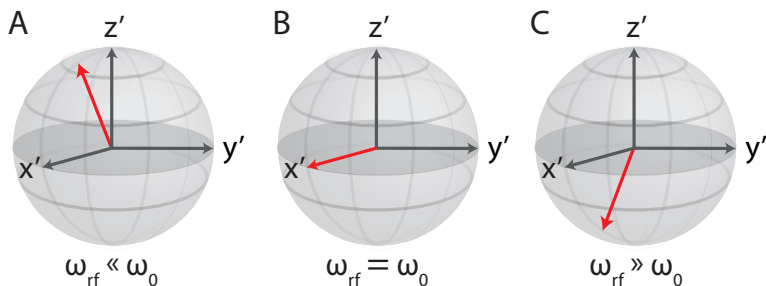
FIGURE 4.3: Effective magnetic field vector in the rotating reference frame for three different frequencies: (a) $\omega_{rf} \ll \omega_0$, (b) $\omega_{rf} = \omega_0$, and (c) $\omega_{rf} \gg \omega_0$

The square brackets can be described as an effective field vector $\vec{B}_{eff}$ such that

$$\frac{d\mu}{dt} = \vec{\mu} \times \gamma \vec{B}_{eff} \qquad (4.6)$$

$$\vec{B}_{eff} = (B_o - \frac{\omega}{\gamma})\hat{\mathbf{k}}' + B_1 \hat{\mathbf{i}}' \ . \qquad (4.7)$$

Equation (4.6) indicates that in the rotating reference frame, a nuclear spin feels a static effective field $\vec{B}_{eff}$. Therefore, the spin precesses about a cone in the direction of $\vec{B}_{eff}$ at an angular frequency $\omega = \gamma B_{eff}$ as depicted in figure 4.4.

Equation (4.6) also indicates that applying a $\vec{B_1} = B_1 \hat{\mathbf{x}}$ pulse on resonance, such that $\omega = \gamma B_o$, will make the spin precess perpendicular to the x-axis (in the y-z plane). The magnetization vector will continue to precess for the duration of a pulse, called a Rabi oscillation. The angle ϕ swept by the magnetization vector is

$$\phi = \gamma B_1 t_w$$
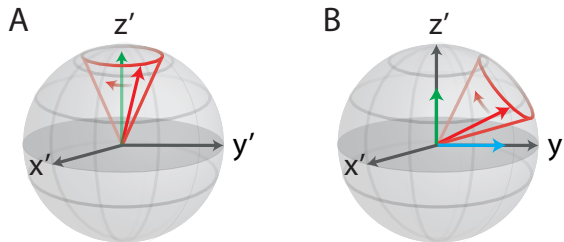
FIGURE 4.4: (a) In the rotating reference frame, a nuclear spin (red) precesses about the effective magnetic field vector $\vec{B}_{eff}$. When no B_1 pulse is applied, the spin precesses about the z-axis due to the external magnetic field B_{ext} (green). (b) When a B_1 pulse (blue) is applied, the effective field is tilted according to equation (4.7)

where B_1 is the pulse amplitude, and t_w is the pulse duration. Consequently, the magnetization vector can be inverted from $+z$ to $-z$ by applying a resonant pulse for a duration of t_w such that $\phi = \pi, 3\pi, ...$ This is referred to as a '180-degree-pulse' or a 'π pulse.'

4.1.5 Adiabatic spin inversions

Early NMR experiments inverted thermal polarizations (a magnetization vector) with slowly varying B_1 fields [66, 69]. These sweeps were accomplished by continuously irradiating with a fixed RF frequency and modulating the amplitude. By sweeping sufficiently slow, the magnetization vector remains in equilibrium with the effective field despite the time dependent rotation. Conversely, the sweep must be completed fast enough such that the spins do not relax by T_1 and T_2 decay channels.

Despite the advancement of RF generation hardware, adiabatic inversions are still widely used. These pulses provide a convenient method of exciting broad frequency bandwidths with a high degree of tolerance for RF field

inhomogeneities [70]. Modern NMR experiments can produce adiabatic sweeps with fixed amplitudes and modulating phase

$$\phi(t) = \int_0^{t_0} \Big(\omega_{RF}(t') - \omega_c \Big) dt' + \phi(0)$$

where ω_c is the center angular frequency of the inversion bandwidth (rad/s), $\phi(0)$ is the initial phase at $t = 0$, and ω_{RF} is the time varying angular frequency of the RF field. An adiabatic passage inverts spins that possess Larmor frequencies within the pulse bandwidth $\omega_{RF} = \omega_c \pm \omega_{dev}$. This corresponds to modulating the RF frequency (with continuous phase) by

$$\omega_c - \omega_{RF}(t) = \frac{d\phi}{dt} \ .$$

Therefore, the effective field vector in the rotating reference frame is time dependent

$$\vec{\omega}_{eff}(t) = \omega_{eff}(t)\Big(-\omega_1(t), 0, \Delta\omega + \dot{\phi}(t) \Big) \ .$$

The angle of the effective field relative to the rotating reference frame is

$$\theta(t) = tan^{-1}\Big[\frac{\Delta\omega + \dot{\phi}(t)}{\omega_1(t)} \Big] \ .$$

This is illustrated in figure 4.5(a), where an RF pulse applied along the y-axis creates an effective field that rotates in the x-z plane. In order for the spins to follow the pulse, the effective field rotation speed must be slower than the precession rate of the magnetization vector

$$\Big| \frac{d}{dt}\theta(t) \Big| \ll \omega_{eff} \ .$$

This rate of rotation is quantifiable by defining the adiabaticity A

$$A(t) = \frac{\omega_{eff}}{\frac{d}{dt}\theta(t)} \ .$$

Increasing A for an entire sweep duration improves the spin inversion fidelity, and therefore ensures that the spins follow the effective field vector. Furthermore, to ensure that the entire bandwidth of spins is inverted ($\omega_c \pm \omega_{dev}$), the sweep frequency must begin and end far from the bandwidth extents

$$\omega_{rf}(0) \ll \omega_c - \omega_{dev}$$

$$\omega_{rf}(t_0) \gg \omega_c + \omega_{dev} \; .$$

The adiabatic regime is typically defined for NMR as $A > 1$, but MRFM generally requires a more stringent $A > 5$. This can be illustrated by defining an additional reference frame that rotates with the effective magnetic field vector, as shown in figure 4.5(a). In this reference frame ($\hat{\mathbf{i}}'', \hat{\mathbf{j}}'', \hat{\mathbf{k}}''$), the effective field vector remains along the z-axis, while the magnetization vector sweeps out a cone, as illustrated in figure 4.5(b). The magnetization vector sweeps a larger cone dependent on the pulse speed, decreasing the 'force' applied by the effective field. Spins with higher gyromagnetic ratios are less affected by the effective field sweep rate.

4.2 MRFM spin detection

Force detection was the first general purpose technique capable of detecting a single electron spin. Rugar et al. demonstrated this by attaching a magnet to a cantilever, and approaching it to a single silicon danging bond, known as an E' center [71]. This was a milestone experiment that paved the way for mechanically detecting nuclear spin signals with MRFM. The magnetic moment of an electron spin ($\mu_e = 9.29 \cdot 10^{-24}$ J/T) is approximately 660 times larger than that of a single proton ($\mu_p = 1.41 \cdot 10^{-26}$ J/T). Therefore, detecting a single nuclear spin requires improving the sensitivity of MRFM by over two orders of magnitude to achieve similar SNR.
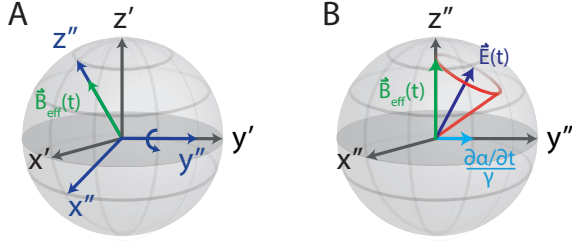
FIGURE 4.5: (a) In the rotating reference frame $(\hat{\mathbf{i}}', \hat{\mathbf{j}}', \hat{\mathbf{k}}')$, a $\vec{B}_1$ field applied along the y-axis produces an effective field $\vec{B}_{eff}$ that rotates in the x-z plane. An additional reference frame $(\hat{\mathbf{i}}'', \hat{\mathbf{j}}'', \hat{\mathbf{k}}'')$ can be defined that rotates in the x-z plane with B_{eff}. (b) In the effective field rotating reference frame $(\hat{\mathbf{i}}'', \hat{\mathbf{j}}'', \hat{\mathbf{k}}'')$, the magnetization vector sweeps a cone dependent on the pulse frequency modulation rate. The slower the pulse, the smaller the cone, and the more the magnetization vector follows the effective field.

4.2.1 Force detection

When a spin is placed in a magnetic field gradient, it experiences a static force

$$\vec{F} = -\vec{\nabla}E = \vec{\nabla}(\vec{\mu} \cdot \vec{B}) \tag{4.8}$$

where $\vec{\mu}$ is the magnetic moment of the spin ($\mu_p = 1.51 \cdot 10^{-26}\,\mathrm{Am^2}$ or J/T), and $\vec{B}$ is the magnetic field. In our version of MRFM, a sample is attached to the end of a cantilever, which is approached to a nano-magnet that produces a field gradient. The cantilever is most compliant to forces in the deflection direction (defined as the x-axis)

$$F_x = \frac{d}{dx}(\vec{\mu} \cdot \vec{B}) = \mu_z \frac{dB_z}{dx}$$

where μ_z is aligned by an external magnetic field along the z-axis. Consequently, the force is strongly dependent on the magnitude of the $\frac{dB_z}{dx}$ field gradient. However, this static force is extremely small ($\sim 10^{-20}\,\mathrm{N}$),

and is difficult to detect with low frequency noise sources that are always present.

Cantilevers are extremely sensitive to alternating forces that match their mechanical resonance. Furthermore, mechanical oscillators with frequencies $\gtrsim$2000 Hz evade low frequency detector noise sources. Previous work has demonstrated force sensitivity as small as $1\,\mathrm{aN}/\sqrt{\mathrm{Hz}}$ [45]. An alternating force can be produced from equation (4.8) by periodically inverting the magnetic moment direction. When the spin inversion frequency matches the cantilever resonance, the oscillating spin polarization drives the cantilever motion. Spin inversions have been shown to be most controllable with adiabatic passages.

The SNR of an MRFM experiment directly determines the required time to detect a signal. The averaging time required to detect the force of a single electron spin was about 12 hours per data point, owing to the single-shot SNR of 0.06. This SNR limitation precludes the possibility of observing the dynamics of a single electron spin. However, E' centers have been shown to have a correlation time of 760 ms, and it was shown that a sufficiently large signal is possible with $\sim$70 electrons to observe single shot readout [72].

In the TMV experiment, the magnetic field gradient was significantly improved over the single electron measurement [73]. However, many more data points were required to produce a 3-dimensional image with sufficiently high enough voxels. For this reason, spatial resolution was compromised to record enough data points. The detection volume per voxel was on the order of $(5\,\mathrm{nm})^3$, corresponding to about $20,000$ nuclear spins, and each data point was recorded for 1 minute. Therefore, improvements in SNR speed up data acquisition, as well as spatial resolution. In this
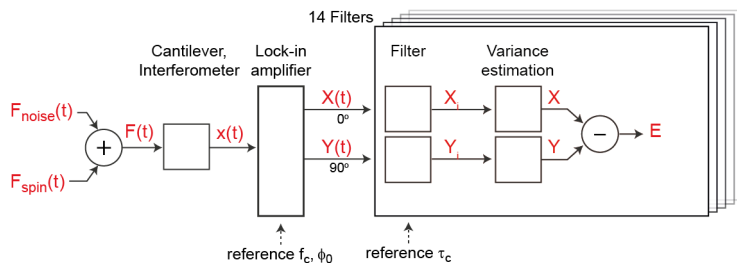
FIGURE 4.6: Two channel MRFM signal detection protocol. The cantilever position x(t) is influenced by forces by both thermal noise and the spin signal. A lock-in amplifier detects the phase of the cantilever motion relative to the RF pulses applied to the strip line. The in-phase (X_0) and quadrature (X_{90}) channels are each filtered by 2

voxel size regime, the spin noise provides a substantially larger signal than the thermal polarization.

4.2.2 Signal pathway

The cantilever motion is influenced (see figure 4.6) by both undesired thermal noise $F_{\mathrm{noise}}(t)$, and a typically much smaller force generated by the desired nuclear spin noise $F_{\mathrm{spin}}(t)$. These forces collectively influence the cantilever motion, which is then measured by the laser interferometer, providing a positional dependent signal $x(t)$.

In order to detect the weak spin noise, the cantilever motion is measured with lock-in amplification. The in-phase channel $X_0(t)$ receives both the spin signal and thermal noise, while the quadrature channel $X_{90}(t)$ receives only thermal noise. Figure 4.7(a) shows one minute traces of $X_0(t)$ and $X_{90}(t)$, and figure 4.7(b) shows a five second segment of the two channels. The data from the two lock-in channels are filtered using a bank of 14
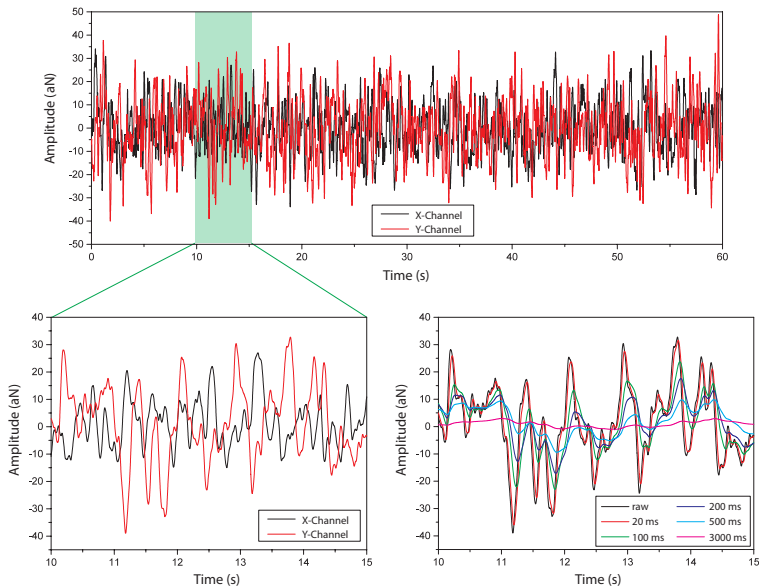
FIGURE 4.7: (a) Traces of X_0 and X_{90} channels recorded for 60 seconds. (b) A zoom in on 5 seconds of the lockin data. (c) The X_0 trace with five of the 14 filters applied to the data.

filters. Figure 4.7(c) shows examples of five of the filters applied to the X_{90} data.

The spin noise is characterized by statistical fluctuations with correlation times ranging from 20 ms to 3 s. In order to detect these fluctuations, the variance σ of the cantilever motion is calculated for the filtered lock-in channel data

$$\sigma = \frac{\sum_i (s_i^2)}{n} - \frac{(\sum_i s_i)^2}{n^2}$$

where s_i corresponds to ith data point of a lock-in trace, and n is the number of statistically independent samples of a filter

$$n = \frac{2s^2}{\sigma_s^2} + 1$$

where s and σ_s are the exact and measured variances of the spin noise respectively. Since the cantilever is driven by thermal noise and fluctuating spin noise, the mean ($\sum_i s_i$) should yield zero after long averaging times since there is not a coherent drive. A mean value greater than $\sim 0.05\,\text{V}$ typically indicates that the cantilever is electrostatically driven by RF pulses. Figure 4.8 shows an example of the sum-of-squares, squared-sum, and variance of both X_0 and X_{90} channels, using the data from figure 4.7.

The X_0 and X_{90} channels correspond to

$$X_0 = \sigma^2 \cos^2(\phi) + \sigma_{\text{th}}^2 \tag{4.9}$$

$$X_{90} = \sigma^2 \sin^2(\phi) + \sigma_{\text{th}}^2 \tag{4.10}$$

where σ^2 is the variance of the spin noise, and σ_{th}^2 is the thermal noise. When the spin signal is correctly directed, then $\phi = 0$. Subtracting the calculated variance of both channels produces the spin signal ($E = X_0 - X_{90}$). The SNR ratio can be optimized by choosing a lock-in filter time constant that is close to the intrinsic correlation time τ_{m}. We achieved this by calculating variances for a bank of 14 filters and post-selecting the desired filter.

The SNR of this detection protocol suffers when the signal is not entirely directed in the in-phase channel. In section 4.2.3, we have extended this method to detect the signal in both X_0 and X_{90} quadratures while subtracting the noise.
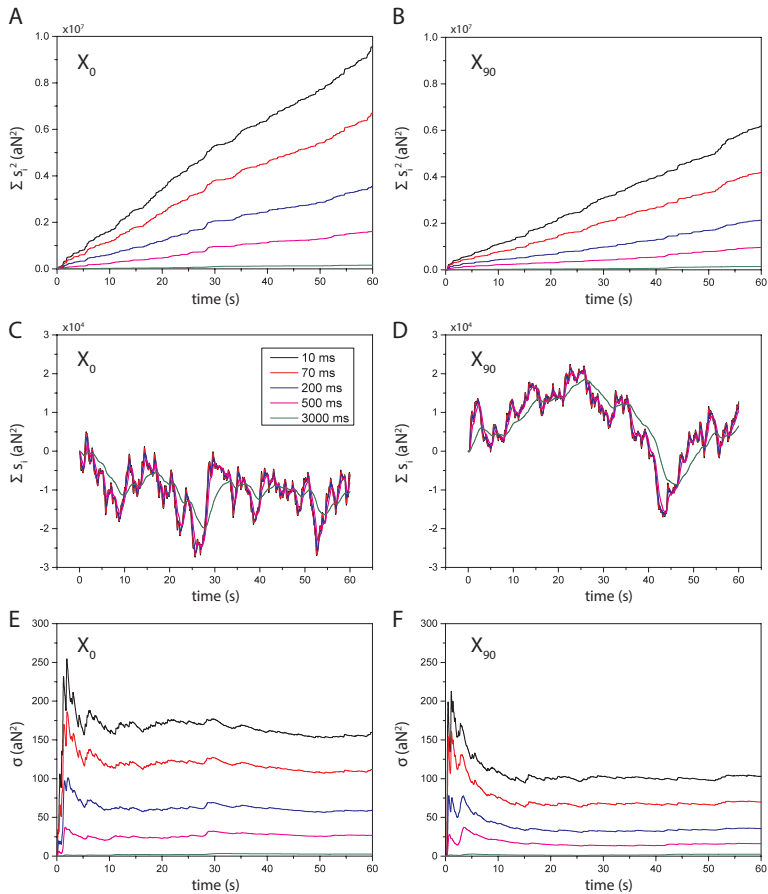
FIGURE 4.8: Sum-of-squares of (a) X_0 and (b) X_{90} vs. time. Squared-sum values of (c) X_0 and (d) X_{90} vs. time. The variances of (e) X_0 and (f) X_{90} vs. time.
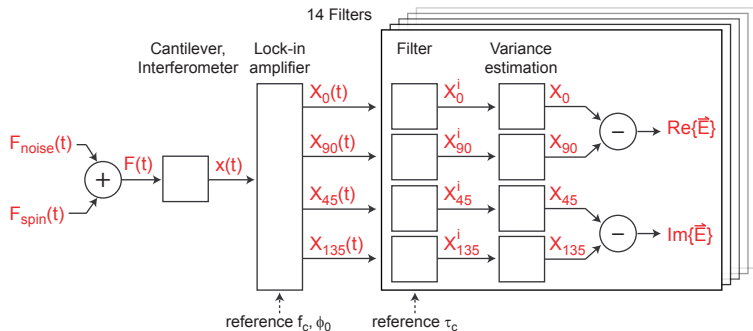
FIGURE 4.9: Schematic of signal acquisition protocol. $x(t)$ denotes the position of the cantilever as a function of time, influenced by both thermal F_{noise} and spin F_{spin} noise. $X_0(t)$, $X_{45}(t)$, $X_{90}(t)$, and $X_{135}(t)$ denote the cantilever motion amplitudes with different phases, which are then filtered with 14 different time constants between 20 ms and 3 s. X_0^i, X_{45}^i, X_{90}^i, and X_{135}^i are amplitudes filtered by the ith filter. Finally, X_0, X_{45}, X_{90}, and X_{135} stand for the variance of those amplitudes over the averaging time of the experiment (converted into units of squared force).

4.2.3 Four quadrant detection

Calculating the variance requires squaring the input signals, causing information concerning the sign (and hence the phase) of the signal to be lost. However, the full phase of the spin signal can be retrieved by using a four-channel lock-in detection, where the interferometer signal is demodulated at the phases 0°, 45°, 90° and 135°. (A conventional lock-in amplifier would only demodulate at 0° and 90°). To illustrate this, consider measuring a spin signal with variance σ_{F}^2 and phase ϕ in the presence of thermal noise with variance σ_{th}^2. If we denote the four demodulated signals by X_0,

X_{45}, X_{90}, and X_{135},

$$X_0 = \sigma_F^2 \cos^2(\phi) + \sigma_{th}^2 \tag{4.11}$$

$$X_{45} = \sigma_F^2 \cos^2(\phi - \pi/4) + \sigma_{th}^2 \tag{4.12}$$

$$X_{90} = \sigma_F^2 \sin^2(\phi) + \sigma_{th}^2 \tag{4.13}$$

$$X_{135} = \sigma_F^2 \sin^2(\phi - \pi/4) + \sigma_{th}^2. \tag{4.14}$$

Note that the thermal noise, being incoherent, is equally distributed over the phase space. We can subtract the thermal noise signal contributions by forming the differences

$$X_0 - X_{90} = \sigma_F^2 \Big(\cos^2(\phi) - \sin^2(\phi) \Big) = \sigma_F^2 \cos(2\phi) \tag{4.15}$$

$$X_{45} - X_{135} = \sigma_F^2 \Big(\cos^2(\phi - \pi/4) - \sin^2(\phi - \pi/4) \Big) = \sigma_F^2 \sin(2\phi). \tag{4.16}$$

These two terms correspond to the real and imaginary parts of a signal E,

$$E = (X_0 - X_{90}) + i(X_{45} - X_{135}) = \sigma_F^2 e^{i2\phi} \tag{4.17}$$

4.2.4   FPGA implementation and analysis

We implemented the four-channel lock-in detection technique by first demodulating by a conventional two-channel lock-in amplifier (SR830, Stanford Research), and then rotating lock-in outputs by 45° on an FPGA controller. The same FPGA then also performed the filtering and variance estimation to produce X_0, X_{45}, X_{90}, and X_{135}.

For all imaging scans, two additional corrections were applied in order to account for position-dependent changes in cantilever gain (represented by the damped quality factor) and phase. Both parameters were measured at each location prior to data collection. For typical one dimensional scans,

we found Q_{damped} to vary between $200 - 500$ while changes in phase were only within a few percent. Since these changes vary slowly with position, roughly with a length scale similar to the tip-sample spacing, they can be easily corrected for by low-order polynomial fit or heavy low-pass filtering. Note that these corrections apply to all imaging scans, including both single signal measurements and multiplexed measurements.

4.3   MRFM pulse sequences

In order to drive the cantilever with nuclear spin inversions, spins must be modulated at the cantilever resonance frequency $f_c = 1/T$. Typical MRFM cantilevers oscillate at approximately $5\,\text{kHz}$ ($T = 0.2\,\text{ms}$). The spins must be inverted twice per cantilever period, which requires each adiabatic passage to be completed within $0.1\,\text{ms}$. For a high frequency bandwidth of spins, for example $\gtrsim 1\,\text{MHz}$, this is a short time period.

The short time period per adiabatic passage can be compensated for using high B_1 amplitudes. MRFM experiments originally used inductive coils to produce B_1 fields. More recent work has used strip lines to produce significantly higher amplitudes, and have been shown to not limit the τ_{m} [39]. This enables considerably higher adiabaticity, and also enables the ability to invert bandwidths of Larmor frequencies up to several MHz.

The shape of adiabatic pulses also significantly affect adiabaticity. In this work, two different frequency/amplitude modulation shapes were used: linear/trapezoid and secant/hyperbolic tangent pulse sweeps. Depending on the profile shape, the pulses can also be overlapped to increase the amount of time per pulse.

4.3.1   Linear sweeps

In past MRFM experiments, the most commonly used adiabatic sweep profile has been linear frequency sweeps with trapezoidal amplitude modulation. This is partially owing to ease of implementation and being straightforward to interpret signals.

A linear frequency sweep is defined by

$$\omega_1 = \frac{d\theta(t)}{dt} = -kt$$

where $-t_0 \leq t \leq t_0$ and k is a linear sweep rate [74]. If k is sufficiently small, then the adiabatic condition is met, but changes as a function of time

$$A(t) = \frac{\left[\omega_1^2 + \dot\theta(t)\right]^{3/2}}{k\omega_1} \ .$$

This equation indicates that the adiabaticity is minimum on resonance, and therefore a large B_1 amplitude is required for the pulse to coherently invert spins.

Figure 4.10 shows a schematic representation of a linear adiabatic sweep for inverting nuclear spins with a Larmor frequency of 118 MHz. The B_1 amplitude is initially at 0, and is ramped up to 4 mT at constant frequency. This amplitude ramping produces a y-component in the effective field, and causes the spins to rotate within the Bloch sphere along to the x-axis. Between steps 1 and 3, the amplitude remains constant while the frequency is swept from $f_c - f_{dev}$ to $f_c + f_{dev}$ (or vice versa), causing the effective field to rotate through the XY plane at step 2. A full inversion is completed by ramping the amplitude back to 0.

The trapezoidal amplitude modulation is used to ensure that the spins decouple from the RF field before and after an inversion. Any discontinuity
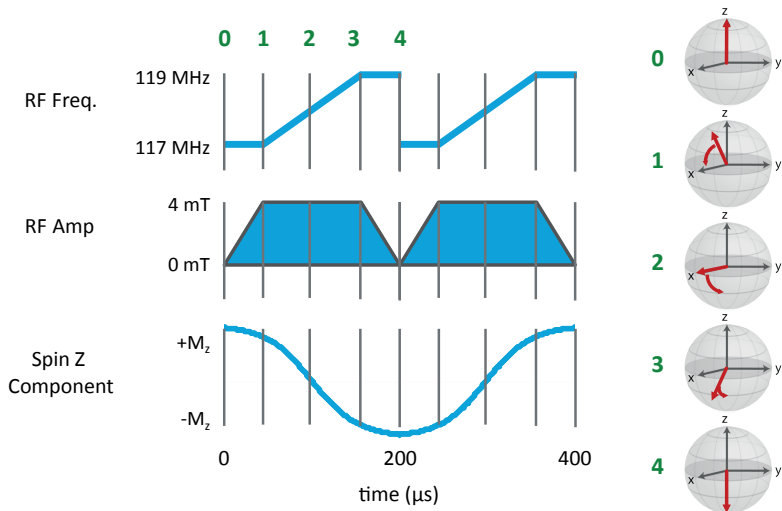
FIGURE 4.10: Linear spin inversion protocol: the amplitude (b) is modulated with a trapezoid profile, while the frequency is linearly swept (a) when the amplitude is at its maximum. This inversion profile causes the spin to rotate between the $\pm z$ poles of the Bloch sphere. Two inversions within a cantilever period produces a force on the cantilever dependent on the number of spins inverted.

in phase within a pulse, or between two pulses will prevent the spins from following the effective field. For the same reason, the frequency and amplitude must be ramped slow enough to abide by the adiabatic condition.

Ideally the RF fields applied to both sides of the stripline are 180° out of phase, and consequently no electric field is produced. However, the cantilever is extremely sensitive to any electrostatic forces, and it is unlikely to fully cancel out the entire electric field. In order to avoid this issue, pulses are swept unidirectionally such that electrostatics are produced at $2f_c$, and are therefore far from resonance. However, large amplitudes at
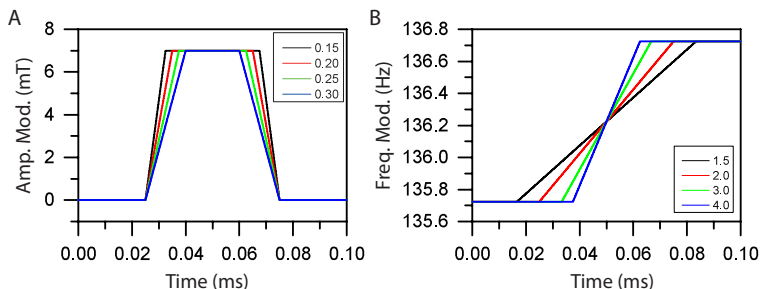
FIGURE 4.11: Profiles of an adiabatic passage with (a) trapezoidal amplitude and (b) linear frequency modulation for inverting spins at 5 kHz. Four frequency modulation slopes are shown in (b), which change the total pulse time. The amplitude modulation ramp rate (four shown) corresponds to the fraction of the total pulse time used for ramping one side of the pulse. In (a), the frequency slope was set to 2, thus the total pulse time is half of 0.1 ms.

$2f_c$ can parametrically drive the cantilever, causing squeezing of one quadrature relative to the other. In turn, this would cause thermal noise to be misbalanced between the quadratures, and consequently not fully cancel out.

4.3.2 Hyperbolic secant sweeps

Linear sweeps increase the amount of time with maximum amplitude. However, the beginning and end of a pulse is abrupt causing a large portion of spins to not follow the effective field. An alternative phase dependent profile can be derived by requiring constant adiabaticity throughout the sweep [74]

$$A(t) = a \ .$$

Therefore, the adiabatic condition can be written as

$$a\frac{d\theta}{dt} = \omega_{eff} \ .$$

Additionally,

$$\omega_{eff}\cos\theta = \omega_1$$

$$\omega_{eff}\sin\theta = \dot{\phi}$$

combining these equations allows us to derive a function for the phase modulation

$$\dot{\phi}(t) = \frac{-\omega_1^2 t}{\sqrt{a^2 - \omega_1^2 t^2}} \ .$$

By integrating this equation, we obtain

$$\phi(t) = -\sqrt{a^2 - \omega_1^2 t^2} + a$$

or alternatively writing in terms of the amplitude modulation

$$\omega_1(t) = \omega_{rf}\operatorname{sech}(\beta t)$$

and the frequency modulation

$$\omega_{RF}(t) - \omega_c = \frac{d\phi}{dt} = -\omega_{dev}\tanh(\beta t)$$

where β is truncation factor. The amplitude modulation is plotted as a function of β in figure 4.12a and the frequency modulation in 4.12b.

4.3.3   Comparison of adiabatic profiles for MRFM

Figure 4.13 shows a comparison of spin signals measured with linear and hyperbolic secant inversion profiles. A high FM deviation inverts a large
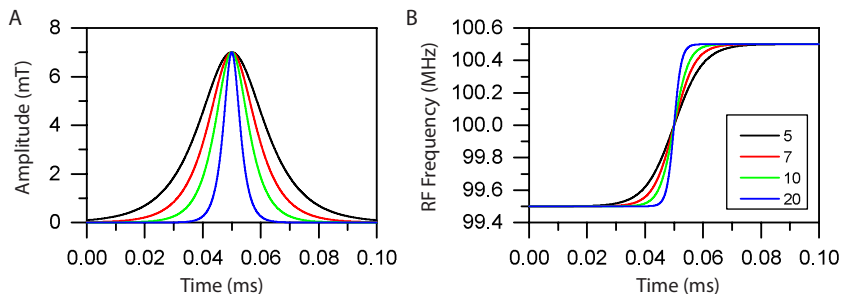
FIGURE 4.12: (a) Amplitude modulation and (b) frequency modulation of the hyperbolic secant adiabatic sweep. Each trace is plotted with a different β, demonstrating the decrease in pulse width as a function of β.

bandwidth of Larmor frequencies, and therefore produces a large spin signal. The linear profile (figure 4.13A) is capable of inverting large bandwidths of spins with low RF power. In contrast, the hyperbolic secant (shown in figure 4.13B) requires higher RF power to invert similar bandwidths as the linear profile.

Inverting a large bandwidth of spins is desired when initially searching for a spin signal with a new cantilever or magnet. However, the imaging resolution is improved by decreasing the resonance slice thickness, corresponding to low FM deviations. When the FM deviation of the linear sweeps is reduced below ∼500 kHz, the inversion efficiency is poor. This is reflected in a drastic decrease in spin signal below ∼500 kHz, which is not proportional to the decrease in the number of spins inverted. In contrast, the hyperbolic secant more efficiently inverts low bandwidths of spins.
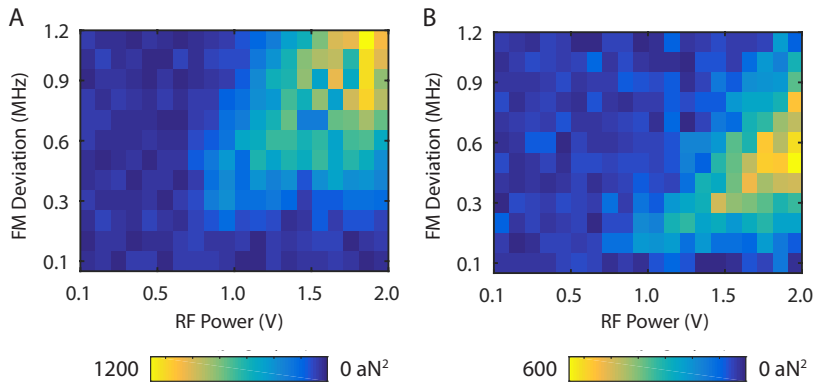
FIGURE 4.13: (a) Adiabatic plot using a linear/trapezoid pulse and (b) hyperbolic secant inversion profiles by plotting FM deviation ω_{dev} vs. RF power B_1. The linear profile is capable of inverting large frequency bandwidths with low power. However, since linear sweeps poorly invert the beginning and end of the frequency bandwidth, they poorly invert small bandwidths, such as below 300 kHz. Conversely, the hyperbolic secant requires a high RF power to invert a large bandwidth, but efficiently inverts low spin bandwidths.

4.4 Adiabatic sweep simulations

4.4.1 Computational method

Adiabatic passages can be simulated by numerical propagation of density matrices. The hamiltonian in the rotating reference frame in units of Hz is

$$H(t) = \Big(f_z(t) - f_L \Big) S_z - \gamma B_1(t) S_x$$

where $f_z(t)$ and $B_1(t)$ are the frequency and amplitude profiles of the adiabatic sweep respectively. f_L is the Larmor frequency of a spin, S_z and

S_x are the Pauli spin matrices

$$S_x = \begin{pmatrix} 0 & 1 \\ 1 & 0 \end{pmatrix}$$

$$S_y = \begin{pmatrix} 0 & -i \\ i & 0 \end{pmatrix}$$

$$S_z = \begin{pmatrix} 1 & 0 \\ 0 & -1 \end{pmatrix}$$

The hamiltonian is stepped in time by increments of dt using the propagator

$$U = e^{-i2\pi H dt}$$

which increments the density matrix Σ to Σ' by calculating

$$\Sigma' = U\Sigma U^\dagger \ .$$

A simulation begins by defining the density matrix in an initial state, for example $\Sigma = S_z$. The hamiltonian is propagated for the duration of an adiabatic sweep with approximately $10,000$ time steps. The expectation value (E_x, E_y, E_z) of the spin along the x, y, and z axes can be determined at a time step by calculating the trace of Σ'

$$E_x = \Re(\mathrm{Tr}\{\Sigma S_x\})$$

$$E_y = \Re(\mathrm{Tr}\{\Sigma S_y\})$$

$$E_z = \Re(\mathrm{Tr}\{\Sigma S_z\})$$
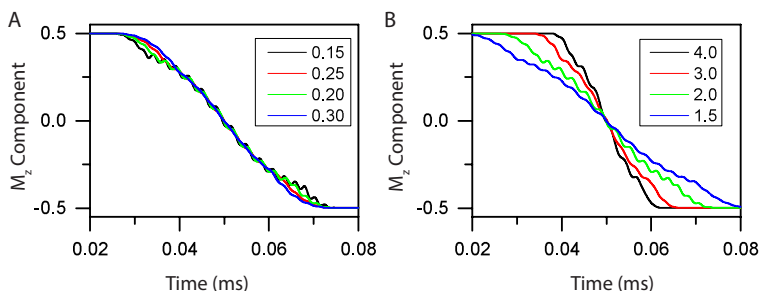
FIGURE 4.14: Simulations of a nuclear spin inverted by linear frequency modulation and trapezoidal amplitude. The spin was inverted at $5\,\text{kHz}$, with an amplitude of $7\,\text{mT}$. The simulation was performed with $10,000$ time steps. (a) A spin is initialized in the $M_z = +0.5$ state, and inverted with various ramp values. The pulse slope was set to two for each trace. (b) The ramp parameter was set constant (0.2), and the slope was varied.

4.4.2   Results

Figure 4.14 shows the results of simulating a nuclear spin reacting to a linear adiabatic passage. Variation of the amplitude and frequency ramping rate are both demonstrated independently.

Figure 4.15 shows simulation results using the linear/trapezoidal and hyperbolic secant pulse types. Similar to the data shown in 4.13, the linear/trapezoidal pulse (figure 4.15(a)) efficiently inverts large spin bandwidths, but performs poorly for FM deviations below $500\,\text{kHz}$ (see section C.2 for supplementary details). The features within the adiabatic regime are due to the nutations observed in 4.14. In contrast, the hyperbolic secant operates best with narrow bandwidths, and requires very high power to invert large bandwidths. There is no substructure within the hyperbolic secant's adiabatic regime.
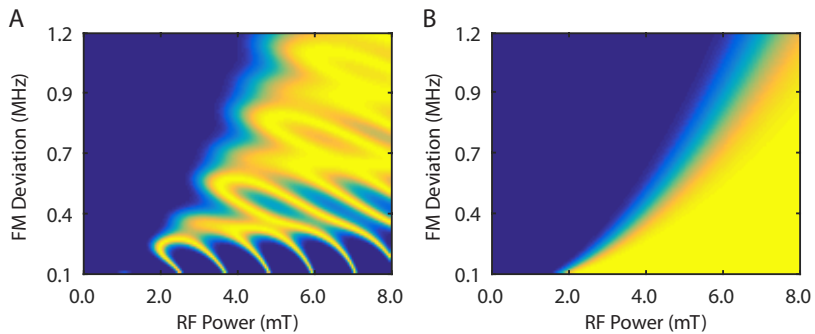
FIGURE 4.15: Simulations of adiabaticity for (a) trapezoidal and (b) hyperbolic secant inversion profiles. The plotted values range from 0 (blue) to 1 (yellow), where 1 is a perfect adiabatic inversion, and 0.5 corresponds an adiabatic half passage. Each data point corresponds to a simulation of inverting a spin from the up-state (+0.5) to down (-0.5). The inversion is performed in 0.1 ms, corresponding to a cantilever frequency of 5 kHz. The adiabaticity is calculated by determining the amplitude of the inversion, where 1 corresponds to a complete inversion from +0.5 to -0.5. This inversion efficiency is then raised to the power of 100, to obtain the adiabaticity for a $\tau_m = 10$ ms spin lifetime.

Chapter 5

Multiplexing

This chapter is published in:

Although $\sim$10 nm spatial resolution has been reached in several experiments [17, 73, 76], realizing this resolution in three-dimensional images required long averaging times. For instance, imaging the proton density (^{1}H) in a single tobacco mosaic virus required two weeks of data acquisition [73], even for coarsely sampled data. The long averaging times are prohibitive if one intends to refine voxel sizes or to image multiple nuclear spin species (e.g. ^{1}H and ^{13}C). The slow data acquisition is in part due

to the point-by-point measurement procedure where only a small subset of nuclei in a sample is detected at a given time.

An interesting avenue for speeding up the image acquisition process is to measure multiple signals in parallel and to use post processing to calculate the contributions from each individual signal. Signal encoding is especially well-suited for MRI since nuclear spins can be separately addressed by radio-frequency (RF) pulses based on their differing Larmor frequencies. In micron-to-millimeter scale MRI, Fourier-transform [77] and Hadamard [78, 79] encoding provide efficient means for detecting the thermal (Boltzmann) polarization of nuclear spins.

When imaging voxels are less than $\sim (100\,\mathrm{nm})^3$ the thermal polarization becomes exceedingly small and is dominated by statistical polarization fluctuations [65]. It is the variance of these statistical fluctuations that then serves as the imaging signal [16]. Since variance measurements cannot be coherently averaged, traditional encoding techniques fail and parallel signal detection is considerably more challenging.

One effort for parallel detection of statistical spin polarization included the use of multiple detector frequencies [80]. Unfortunately this approach is limited by detector bandwidth, and often only a single short-lived spin signal (which is the case for most biological samples) can be accommodated. An exciting prospect is to Fourier encode statistically polarized nuclei by a correlation measurement [76, 81], however these methods require pulsed gradients or mechanical shuttling and have yet to be applied to 3D imaging.

In order to accelerate MRFM data acquisition, we have developed a phase encoding technique. Unlike frequency multiplexing, the bandwidth of the spin signal is not limited by the number of parallel channels, and pulsed

gradients are not required. The phase encoding technique was demonstrated by detecting multiple isotopes (^{1}H and ^{19}F) simultaneously (chemical contrast). Additionally, 6 signals of ^{1}H were simultaneously measured to demonstrate the potential to speed up acquisition. With 6 simultaneous measurements, the time required to image the TMV experiment would be reduced from 2 weeks to 2 days.

5.1 Theory

In this section, the theory of phase multiplexing will be introduced as well as several technical achievements that were required for the measurement to work. These technical achievements include a four-quadrant lock-in amplifier, and sequential low-pass filters, both implemented using a Labview FPGA. Additionally a heuristic method was developed to optimize phase encoding matrices, and prevent amplification of detector noise.

5.1.1 Phase multiplexing

Phase multiplexing is achieved by exciting several nuclear spin ensembles sequentially, with a defined time delay between magnetization reversals. Since signal detection is phase-sensitive, a time delay τ corresponds to a phase shift $\phi = 2\pi\tau/T$, where $T = 1/f_c$ is the duration of one clock cycle and f_c is the detector frequency. When measuring N statistically independent spin ensembles, the total (complex) signal E is

$$E = \sum_{j=1}^{N} S_j e^{i2\phi_j} \; , \tag{5.1}$$

where $S_j = \sigma^2_{M_j}$ is the variance of the j'th ensemble's magnetization $M_j(t)$ and ϕ_j denotes the phase shift of the periodic reversal of $M_j(t)$ relative to the detector clock [82]. In order to separate the different signal components, one may carry out N measurements, each with a different combination of phases, yielding $\vec{E} = (E_1, E_2, ..., E_N)$. The reconstruction of the original spin signals $\vec{S} = (S_1, S_2, ..., S_N)$ then follows by linear recombination as

$$\vec{S} = \mathbf{A}^{-1}\vec{E} \ , \tag{5.2}$$

where the transfer matrix

$$\mathbf{A} = \begin{bmatrix} e^{i2\phi_{11}} & e^{i2\phi_{12}} & ... & e^{i2\phi_{1N}} \\ e^{i2\phi_{21}} & e^{i2\phi_{22}} & ... & e^{i2\phi_{2N}} \\ \vdots & \vdots & \ddots & \vdots \\ e^{i2\phi_{N1}} & e^{i2\phi_{N2}} & ... & e^{i2\phi_{NN}} \end{bmatrix}$$

contains the phase of each spin inversion during the cantilever period, as depicted in Figure 5.1d. The phase at which the spin signal due to the j'th ensemble (columns of $\mathbf{A}$) appears changes between different experiments k (rows of $\mathbf{A}$). Although any linearly independent set of phases ϕ_{jk} will allow for the reconstruction of $\vec{S}$, only a suitable choice of ϕ_{jk} will evade amplification of detector noise [82].

Since each measurement E_k simultaneously detects the magnetization of all nuclear ensembles, the signal collected after a complete sequence $\vec{E}$ is N times larger compared to a sequential collection of $S_1, ..., S_N$ without multiplexing. By contrast, the same amount of detector noise is added to each measurement E_k regardless of whether multiplexing is applied. Phase multiplexing can therefore improve the SNR by $\sqrt{N}$ for a fixed acquisition time. Alternatively, the acquisition time can be reduced by N without any loss in SNR.
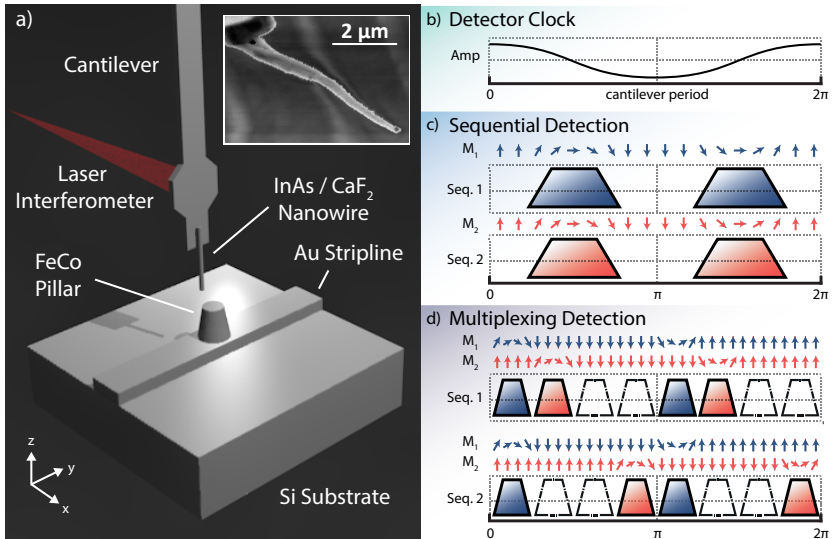
FIGURE 5.1: Basic principle of phase multiplexing with $N = 2$ nuclear spin ensembles. (a) Schematic representation of the MRFM apparatus showing a micromechanical cantilever and ferromagnetic tip. Inset: Scanning electron micrograph of an InAs nanowire test sample attached to the cantilever end. The nanowire is possibly terminated by a Au catalyst particle. (b) Cantilever detector clock. Each spin ensemble must be inverted twice per cantilever period T to apply a force on the cantilever. (c) For sequential measurements, only a single nuclear spin ensemble is flipped in each sequence. Arrows depict the orientation of nuclear magnetization $M_j(t)$ and trapezoids represent adiabatic RF pulses. (d) For phase multiplexed measurements, both nuclear spin ensembles are flipped, but the flipping is partially out of phase. Two different flipping sequences are applied to generate two different measurements E_1 and E_2, which are subsequently reconstructed to yield S_1 and S_2. Encoding phases in this example are $\phi_{11} = 22.5°$, $\phi_{12} = 67.5°$ (for E_1) and $\phi_{21} = 22.5°$, $\phi_{22} = 157.5°$ (for E_2).

Whether the improvement by N is realized depends on the choice of phases ϕ_{jk}. Poorly selected phases will amplify detector noise when reconstructing $\vec{S}$ from $\vec{E}$. We find that for white detector noise (such as thermal noise), the noise amplification factor is given by the matrix 2-norm: $||\mathbf{A}^{-1}||_2 = (\sum_{jk} |\tilde{a}_{jk}|^2)^{1/2} \geq 1$, where $\tilde{a}_{jk}$ are the matrix elements of $\mathbf{A}^{-1}$ [82]. For an optimum set of phases $||\mathbf{A}^{-1}||_2 = 1$. Although such an optimum set can be constructed (e.g., using the digital Fourier transform matrix $\phi_{jk} = \pi jk/N$), we used a heuristic search in order to satisfy additional constraints. In particular, the pulses were sequentially arranged to prevent the total RF power from varying over a cantilever period. Other potential noise sources include spin noise [16], correlations between spin ensembles, and instabilities in detector phase, gain or frequency [82].

5.1.2 Phase matrix optimization

Transfer matrices $\mathbf{A}$ were chosen such that the element-wise 2-norm of the inverse matrix was $||\mathbf{A}^{-1}||_2 \gtrsim 1$. These matrices minimize the propagation of thermal noise, which is the dominant noise in our measurements. To form the matrix, we first divided the cantilever half-period into p equally spaced phase slots (*i.e.*, for $p = 6$ slots, $\phi_{jk} \in \{0°, 30°, 60°, ..., 150°\}$). We additionally required all pulses to have a unique phase within each sequence E in order to evenly distribute RF power over the cantilever period, thus minimizing peak power and spurious mechanical excitation. This constraint precludes the use of digital Fourier transform matrices, which would otherwise be the obvious choice.

In the case of multiplexing with $N = 2$ signals as in Figure 5.1d, we used $p = 4$ phase slots with matrix

$$\mathbf{A} = \begin{bmatrix} 1 & e^{i\pi/2} \\ 1 & e^{i3\pi/2} \end{bmatrix} \, ,$$

which has a 2-norm of $||\mathbf{A}^{-1}||_2 = 1$.

In the case of multiplexing $N = 6$ signals, we performed a heuristic search to find an optimal matrix. The matrix used for Figure 3 had $p = 9$ with phases

$$\mathbf{A} = \begin{bmatrix} 1 & e^{i2\pi/3} & e^{i14\pi/9} & e^{i4\pi/3} & e^{i2\pi/9} & e^{i16\pi/9} \\ 1 & e^{i4\pi/3} & e^{i8\pi/9} & e^{i16\pi/9} & e^{i10\pi/9} & e^{i14\pi/9} \\ 1 & e^{i16\pi/9} & e^{i2\pi/9} & e^{i4\pi/3} & e^{i14\pi/9} & e^{i2\pi/3} \\ 1 & e^{i10\pi/9} & e^{i8\pi/9} & e^{i2\pi/3} & e^{i2\pi/9} & e^{i4\pi/9} \\ 1 & e^{i16\pi/9} & e^{i2\pi/9} & e^{i2\pi/3} & e^{i4\pi/9} & e^{i14\pi/9} \\ 1 & e^{i2\pi/3} & e^{i14\pi/9} & e^{i4\pi/9} & e^{i10\pi/9} & e^{i8\pi/9} \end{bmatrix} \, .$$

This matrix has $||\mathbf{A}^{-1}||_2 = 1.09$. This means that the SNR improvement is reduced from $N = 6$ to $N/||\mathbf{A}^{-1}||_2 = 5.5$.

5.1.3 Adiabatic inversions

Nuclear magnetization reversals were performed using periodic application of adiabatic RF pulses. An individual adiabatic pulse consisted of frequency and amplitude modulation. A pulse had a center frequency f_{center} and bandwidth of $2\Delta f_{dev}$, and thus inverted nuclear spins only in a thin "resonance slice" (RS) in space (see Figure 5.2a) whose Larmor frequencies lay within $f_{center} \pm \Delta f_{dev}$.

Two types of frequency modulations were used: linear and hyperbolic secant. For linear sweeps, the RF frequency was linearly increased from $f_{\text{center}} - \Delta f_{\text{dev}}$ to $f_{\text{center}} + \Delta f_{\text{dev}}$ over the duration of the pulse T_{p}, which was equal to $T/(2p)$, where p was the number of phase slots. The amplitude was modulated with a trapezoidal shape to ensure phase continuity at the beginning and end of each pulse. Linear sweeps were used for the measurements shown in Figure 5.2.

Consecutive pulses were allowed to have overlapping tails such that the pulse was effectively longer than T_{p}, further aiding adiabaticity. Sech/tanh sweeps (with $\beta = 15$) were used for the measurements shown in Figure 5.3.

The maximum RF amplitude that could be employed in our apparatus was limited by undesired electrostatic driving (of the cantilever) that set in above $7\,\text{mT}$, corresponding to a $300\,\text{kHz}$ Rabi frequency for ^1H nuclei. This allowed for about $p \sim 10$ phase slots before the adiabatic condition became violated.

5.2 Results

We demonstrated phase multiplexing by measuring the statistical polarization of $\sim 10^5$ ^1H and ^{19}F spins on an InAs nanowire test sample. The nanowire had a diameter of $120\,\text{nm}$, and was coated with $60\,\text{nm}$ of CaF_2 by thermal evaporation (see Figure 5.2a). ^1H spins were present in a $\sim 1\,\text{nm}$ layer of surface adsorbates that naturally formed in ambient air [17, 20, 73]. For nanoscale MRI measurements, the nanowire was attached to the end of an ultrasensitive silicon cantilever and mounted in an MRFM apparatus operating at $4.2\,\text{K}$ temperature and $2.77\,\text{T}$ magnetic bias field. Under measurement conditions, the cantilever had a resonant frequency $f_c \sim 5\,\text{kHz}$, a spring constant of $k_c \sim 2.5 \times 10^{-4}\,\text{N/m}$, and a mechanical

$Q \sim 30,000$, equivalent to a thermal force noise of about $3\,\mathrm{aN}/\sqrt{\mathrm{Hz}}$. For the imaging, the nanowire was approached to within $100\,\mathrm{nm}$ of a 300-nm-diameter FeCo magnetic tip [39].

5.2.1 Chemical contrasting

In a first experiment we performed multiplexing of two different nuclear isotopes (^{1}H and ^{19}F). In order to identify the nuclear species, we parked the nanowire $\sim 60\,\mathrm{nm}$ above the nanomagnetic tip and measured the nuclear magnetization as a function of RF center frequency (Figure 5.2b). Two peaks at 111 MHz and 118 MHz confirmed the presence of both ^{1}H and ^{19}F nuclear species. To demonstrate multiplexing, we performed a one-dimensional spatial scan over the magnetic tip while exciting both ^{1}H and ^{19}F. At each location, $N = 2$ signals were acquired with different phase sequences, resulting in the two scans E_1 and E_2 shown in Figure 5.2c-d. Application of Eq. (5.2) then directly reproduced the reconstructed signals (Figure 5.2e-f). We found excellent agreement between reconstructed signals and sequential control measurements of ^{1}H and ^{19}F .

5.2.2 Multiple spatial signals

In addition to chemical contrast imaging, multiplexing can also be applied to detect signals of the same isotope in different spatial regions of a sample. Such multi-slice imaging provides depth information with a single lateral scan, and may be useful to improve the fidelity of 3D image reconstruction. Figure 5.3a shows an example of spatial multiplexing by detecting $N = 6$ resonant slices of ^{1}H. A shifting peak is seen as the nanowire moves across the different slices, and the six signal traces clearly reflect the geometry of imaging slice and nanowire.
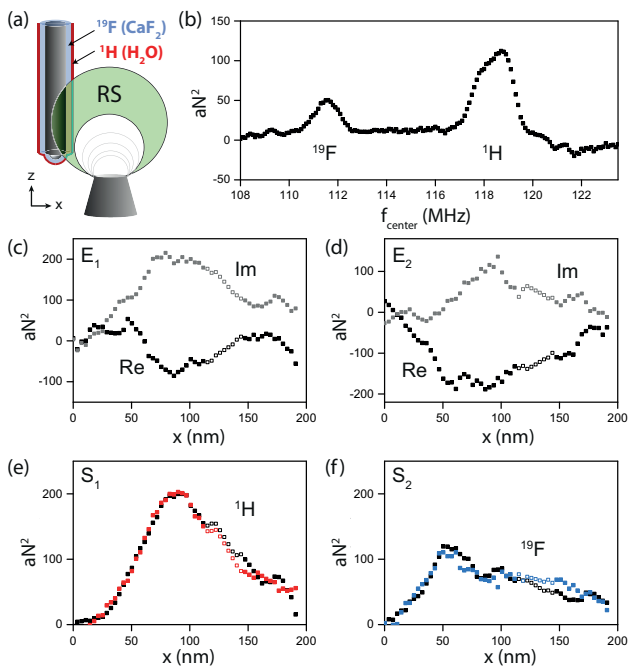
FIGURE 5.2: (a) Schematic of the nanowire with ^{19}F and ^1H layers. RS represents the resonant slice, *i.e.* the volume in space where nuclear spins contribute to the signal. (b) NMR spectrum of the sample measured by incrementing the RF center frequency f_{center} while the nanowire was at a fixed position. In a magnetic field of 2.77 T, the Larmor frequency of ^1H is 118.0 MHz and of ^{19}F is 110.9 MHz. Each data point was averaged for 360 s. (c,d) One-dimensional x scans (3.6 nm steps) at a fixed height using the multiplexing sequences of Figure 5.1d. Gray and black symbols represent the real and imaginary parts of E_1 and E_2, respectively. RF center frequencies were 118.0 MHz and 110.9 MHz with $\Delta f_{dev} = 0.5$ MHz. (e,f) Reconstructed signal (colored squares) providing separate images for (e) ^1H and (f) ^{19}F. A sequential single isotope scan is shown for comparison (black squares). Total averaging time per point was 240 s for multiplexed acquisition and 480 s for sequential acquisition. For reasons explained in [82], the mechanical detector was unstable between 115 nm and 145 nm. Data in this range was replaced by interpolated data, represented by hollow symbols in (c-f). Data has been spatially low pass filtered by 5 points.
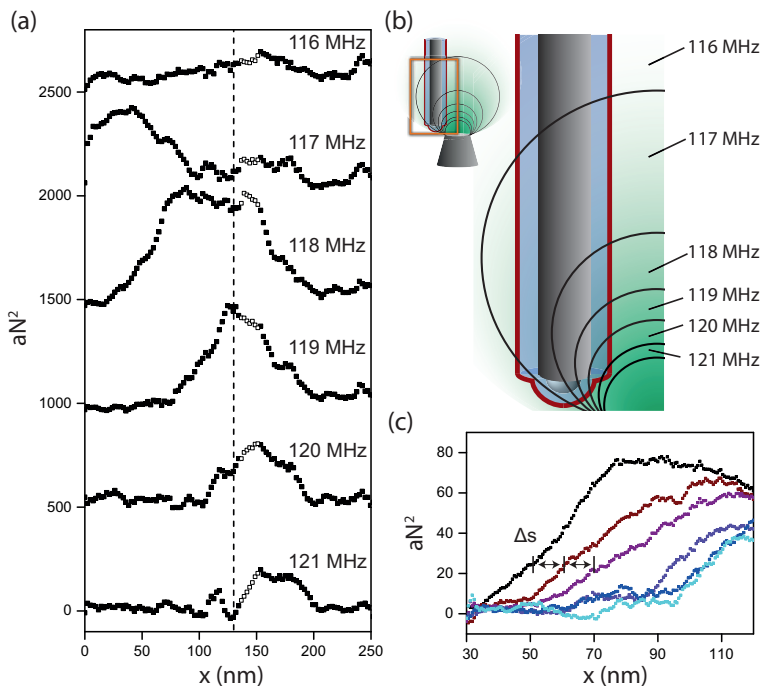
FIGURE 5.3: (a) Signal from $N = 6$ different ^{1}H ensembles measured during a single x scan with phase multiplexing. x increment was 2.4 nm, $\Delta f_{\text{dev}} = 0.3$ MHz, and center frequencies of resonant slices ranged from 116 to 121 MHz as indicated. The averaging time was 360 s at each position for all 6 measurements together. As in Figure 5.2, hollow points represent data that was interpolated due to instability of the mechanical oscillator [82]. Data was low pass filtered by 5 points. (b) Schematic of the spatial shape of resonant slices associated with Larmor frequencies $116 - 121$ MHz. As the nanowire is scanned from left to right, spins intersect slices with progressively higher Larmor frequencies, reflected in a shifting peak in (a). The schematic corresponds to the x location of the vertical dotted line. (c) High resolution x scan with increments of 0.6 nm, $\Delta f_{\text{dev}} = 0.13$ MHz, and slice center frequencies ranging from 117.8 to 119.8 MHz in steps of 0.4 MHz (from left to right). Averaging time was 1080 s at each position for all 6 measurements together. Data was low pass filtered by 30 points.

We have tested multiplexing down to very low values of Δf_{dev} to estimate the limits towards high spatial resolution. Figure 5.3c shows such a high resolution scan acquired with frequency increments of $\Delta f_{\text{center}} = 0.4\,\text{MHz}$. By comparing the signal onset as a function of x position, we find that the lateral distance between slices Δs is about $10\,\text{nm}$. This corresponds to a lateral magnetic gradient of

$$G = \frac{\partial B_z}{\partial x} = \frac{\Delta f_{\text{center}}}{\gamma_n \Delta s} \approx 1 \times 10^6\ \text{T/m} \ .$$

A comparison with similar nanomagnetic tips, where $G \sim 4 - 5 \times 10^6\,\text{T/m}$ [83], indicates that our tip had a lower-than-expected gradient, probably due to partial oxidation. Note that the imaging resolution is not limited by the step size Δs, but by the bandwidth of the frequency modulation $\Delta f_{\text{dev}} = 0.13\,\text{MHz}$. As the full width at half maximum of the resonant slice is approximately $\sqrt{2}\Delta f_{\text{dev}}$ [73], the imaging resolution is about $\sqrt{2}\Delta f_{\text{dev}}/(\gamma_n G) \approx 4.3\,\text{nm}$. With an improved nanomagnetic tip, an imaging resolution of $\sim 1\,\text{nm}$ can therefore be expected.

5.3 Noise Analysis

To compare the quality of multiplexed data to that of sequential measurements, we have quantified the signal error by analyzing the standard deviation of point-to-point fluctuations in the data sets. For the multiplexed scans in Figure 5.2e-f we find $\epsilon_H = 6.62\,\text{aN}^2$ and $\epsilon_F = 6.53\,\text{aN}^2$, while the separate measurements have $\epsilon_H = 6.89\,\text{aN}^2$ and $\epsilon_F = 4.94\,\text{aN}^2$. The differences in amplitude between multiplexed and separately measured signals have standard deviations of $6.31\,\text{aN}^2$ for ^1H and $8.34\,\text{aN}^2$ for ^{19}F
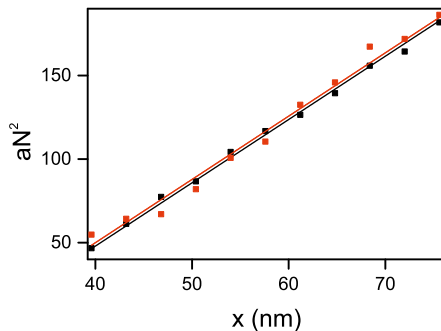
FIGURE 5.4: Two traces of ^{1}H signals measured sequentially with multiplexing (red) and single sweep (black). The data is a subset previously shown in Figure 5.2e. The two datasets were fit with linear equations, and an average slope was obtained. The lines displayed are from each dataset being refit, but using the average slope obtained from the first fit. The x-offset of the two equations indicates an experimentally measured positional accuracy of 0.6 nm.

[82]. These results confirm that phase multiplexing produces the same signal amplitude and SNR as sequential acquisition within half the averaging time.

While imaging step sizes and resolution for our experiments were on the order of a few nanometers, we found that the imaging precision was below one nanometer. For example, in the leftmost trace of Figure 5.3c (117.8 MHz center frequency), we observed that the signal rose with $3.4 \, \text{aN}^2/\text{nm}$ around $x \sim 65$ nm. Comparing this slope with the measurement error $\epsilon_H = 0.8 \, \text{aN}^2$ we derive a position uncertainty of 0.24 nm. Although this precision is probably overestimated, we note that the signal onsets of the two scans in Figure 5.2e (and reproduced in Figure 5.4) coincide within 0.6 nm. Such good positional accuracy is an important prerequisite for extending nanoMRI to subnanometer resolution.

5.4   Outlook

Finally, we briefly comment on the limits of phase-multiplexed detection. When applying N RF frequencies simultaneously, both average and peak power increase by at least N regardless of the finer details of RF pulses. Phase multiplexing therefore puts progressive demands on RF excitation, which in our experiments limited $N < 10$. Moreover, error analysis shows that strong signals tend to transmit noise to weak signals and eventually deteriorate the SNR of the latter [82], which we found to become noticeable as $N > 6$.

In summary, we have introduced a simple phase multiplexing method for accelerated detection of nanoscale NMR signals. The method is applicable even if spin ensembles are randomly polarized. It can in principle be used with any phase-sensitive excitation/detection scheme, including those used in recent diamond-based magnetometry experiments [18, 84]. Using an MRFM apparatus, we have demonstrated simultaneous acquisition of nuclear spin signals from two different nuclear species and from up to six different sections within a sample. One-dimensional imaging scans reached a nominal spatial resolution $< 5\,\mathrm{nm}$ with subnanometer positional accuracy. The reduction in measurement time offered by our technique will be especially useful for 3D images of biomolecular complexes with isotope contrast.

Chapter 6

Influenza virus

This chapter presents the Influenza virus, and preliminary MRFM results of an attempt to image a single copy of the virus.

6.1 Introduction

Viruses are complex molecular assemblies that are responsible for a vast array of diseases in humans, animals, and plants. Despite their intimate connection to ailments, three-dimensional imaging of viruses remains a formidable task. A significant hurdle is the large variability in structures, causing methods that rely on averaging ensembles to fail [85]. No method in the unbridged regime is capable of imaging a single copy of a large biosystem, obtaining high resolution, and resolving chemical contrast.

An example of such a biosystem is the constantly mutating influenza virus (see figure 6.1a for 3D rendering), which causes severe illness in 3-5 million people, and between 250,000 and 500,000 deaths every year [86]. A particularly deadly strain is the Influenza A virus H1N1, or more commonly referred to as the Avian Flu. In 1918, this virus caused the worst pandemic in history, killing 50 million people worldwide [87]. Despite this staggering death toll, the virus is not airborne, which would certainly have increased its infection rate. However, recent work has demonstrated that H5N1 is within a few mutations from becoming airborne, raising concern of another pandemic or bioterrorism [88]. Although medical practice has significantly improved since 1918, this is only a partial safeguard. As the population density continues to rise, accelerated infection of deadly viruses becomes evermore prevalent, making vaccine development essential [89].

A strain of influenza virus is characterized by two integral membrane proteins: hemagglutinin and neuraminidase. Neuraminidase is essential for replication as it allows the virus to release from a host cell [92]. Hemagglutinin is responsible for viruses binding to cells with sialic acid-containing receptors in their membrane, which are commonly found in the upper respiratory tract or erythrocytes [93]. The structure of hemagglutinin is shown in figure 6.1b. Mutations in the genome cause slight variations in the hemagglutinin structure, and consequently change a virus' binding properties [94].

Influenza vaccines use neutralizing antibodies that target hemagglutinin, and prevent the virus from interacting with target receptors. Consequently, the exact binding site of the antibody is critical to the effectiveness of a vaccine. Recent work indicates that most vaccine antibodies attach far from the hemagglutinin binding site, suggesting a lot of room to improve vaccine effectiveness [95, 96]. Here we investigate the potential for nanoMRI to provide high resolution 3D images of an individual H3N2 virion.
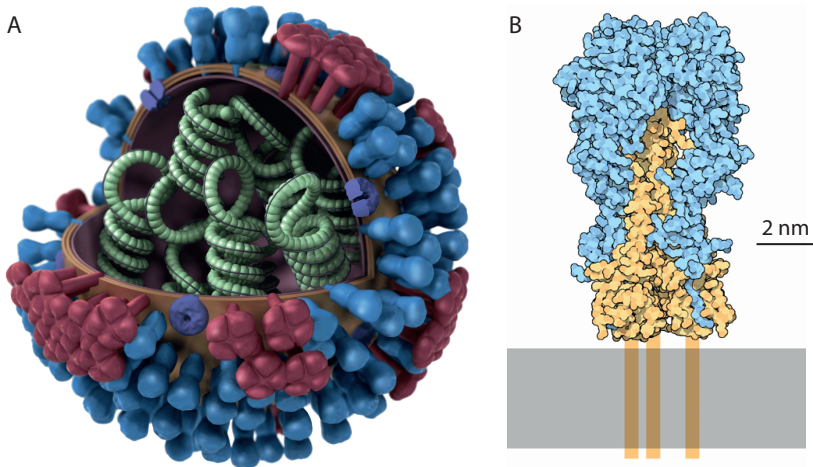
FIGURE 6.1: (a) 3D model of an influenza virus. The structure consists of a outer lipid membrane and a protein shell underneath. The virus encapsulates several strands of RNA wrapped around protein cores that range from $30 - 120$ nm [90]. The lipid surface contains three exposed transmembrane proteins: hemagglutinin, neuraminidase, and the M2 proton channel. Image from Centers for Disease Control and Prevention website. (b) Schematic of a hemagglutinin protein attached to a lipid membrane. The structure of this transmembrane protein was determined with x-ray crystallography. Image from the Protein Database [91].

6.2 MRFM of influenza virus

Here we describe an attempt to image a single influenza virus, which is ongoing during the writing of this thesis. We have explored two techniques for placing a virus at the end of a cantilever: solution deposition and using a fabricated nanowire. We show frequency- and touch-map images of a nanowire containing viruses. The images were obtained by scanning the nanowire over a silicon cone. Upon confirming the correct geometry of the virus, we switched the silicon cone surface out for a stripline with a dysprosium magnet. Preliminary results suggest that the field gradient of

this magnet is comparable to the best gradients reported literature values [38].

6.3 Virus preparation

Two methods of attaching the influenza virus to the end of cantilevers were explored in this work. One method used very narrow pipettes to deposit virus solution onto a flat cantilever surface. The second method used fibbed nanowires that could be placed in virus solution, and then fixed to the cantilever after processing.

6.3.1 Cantilever deposition

In a first attempt, influenza viruses were deposited onto cantilevers using micropipettes [22]. The end of a cantilever was cut using a focused ion beam to produce a flat surface to accommodate several viruses. A 5 nm titanium adhesion layer and a 10 nm gold layer were thermally evaporated onto the cantilever tip, while the cantilever shaft was shielded by a blade [43]. The cantilever was then placed under a UV-ozone lamp to oxidize the gold surface, which creates a hydrophilic environment. A Narishige's PC-10 puller was used to fabricate a micropipette with an end diameter of approximately $10\,\mu$m. Solution containing purified viruses was sucked into the micropipette, and positioned close to the cantilever using a Narishige micromanipulator stage. An optical microscope using long working range objectives was used to observe the pipette and cantilever. The cantilever was brought into contact with the solution up to the paddle for approximately 10 minutes to allow viruses to diffuse onto the surface. The pippette was retracted, and the cantilever dried in air within seconds. Figure 6.2
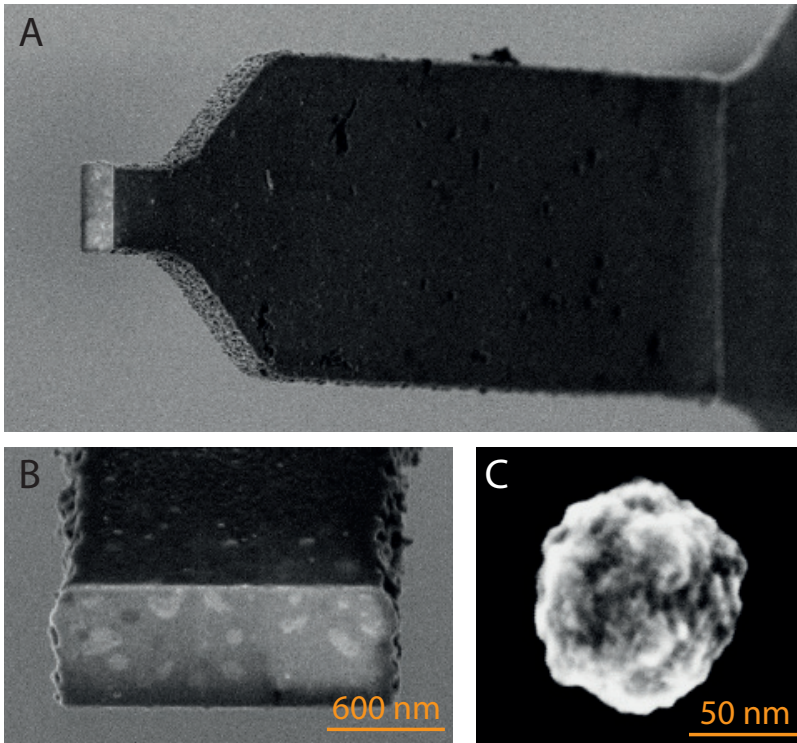
FIGURE 6.2: (a) An SEM image showing viruses on a cantilever from deposition with a micropippette. (b) Zoom-in of the viruses deposited on the cantilever end. The viruses all have different shapes and sizes due to deformation from surface tension while drying. (c) A zoomed-in image of a single influenza virus on a silicon substrate deposited by a micropipette. These images were taken by Hiroki Takahashi.

shows images of a mass loaded cantilever after the virus attachment process.

This deposition method had limited success since the solution quickly evaporates. This drying harms the viruses in two possible ways: (i) by applying

a large surface tension, and (ii) by creating a dry environment in which the lipid membrane is unstable. Although influenza is much more resilient to evaporation than most viruses, the survival rate is only about 50% [97]. Since, the cantilever can only accommodate a few viruses in its small tip cross sectional area, a 50% survival rate yields many cantilevers with no viruses after drying. Consequently, screening several cantilevers with an SEM does not provide good indication that an unscreened cantilever contains viruses. In contrast, the TMV virus is nearly unaffected when it is removed from its native environment, and therefore the yield per cantilever was much higher in previous MRFM work [22].

6.3.2   Fibbed nanorods

A more refined approach involves first depositing influenza viruses on nanorods, and then attaching the nanorods to cantilevers. Nanorods were cut out of a silicon chip using a focused ion beam (FIB) [98]. Starting with a silicon chip, the edge was shaved down to create a 500 nm thick suspended membrane. The sample was rotated by 90°, and nanorods were cut out of the membrane. One or two bridges contact the side of the nanorod to keep it connected with the silicon chip. Figure 6.3a shows an SEM image after the nanorods were fibbed. Gold was evaporated onto the nanorods, and placed in a UV-ozone chamber to modify the gold surface. The final product under an optical microscope is shown in 6.3c.

Freeze drying is a safe method of removing a virus from an aqueous environment. Water can be sublimated by freezing the virus, and then lowering the pressure to about 10^{-2} mbar. However, the freezing must be done rapidly in order to prevent ice crystals from forming. These crystals swell the virus causing it to rupture. In contrast, rapidly cooling the virus prevents ice crystals from forming by passing the gel transition temperature

before ice crystals have time to form. In order to drop the temperature fast enough, the sample is plunged into ethylene glycol or liquid nitrogen, which is too violent for a cantilever to survive.

Unlike cantilevers, nanorods can survive freeze drying. Additionally, a chemical fixation process that strengthens the membrane can be applied to viruses (see section A.3 for the procedure) [99], which is not possible with the micropippette deposition method. The silicon chip containing nanrods was placed into a solution, allowing the viruses to absorb onto the surface. Figure 6.3b shows an SEM image of the end of a nanorod, with three viruses fixed to the tip.

The nanorods are attached to the end of a cantilever using a micromanipulator and optical microscope. A drop of UV-curing glue was placed on the end of a cantilever using a micropipette. The cantilever was then brought into contact with the nanorod, as shown in figure 6.3d. The glue was hardened using a UV laser pointer. The cantilever sometimes applies a sufficient force to break the bridge between the nanorod and the silicon chip. Otherwise, a micropipette was used to apply a force and break the bridge after the glue hardened.

6.4   Characterization in MRFM

Figure 6.4a shows a touch-map of a nanorod using a cone surface at room temperature. The image shows four round features with heights of approximately 75 nm and lateral diameters of approximately 100 nm. These features are comparable to the SEM images shown in 6.3b and agree with influenza virus dimensions reported in literature.
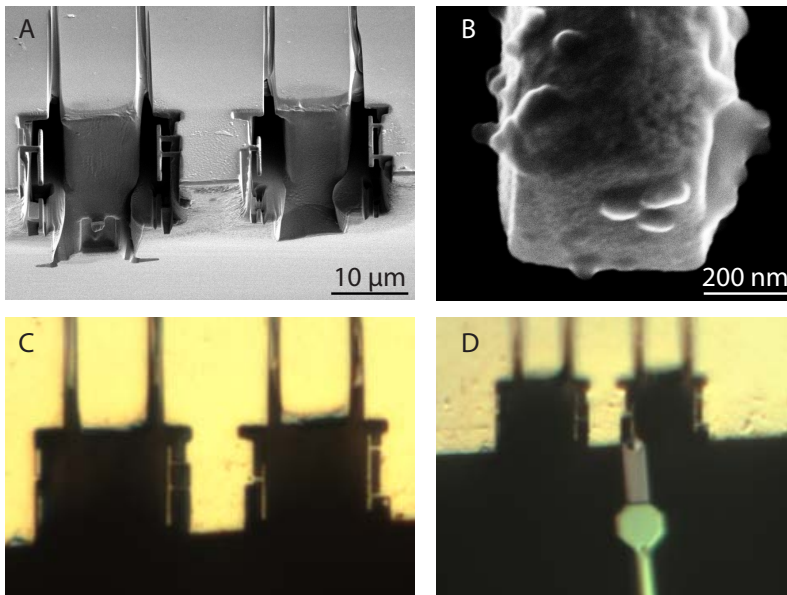
FIGURE 6.3: (a) An SEM image of nanorods formed using a focused ion beam from the edge of a silicon chip. (b) High resolution SEM image of a nanorod end. Three Influenza viruses are clustered together on the right hand side. The sidewalls are rough due to redeposition during the FIB cutting. (c) Optical image of the nanorods from panel (a). (d) An optical image showing the attachment of a nanorod to a cantilever. The glue is dried using a UV laser pointer, and the nanorod is broken off by pressing down with a micropippette. These images were taken by Hiroki Takahashi.

Figure 6.4b shows a second harmonic frequency map of the same nanorod surface as figure 6.4a. This image shows a similar arrangement of features as the touch-map, but with less lateral resolution. The edges of the nanorod are also barely visible. The touch-map required 7 hours to acquire, whereas the frequency map only needed 40 minutes. This agreement between the touch-map and frequency map is useful when lining up a nanomagnet and virus for MRFM data acquisition.
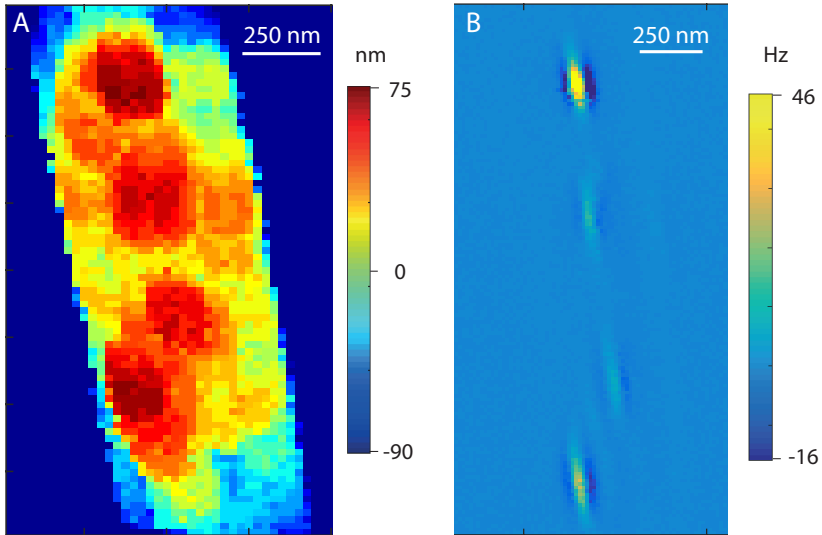
FIGURE 6.4: (a) Touch-map image of the end of a nanorod with influenza viruses. The four tallest features are approximately 75 nm high, measured relative to the nanorod surface. The touch-map was recorded using a cone substrate. (b) A second harmonic frequency-map that show four features in a similar pattern as the touch-map. The locations of the features are more precise emphasized since the tip-sample convolution is insignificant. However, height information cannot be extracted from this data, only the separation of the four features in XY.

6.4.1   Initial MRFM results

Figure 6.5a shows a one dimensional x-scan over the magnet centered at 425 nm. The two peaks correspond to ^{1}H signal on either side of the magnet. The full width at half maximum of the peaks are approximately 75 nm, suggesting that the signal originates from an influenza virus.

The cantilever was placed as close to the edge of the magnet as possible. Figure 6.5b shows a sweep of the RF frequency at this location. The

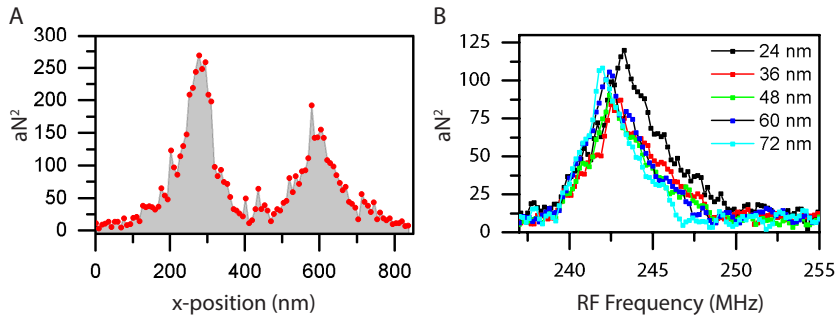FIGURE 6.5: (a) X-position scan over the magnet while measuring ^{1}H nuclear spins. Each point was measured for 3 minutes. The two lobes are approximately 100 nm, which corresponds well with the diameter of influenza viruses. (b) Tip-field measured by positioning the cantilever over the magnetic tip at different heights indicated in the legend. The RF frequency was swept to record ^{1}H nuclear spins. Each data point was measured for 6 minutes, and the data was smoothed by 5 points to improve visibility.

^{1}H center frequency is at 239 MHz, and the tip-field extends to peak by 10 MHz. This tip-field corresponds well with the best reported magnetic field gradient [38].

6.4.2 Simulation of influenza virus

Here we present a simulation of the expected nanoMRI results of an influenza virus. We assume a magnetic field gradient comparable to the one demonstrated in the previous section, and we assume that we have sufficiently high SNR to detect a resonance slice with a width of 0.3 MHz.

Figure 6.6a shows a toy model of an influenza virus, with regularly spaced membrane proteins on the top and bottom surface. The light blue streak across the bottom corresponds to a thin water layer that is always present in MRFM images. Here we demonstrate the imaging capabilities of two
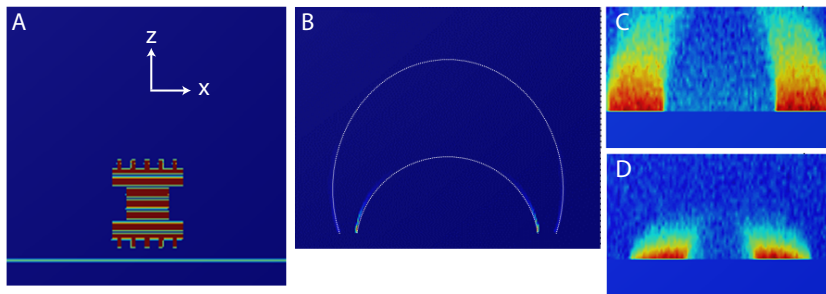
FIGURE 6.6: (a) Toy model of an influenza virus in the ZX-plane. One pixel corresponds to $4 \times 4\,\text{nm}^2$, and the full image is $400 \times 200\,\text{nm}^2$. (b) Two resonance slices corresponding to a low ($85\,\text{mT}$) and high ($285\,\text{mT}$) magnetic tip field. The convolution of these resonance slices with the toy model are shown in (c) and (d) respectively.

different resonance slices: one with a high tip field, and the other with a low tip field. Figure 6.6b shows the two resonance slices in space. The convolution of these two resonance slices with the toy model are shown in figure 6.6c and d.

The convolved data was deconvolved using the known tip field and geometry. Figure 6.7a shows the deconvolution of the low tip field slice, and 6.7b shows the high tip field. The low tip field slice images the full depth of the virus with low spatial resolution. In contrast, the high tip field slice provides a high resolution image of the transmembrane proteins, but only penetrates through about a third of the sample. These simulations suggest that multiplexing with several resonance slices of varying tip fields would provide complimentary information in resolving complex structures.

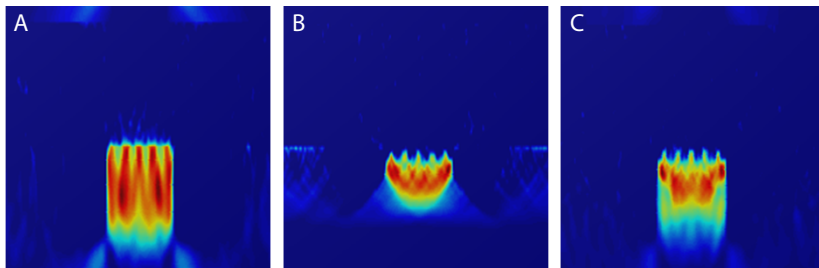FIGURE 6.7: Deconvolved data of the (a) low tip field data, and (b) high tip field. (c) The global reconstruction of both datasets.

6.5 Outlook

One of the most challenging aspects of biological imaging with MRFM is the ability to reliably place samples at the end of cantilevers. This requires an extensive understanding of the cantilever surface chemistry, as well as the biological sample. Additionally, preserving biological structures upon drying and placing into a low temperature and high vacuum environment is difficult.

In this work, viruses were attached by careful adjustment of the virus concentration, and providing an adequate time for the viruses to absorb to the surface. The gold was UV irradiated to create a hydrophillic environment, and the virus was treated with a fixation protocol to preserve the membrane upon drying.

One potential scheme is to improve the attachment selectivity for gold surfaces. A lot of work has demonstrated that viruses can be genetically engineered to add sulfur-containing amino acids into recombinantly produced viruses, which preferentially bond to gold surfaces and nanoparticles [100, 101]. Figure 6.8 shows a GaAs nanowire with a 30 nm diameter gold catalyst at one end from the growth process. These small nanowires
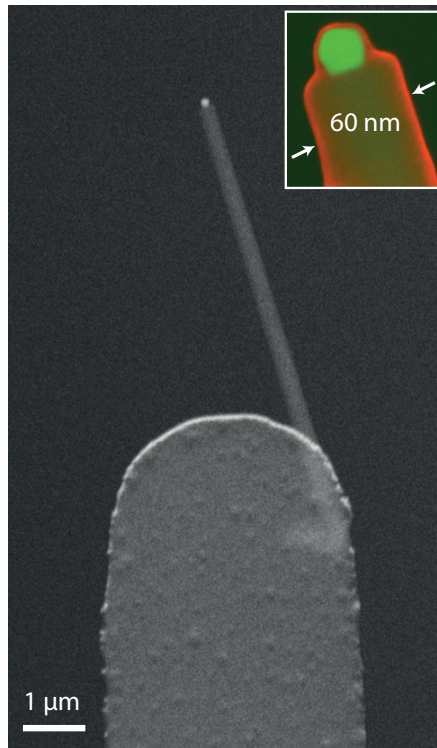
FIGURE 6.8: SEM image of a GaAs nanowire with a gold catalyst fixed to the end. The nanowire is 60 nm in diameter.

provide very low non-contact friction, and the gold nanoparticles provide a small binding area allowing only a few viruses to physioabsorb.

Chapter 7

Conclusions and outlook

In this thesis, we have worked towards improving the capabilities of MRFM to resolve structures within the unbridged imaging regime. We seek to atomically resolve structures with the proposed scheme in section 1.4. To this end, we have developed a novel MRFM probe with high stability and low mechanical noise. With this new design we have demonstrated a new state of the art imaging resolution of $\sim$4 nm, and sub-nanometer positional accuracy $\sim$0.3 nm. We have also worked on improving the efficiency of adiabatic inversions, which provide a means of detecting thinner resonance slices, and consequently improving spatial resolution.

We have also developed a multiplexing method capable of measuring at least six nuclear spin noise signals simultaneously. This provides a means of detecting signals from several isotopes or multiple resonance slices without increasing the data acquisition time frame. This effectively solves one of the required strategies of the proposed roadmap.

Several sample preparation advancements were achieved, including using nanowire cantilever extensions to reduce the non-contact friction between magnetic tips and sample. We also fabricated nanowire structures that provide a convenient means of attaching biological samples to cantilevers.

Appendix A

Protocols and procedures

A.1   Spin signal search process

The following is a standard procedure we used when searching for a spin signal:

1. Turn on the magnetic field (example 5 T) to saturate (or nearly saturate) the magnetic tip. Record a frequency map around the magnetic tip, at a constant height within at least 50 nm from the surface.

2. Measure a touchmap around the location of the tip identified in the frequency map. The position of the tip according to the touchmap may be slightly shifted compared to the frequency map. The touchmap provides a better indication of the exact location. Determine an average z-height of the magnetic tip from the touchmap.

3. Position the cantilever on the edge of the magnetic tip in the x-axis, and in the middle of the y-axis. The height should be approximately 60 to 100 nm above the average z-height measured in (2).

4. Apply feedback damping so that the cantilever quality factor is approximately 200 to 300.

5. Perform an MRFM sweep as a function of RF power. Use two out-of-phase trapezoid adiabatic pulses such that the total output power is constant. Set the center frequency of one pulse to 1 MHz above the ^{1}H Larmor frequency according to the magnetic field. For example, for 5 T, the center Larmor frequency is ∼214 MHz, therefore set the pulse center frequency to ∼215 MHz. Set the center frequency of the second pulse ∼5 MHz below the first frequency (for example ∼210 MHz) such that the two pulses do not interfere. Use a large FM deviation, between 0.7 and 1 MHz. The MRFM signal should increase as a function of RF power, decrease a little, then increase again. The first peak corresponds to the optimized RF power, whereas the second peak corresponds to electrostatic driving.

6. Perform an x-scan using an RF frequency slightly higher than the external field Larmor frequency (∼215 MHz). Scan over the middle of the magnet, along the x-axis. Measure a spin signal at each position, averaging for about 5 mins per point. Find the position that gives the largest signal.

7. Using the determined RF power and the position with a maximum signal from the previous two steps, measure an MRFM signal as a function of RF frequency. Measure above and below the external field Larmor frequency (∼214 MHz) by about 20 MHz. The tip field should appear at higher frequencies.

8. Increase the external field such that the Larmor frequencies increase by a few MHz. Measure the same RF sweep as the previous step for a few external field values, and ensure that the MRFM signal shifts with external field. The same position can be re-found for each external field using a frequency map.

A.2 RF startup procedure

All of the parameters depend on one another. For example, the RF power changes the frequency of the cantilever due to electrostatic driving. This can also change the phase of the damping feedback. The following is a procedure that mitigates the depedencies on all the variables. It is intended to optimize all of the variables that depend on each other: cantilever frequency, RF frequency, feedback phase.

1. Sweep self oscillation phase, find phase that requires the least self oscillation drive output

2. Measure a short (1 second) thermal spectrum to determine the resonance frequency. Turn on the RF at this frequency.

3. Self oscillate and determine if the cantilever frequency has changed. If so, change the RF to the new frequency. Loop until the cantilever and RF frequencies match within a tolerance (for example 2 Hz). This step accounts for thermal drift, and only continues when the drift stops.

4. Turn on damping with a low feedback gain. Perform ringdown curves vs. cantilever external drive amplitude. Find the amplitude required for a desired amplitude (ex. 3V detection).

5. Perform ringdown curves while increasing damping feedback until a mid level Q factor is met (for example 1000)

6. Measure ringdown Q factor vs. feedback phase. The minimum Q factor corresponds to the optimally set phase. Deviating away from this phase increases the Q factor in a quadratic profile.

7. Increase damping, check that ringdown frequency and RF frequency match (if not update it).

8. Measure approximately 20 ringdowns to verify Q factor is at set value and ringdown frequency matches cantilever frequency.

This procedure can be completed within 30 seconds when optimized.

A.3 Influenza virus fixation

Influenza A virus solution (40% sucrose, 0.02% BSA, 20 mM pH 7.4 HEPES buffer, 100 mM NaCl, 2 mM MgCl2): $1 - 5 \cdot 10^5$ virus particles/μL

1. Dipped nano-rods in a 4x diluted virus solution: 1 hour

2. Moved to an aldehyde solution (3% formaldehyde, 3% glutaraldehyde, 20 mM HEPES buffer): 1 hour

3. Add osmium tetroxide (final concentration: 0.7%): 1 hour

4. Wash with water

5. Dipped in 30% MeOH, then freeze-dried

Appendix B

FPGA documentation

B.1   Introduction

In this work, two Labview FPGA units (National Instruments PCI-e-7852R) were used to implement several continuous loops. One unit was dedicated to detecting the nuclear spin noise contribution to the cantilever amplitude. The second FPGA unit contained several independent processes such as the laser temperature control PID, a self oscillation feedback loop, and damping feedback loop.

Parallel processing is one of the most powerful aspects of FPGA computing. In the Labview FPGA, each parallel process is performed in a separate while loop. Figure B.1 shows the general structure of an independent loop. The first frame calculates the clock rate of the loop, the second performs a calculation, and the last frame can add delays to run the loop slower.
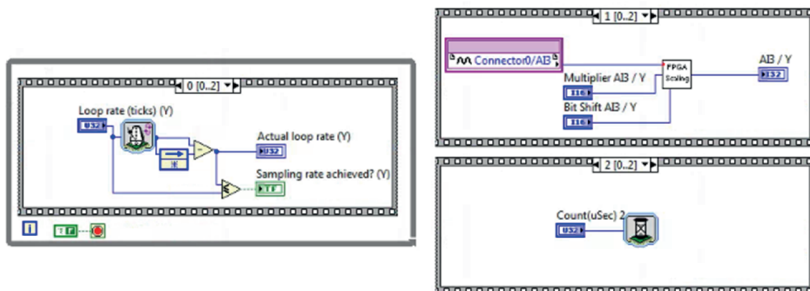
FIGURE B.1: (a) A standard wiring diagram of a stand alone loop on the FPGA. The *'actual loop rate'* outputs the number of clock cycles required to complete all of the frames within the while loop. The *'Loop rate (ticks)'* can be set to limit the speed of the loop. (b) In the second frame, an operation is performed. In this case, a voltage is read in from connector *AI3*, and a bit shift scaling is performed on it. (c) The loop can be slowed down by adding more clock cycles with the *'Count'* variable, similar to the *'Loop rate'* field.

B.1.1 References to target FPGA

In general, communication between Labview and the FPGA units was limited to as few VIs as possible. However, one issue that arose was that these VIs are called many times, and each created a reference to the FPGA upon being called. These references are only cleared from memory once the top level program is stopped or is completed. Consequently, continuously producing new references slows down the computer by filling up memory, and eventually causes Labview to produce a fatal error. Note that all of the presented work was completed with Labview 2009 Service Pack 1. This FPGA reference issue may have been resolved in newer Labview versions, however I have not seen it mentioned in any of National Instrument's technical notes.

To avoid producing too many reference variables, only the top level program is designated to create one. This architecture is depicted in B.2a.
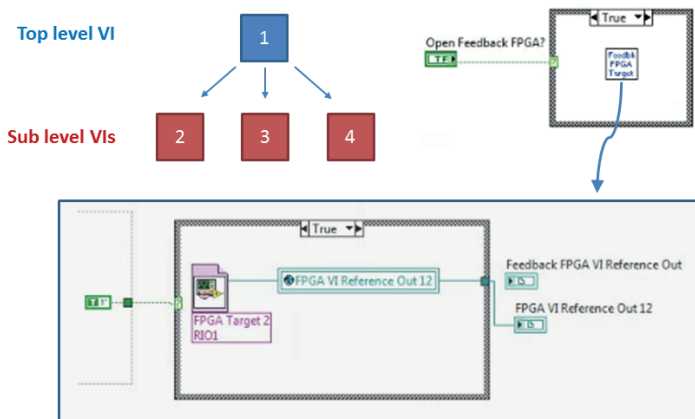
FIGURE B.2: FPGA referencing

Each VI that requires a host reference contains the components shown in figure B.2b. The top level program has *'Open Feedback FPGA?'* manually activated in the front panel, causing it to call B.2c and initialize a reference in the global variable. All sublevel VIs that require the reference are called with *'Open Feedback FPGA?'* deactivated by the top level VI. The sublevel VIs can then use the global reference to communicate with the FPGA. Note that if the global reference is not initialized before attempting to access, often an error is displayed. However, if Labview is low on memory, then this causes a fatal Labview crash. Also note that each time a new target VI is compiled, the global reference acts like a new variable type, and must be recreated in the global file.

B.1.2   Bit shift division operation

Division is a time consuming FPGA operation, and typically requires several (~ 10) clock cycles to calculate. With several sequential division

operations, this can create large bottlenecks in data processing. One way to avoid this slow down is to use a single clock cycle bit shift operation for dividing. A division operation can be performed by calculating

$$A' = A \cdot M \cdot 2^b$$

where A is an input value, M is a multiplier, and b is a bit shift. For example, the operation $A' = A/10$ can be performed using $M = 26214$ and $b = -18$. Effectively A and M are multiplied together, and then 2^b truncates the value by shifting the decimal place to the correct order of magnitude. The values for M and b must be calculated with floating point arithmetic, and therefore must be performed off the FPGA. For example, to calculate M and b in the case of signed 16-bit operation ($p = 16$), and a scaling factor s

$$b = -\Big((2p - 1) - log_2(s2^p)\Big)$$

$$M = s \cdot 2^{-b}$$

In the case of an operation with unsigned variables, the $(2p-1)$ is replaced with $2p$.

The bit shift division operation can introduce several issues with precision and overflow. For example, if A and M are both 16-bit integer values, the variable after multiplication must have a precision of the sum of both input precisions (in this case, a 32-bit integer). In the case of dividing by a value greater than 1, then after multiplying by 2^b, the result can be converted to 16-bit precision.

This operation also introduces round off error due to the 2^n decimal truncation. This issue can be circumvented by scaling up A and M by a multiplier, performing the bit shift, and then scaling the result back down.

B.2 FPGA spin signal detection

The detection pathway described in section 4.2.2 was initially implemented with a Labview DAQ. The DAQ recorded 60 second intervals of lock-in amplifier X and Y channels, which was filtered, and the variances were calculated. However, each time trace processed by Labview required a few seconds of computational overhead that could not be used to acquire new data. More importantly, digital filters require a build-up time before reliable values are output. This typically requires discarding $\sim 3 \cdot T_c$, and therefore a substantial amount of data is discarded for long time constants like 3 seconds.

In order to circumvent these issues with the DAQ, we developed a continuous acquisition tool with a Labview FPGA. A Labview based FPGA is used to calculate the spin signal intensity. This provides a means of offloading the sample filtering main purpose of this is to offload

B.2.1 Digital low-pass filter

Figure B.3 shows a regular Labview implementation of a first order digital low pass filter. For an input function $f(t)$ sampled at a rate of $1/T_s$, the function can be discretely represented by $f[t]$. The discrete function can be low-pass filtered using consecutive input values $x[n] = f[t_n]$ and the previous data point $y[n-1] = f[t_{n-1}]$. These two values are multiplied by weighting factors that collectively determine the filter cutoff frequency

$$w_y = e^{-2\pi f_c T_s} \tag{B.1}$$
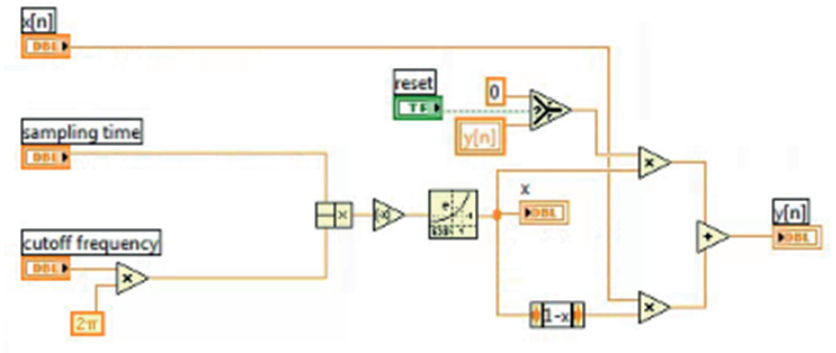
$$w_x = 1 - w_y \tag{B.2}$$

FIGURE B.3: Labview VI implementation of a reprogrammable low-pass filter. The filtered value $y[n]$ is calculated using the previous filtered value $y[n-1]$ and the current input value $x[n]$. Weighting factors w_y and w_x are calculated with equations B.1 and B.2 respectively.

such that the filtered data point is given by

$$y[n] = w_x \cdot x[n] + w_y \cdot y[n-1] \ .$$

The Labview FPGA has a built in low-pass filter function, however it has several limitations. For example, the filtering characteristics are hard-coded when compiled. Additionally, a single filter requires a lot of FPGA memory, which did not allow for enough filters for the spin signal data pathway described in section 4.2.2. In order to circumvent this issue, we implemented a reprogrammable filter. Figure B.4 shows an FPGA implementation of a reprogrammable low-pass filter. The filter weights w_x and w_y are bit shift operators that can be adjusted be uploaded after compilation.
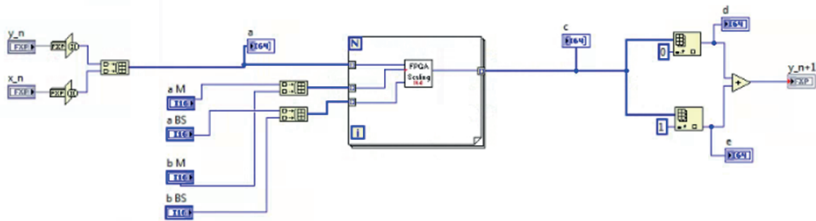
FIGURE B.4: The FPGA implementation of a reprogrammable low-pass filter used within the signal pathway. The filter weights w_x and w_y are calculated with a Labview VI, and uploaded to the filter.

B.2.2 Spin signal filter bank

The spin signal detection pathway described in section 4.2.2 was implemented in this work a Labview FPGA. We initially programmed a two lock-in channel signal pathway, and increased this to four channels (section 4.2.3) to detect both the phase and amplitude of spin signals. Figure B.5 shows the front panel of the signal pathway implemented on the FPGA.

The filter weights (or coefficients) were uploaded to the FPGA through a FIFO and saved in memory variables. Each weight corresponds to a bit shift and multiplier, saved in variables 'a BS' and 'a M' for one weight, and the other in 'b BS' and 'b M'. The block diagram for this process is shown in figure B.6.

Each consecutive X_0 (0°) and X_{90} (90°) channel value were passed into an FPGA analog input. A phase shift was applied to these values to obtain the projection along (45°) and (135°), providing two more lock-in channels X_{45} and X_{135} respectively. Figure B.7 shows the block diagram loop that performs this rotation.

The main filter loop is shown in figure B.8, where each lock-in channel value was passed through a bank of 14 filters. The inner for loop runs
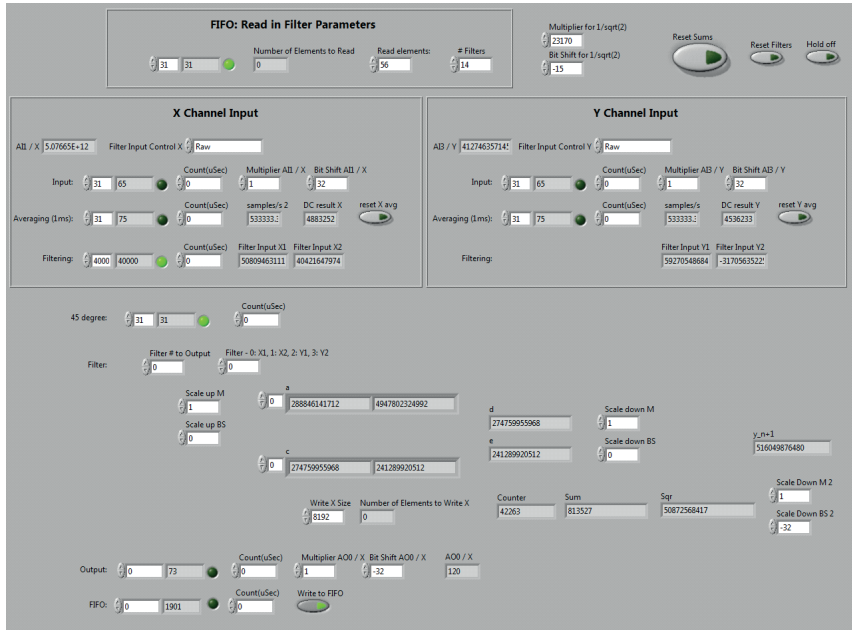
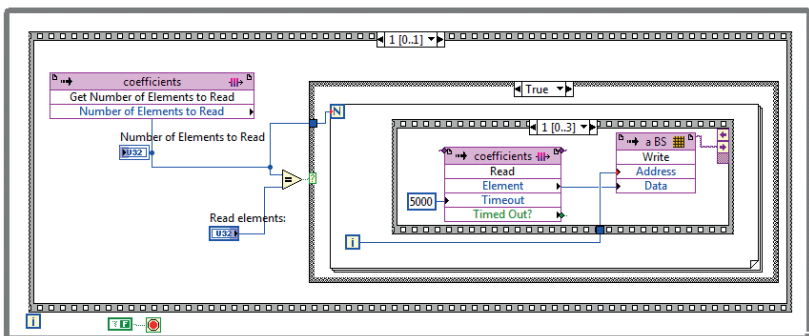FIGURE B.5: FPGA implementation of the spin signal pathway.

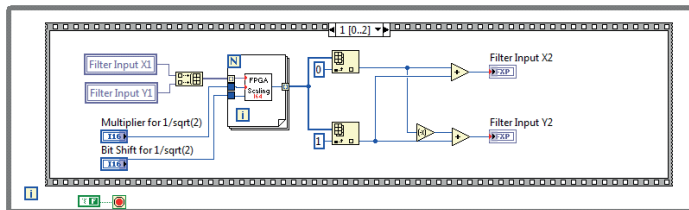FIGURE B.6: Upload of low-pass filter weights via FIFO.

FIGURE B.7: Signal rotation to obtain channels X_{45} and X_{135}.

through each of the four lock-in channels, and the outer loop cycles each of the filters. Each filtered value (for each channel) is saved in a memory variable '*y[n-1] i*', where *i* corresponds to the channel *X, X2, Y,* or *Y2*. The filtered value is also added to a cumulative sum and sum of squares of previous filtered values. These calculated values are saved to memory to access during the next cycle of data input. Each filtered value (or each channel) is passed from the FPGA target to the host VI in figure B.9.

B.3   Fringe control

In order to stabilize the diode laser wavelength against thermal drift (as described in 2.8.2), a PID controller adjusts the temperature of a peltier cooler that is attached to the diode. This adjustment is applied according to the DC value of the interferometer signal. The laser interferometer voltage is low-pass filtered by $3\,\mathrm{Hz}$ and amplified to a $0-5\,\mathrm{V}$ range using an SR560 filter to obtain a DC fringe value. This filtered voltage is passed into an FPGA, which is handled by figure B.11a. The feedback compensates for slow room temperature drifts, and therefore the RMS of the input voltage is measured over $100\,\mathrm{ms}$ intervals to decrease noise (figure B.11b).
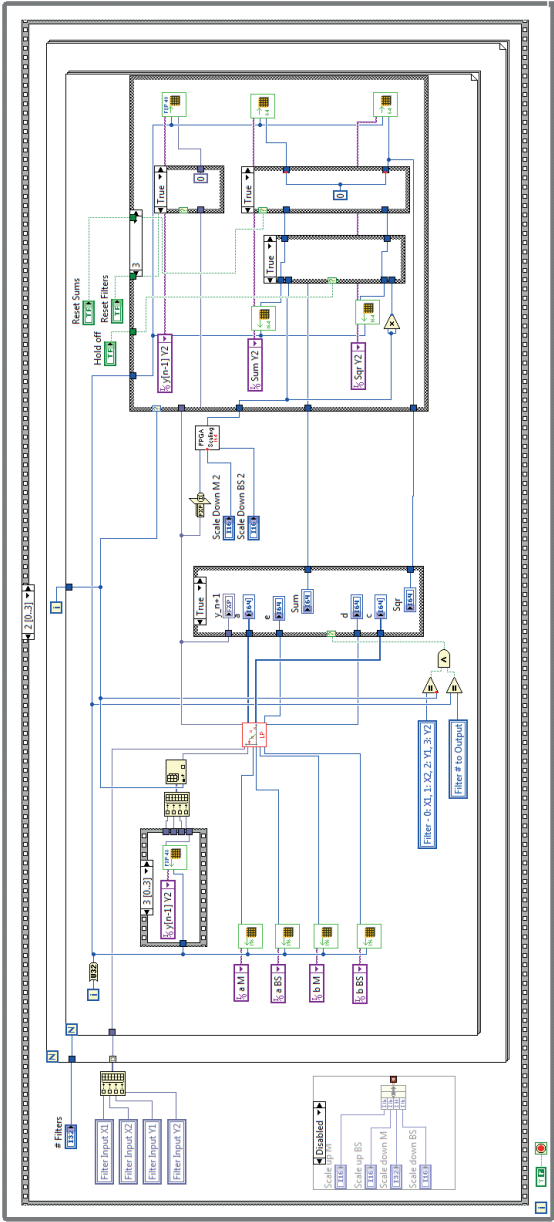
FIGURE B.8: Spin signal pathway filtering loop.
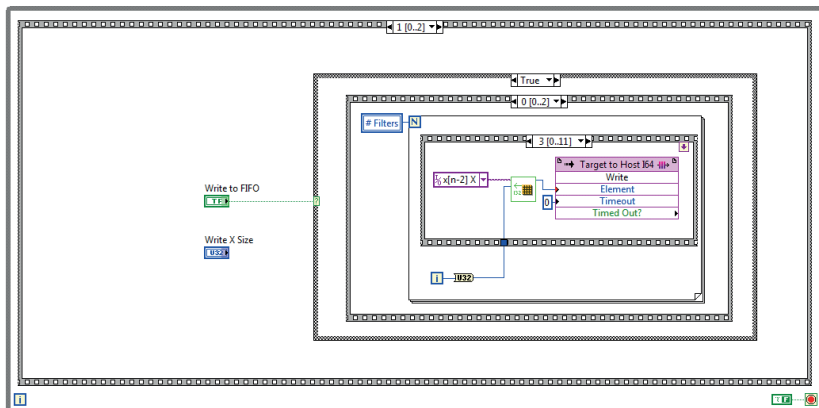
FIGURE B.9: Spin signal pathway filtered output

The PID controller was implemented with a built-in FPGA component shown in figure B.11c. The RMS fringe voltage (or *'Laser Temperature'*) is the PID input, and the setpoint is assigned using a calibration program. The PID is operated with low proportional and integral gains, typically ∼0.2 and ∼0.008 respectively. The integral gain is dependent on the PID loop rate, which must be run at ∼10 Hz by setting the loop rate to ∼4,000,000. Figure B.11 shows the front panel for these components of the FPGA.

The setpoint is assigned using the *'calibrate fringe'* button, found in the fringe monitor (shown in figure B.12. The fringe calibration VI is shown in figure B.13). Running this VI sweeps the control voltage to the TEC between ∼0.5and∼1.0 V. The DC interferometer value is measured for each control voltage, providing a display of the fringes. The top panel shows the DC voltage as measured by the DAQ, and the second panel shows the laser power measured by a photodiode and amplified. The bottom panel is a normalization of the top panel with the laser power. The
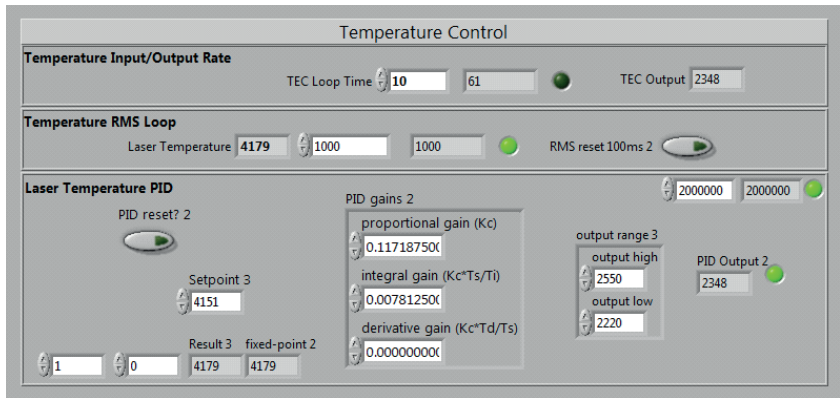
FIGURE B.10: Fringe locking FPGA front panel diagram. (a) The voltage input and output clock rate is measured and can be adjusted with *'TEC Loop Time'*. This loop is typically run as fast as possible. (b) Calculation of the fringe RMS. (c) The PID loop with the setpoint, PID gains, and output limits.

fringe is assigned by placing the cursors of the bottom plot near the maximum and minimum of a fringe, and selecting the *'Select Setpoint'* button. Pressing this button updates the global variables with the AC and DC filter gains, and calculates the calibration factor to convert the oscillation amplitude from volts to nm.

B.4 Cantilever feedback control

The MRFM cantilever is controlled by both a self oscillation and a damping feedback loop. Both of these feedback modes use the interferometry detection signal as a drive signal. However, the detection and drive signals are 90° out of phase, which must be compensated for with a phase shifer.
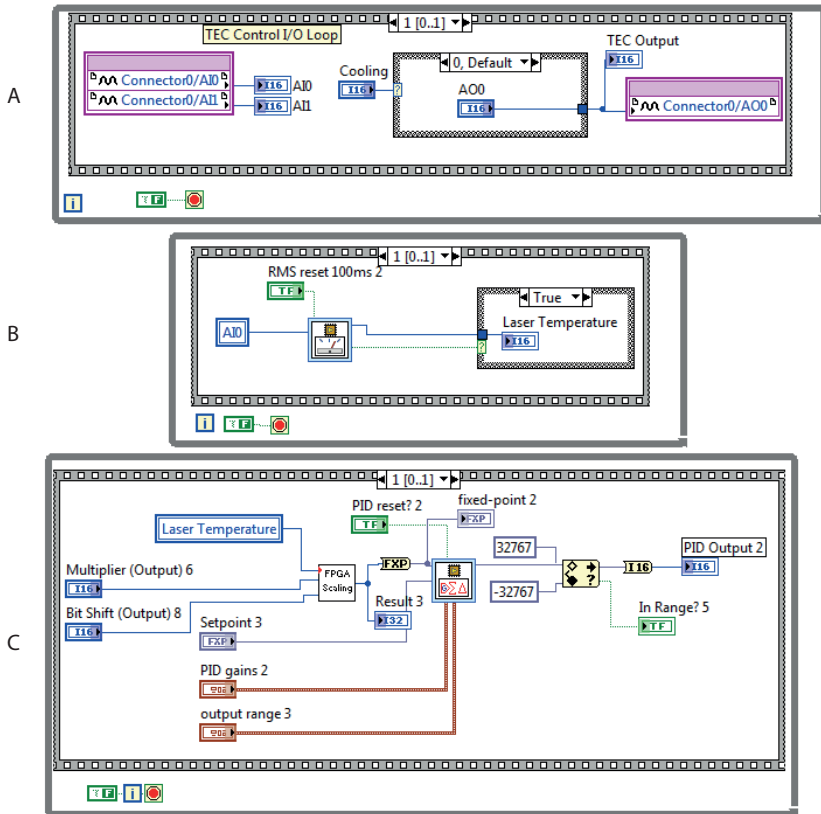
FIGURE B.11: Fringe FPGA PID feedback block diagram. (a) Fringe voltage input and controller output loop. (b) Loop that calculates the RMS of the fringe voltage input. (c) The PID loop that calculates the control voltage.

FIGURE B.12: Fringe monitor

B.4.1 Digital all-pass filter

A digital all-pass filter was described in section 3.4.4. This unilateral Z-transform can be written as a power series

$$X(z) = \sum_{n=0}^{\infty} x[k-n]z^{-n}$$

$$Y(z) = \sum_{n=0}^{\infty} y[k-n]z^{-n}$$

where n corresponds to discrete time steps back in time relative to current time step $x[k]$ and $y[k]$. The all-pass filter is a second order filter, and
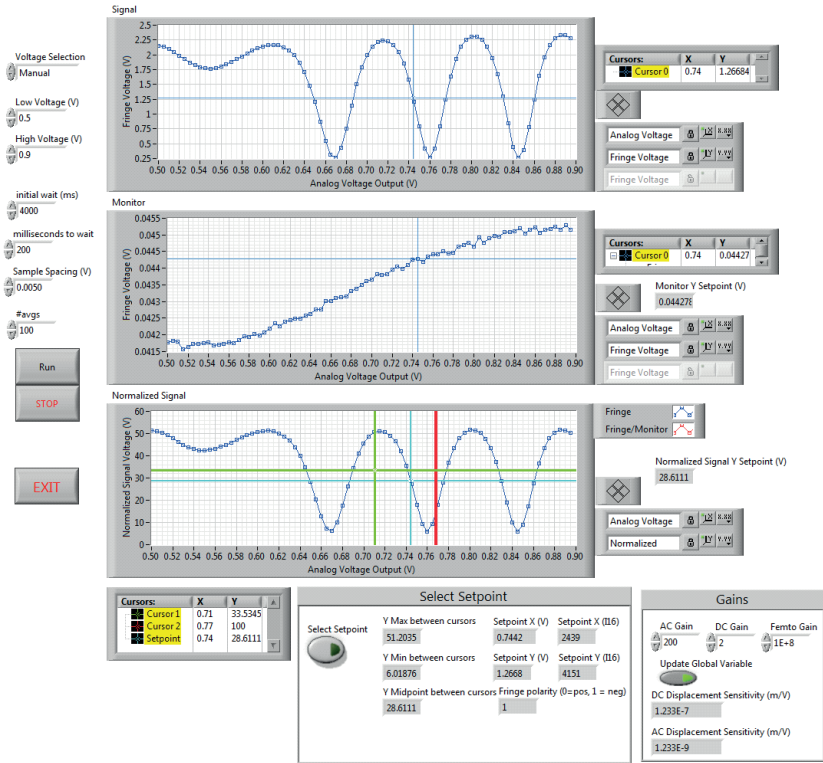
FIGURE B.13: Fringe setpoint calibration

therefore it can be described by powers of z up to $n = 2$

$$y[k] + y[k-1]z^{-1} + y[k-2]z^{-2} = H(z)\Big(x[k] + x[k-1]z^{-1} + x[k-2]z^{-2}\Big)$$

with the real coefficient transfer function

$$H(z) = \frac{z^{-2} - 2\Re(z_0)z^{-1} + |z_0|^2}{1 - 2\Re(z_0)z^{-1} + |z_0|^2 z^{-2}}$$
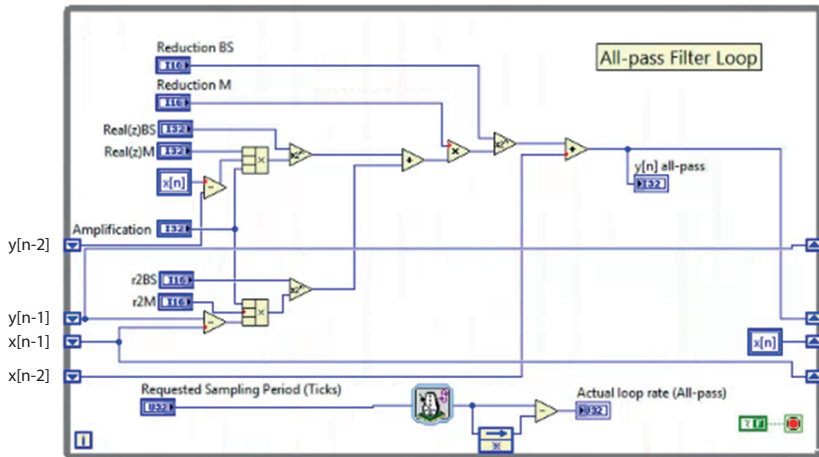
FIGURE B.14: FPGA implementation of an all-pass filter

this can be simplified to an equation in terms of the filtered value of x[k], which is dependent on the previous filtered values and inputs

$$y[k] = |z_0|^2 x[k] + 2\Re(z_0)\Big(y[k-1] - x[k-1]\Big) - |z_0|^2 y[k-2] + x[k-2]$$

Figure B.14 shows a Labview FPGA implementation of this equation.

B.4.2 Phase shift calibration for all-pass filter

The all-pass filter is calibrated each time the cantilever frequency changes, such as when the sample-magnet position is changed. For each calibration, equation 3.14 is calculated as a function of knee frequency ω_c (figure B.15a). The corresponding phase shift of each $|z_0|$ is calculated by $\tan\theta = \Im(H)/Re(H)$ as a function of the knee frequency (figure B.15b). The knee frequency that provides the desired phase shift θ is interpolated
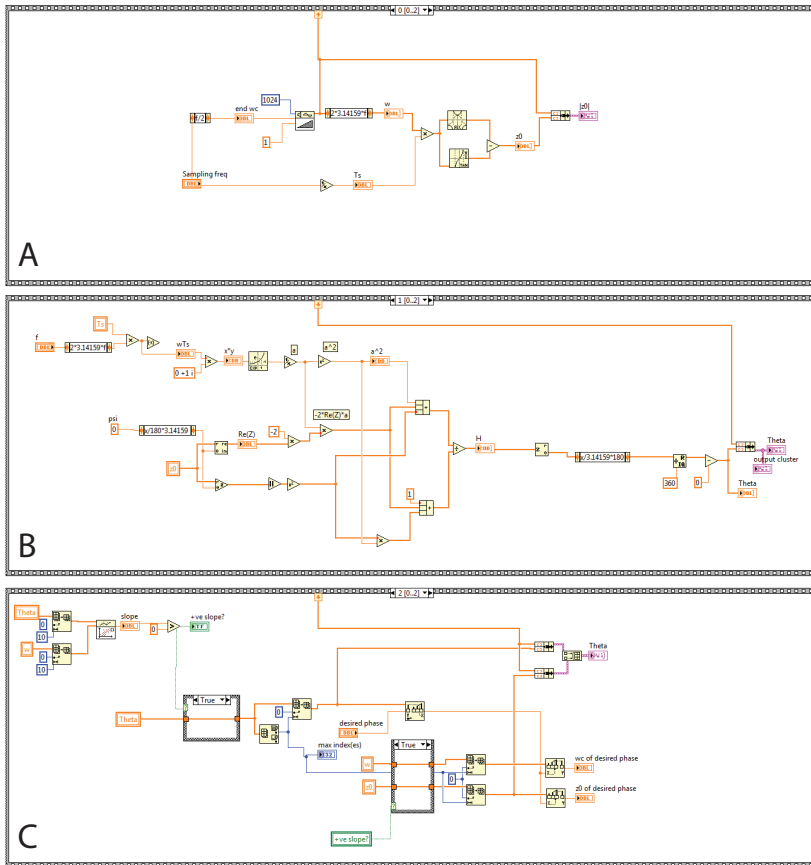
FIGURE B.15: FPGA all-pass calibration wiring diagram

from the curve and used to set the all-pass filter on the FPGA (figure B.15c). Figure B.16 shows a screenshot of the corresponding front panel diagram.
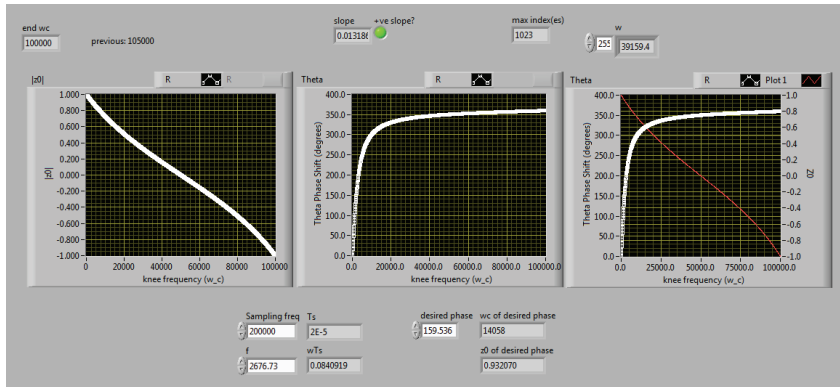
FIGURE B.16: The front panel diagram for the all-pass filter calibration. The cantilever frequency f is passed in as the only free parameter. The magnitude of the pole $|z_0|$ and phase shift angle θ as a function of the knee frequency ω_c are plotted. The right most plot shows $|z_0|$ and θ plotted up to the discontinuity that occurs in the θ vs. w_c plot.

B.4.3 Self-oscillation

The self oscillation feedback circuit uses the interferometer signal to drive up the cantilever motion. As the feedback loop drives the amplitude harder, the drive signal also becomes proportionally larger. In order to prevent the amplitude from being continuously driven up (and eventually out of control), a PID feedback is used to limit the driving amplitude. When the cantilever amplitude is below a setpoint value, the PID drives the cantilever harder. When the amplitude becomes higher than the setpoint, the PID compensates by outputting a smaller drive signal.

Figure B.17 shows a front panel diagram of the self oscillation loop that we implemented with a Labview FPGA. The interferometer signal is bandpass filtered around the cantilever frequency and amplified by a factor of ~200x. This voltage is input into an FPGA, and the RMS of the cantilever amplitude is calculated over a 100 ms (see top loop of figure B.18). This

oscillation RMS is passed into a PID that outputs a feedback voltage (*'PID Output'*) proportional to the relative difference between the input RMS and a setpoint RMS. The RMS feedback output is added to a optional constant offset, and multiplied by the phase shifted cantilever input signal (shown in the bottom loop of figure B.19) to produce a new drive signal. The result of this loop is then output with the loop shown in figure B.20.

B.4.4 Damping

We implemented an active damping feedback loop described in section 3.4.3 on a Labview FPGA. The role of the damping circuit is to counteract a cantilever excitation by applying an opposing drive signal with a magnitude proportional to the desired quality factor. This circuit is implemented using the phase shifted cantilever signal from the all-pass filter, applying an additional 180° phase (or inversion), and multiplying by a scaling factor before outputting to the cantilever drive. Figure B.21 shows the front panel diagram of the damping feedback loop. The wiring diagram is shown in figure B.22.

B.4.5 Self oscillation and damping calibration

Figure B.23 shows the Labview VI that uploads the scaling values to the FPGA. Self oscillation is acted with the *'Self osc'* button. The phase is set with the slider, and the corresponding values to produce that phase shift with the all-pass filter is uploaded to the FPGA. The self oscillation PID gains are set with the *proportional gain (Kc)'* and *integral gain'* fields. The upper plot outputs the RMS of the self oscilaltion PID as a function of time. The optimum self oscillation phase is determined by adjusting the
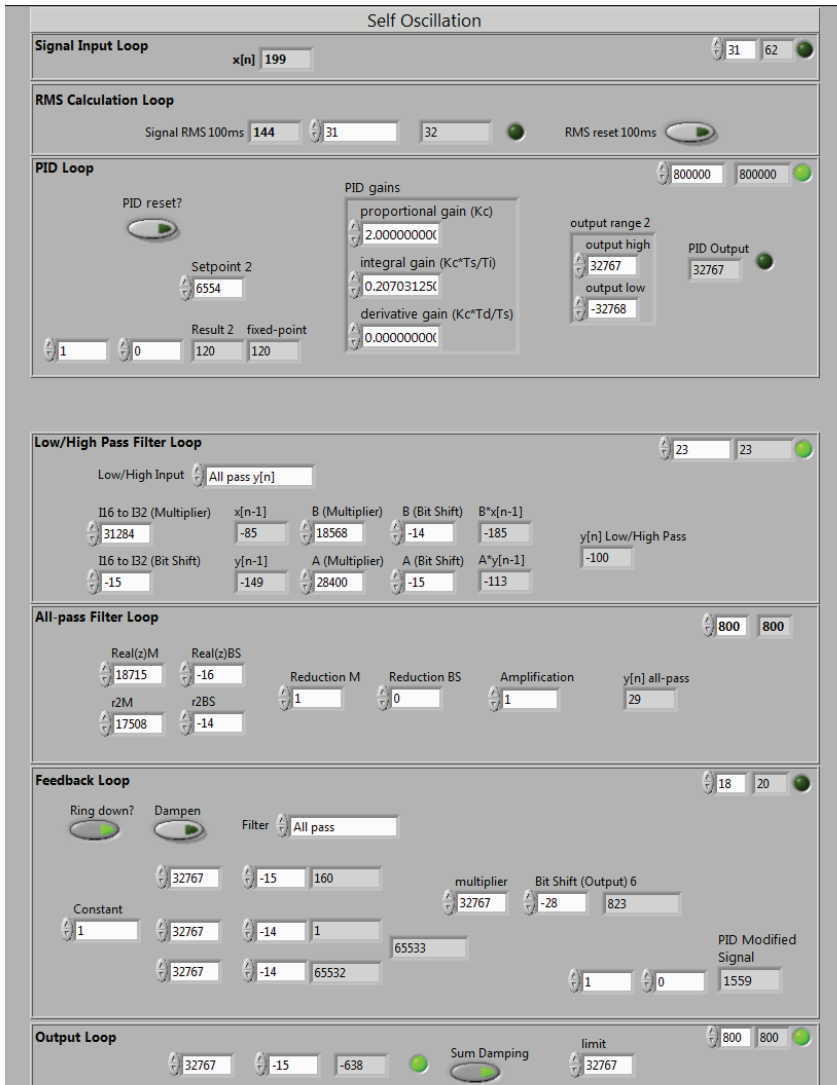
FIGURE B.17: Front panel diagram of the self oscillation loop.
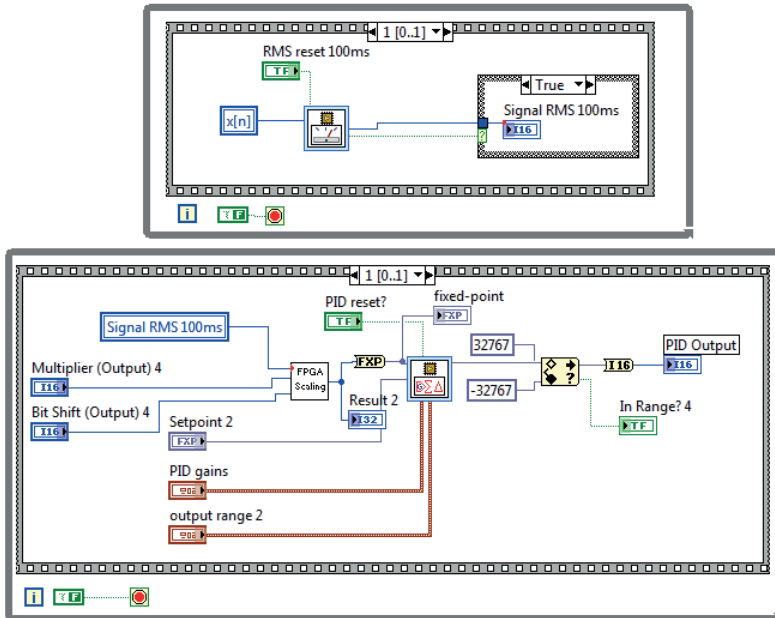
FIGURE B.18: Top loop: RMS calculation of the cantilever amplitude over 100 ms. For a cantilever with a resonance frequency of 5 kHz, this would correspond to averaging over 500 oscillations. Bottom loop: A PID that outputs a control value proportional to how far the oscillation amplitude deviates from a setpoint value.

phase and minimizing this RMS (or *'dissipation'*). The frequency is also plotted below.

The damping circuit is activated with the *'Damp'* button, and the damping scalar is set with the *'desired damping gain'* field. The damped quality factor is determined with a ringdown measurement.
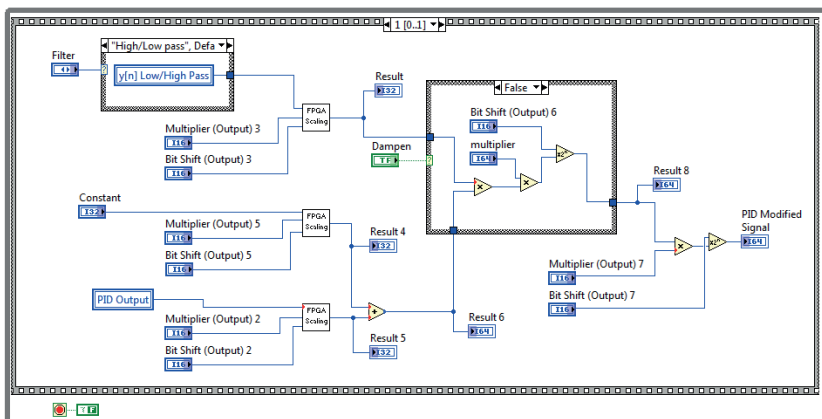
FIGURE B.19: The block diagram for the self oscillation calculation. This section is displayed in the *'Feedback Loop'* section of the front panel in figure B.17. The amplitude PID output can be added to a constant to produce an offset, but this is typically unused and set to 1. This product is then multiplied by the phase shifted cantilever motion, and has an optional scaling factor (unused). The final result is called *'PID Modified Signal'*.
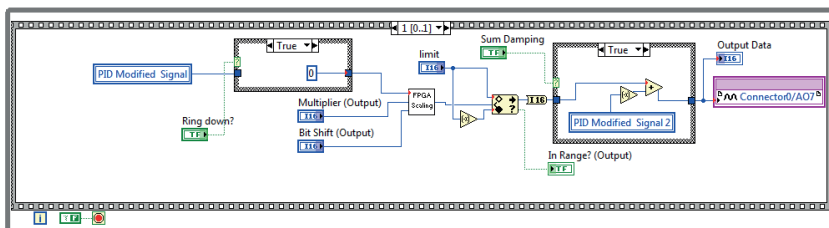
FIGURE B.20: Output loop of the self oscillation amplitude. An optional scaling value is available, but is not used.
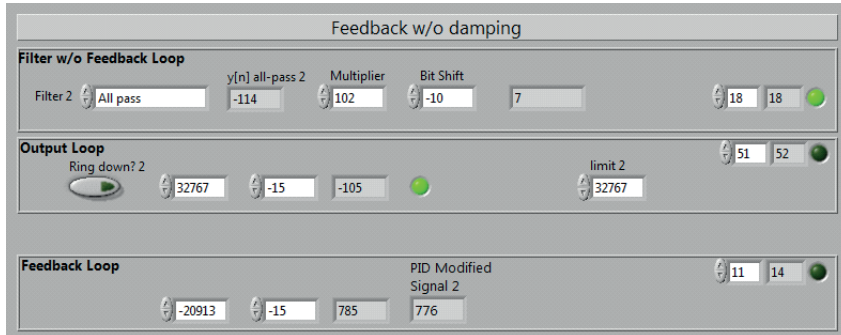
FIGURE B.21: Top loop: The input to the damping circuit is the signal from the all-pass filter. A scaling factor could be applied at this point, but it is set to 1. Bottom loop: A negative scaling factor is applied to the signal, and then output. Generally the AC gain of the cantilever signal is set high enough such that this scaling factor is between 0 and -1.
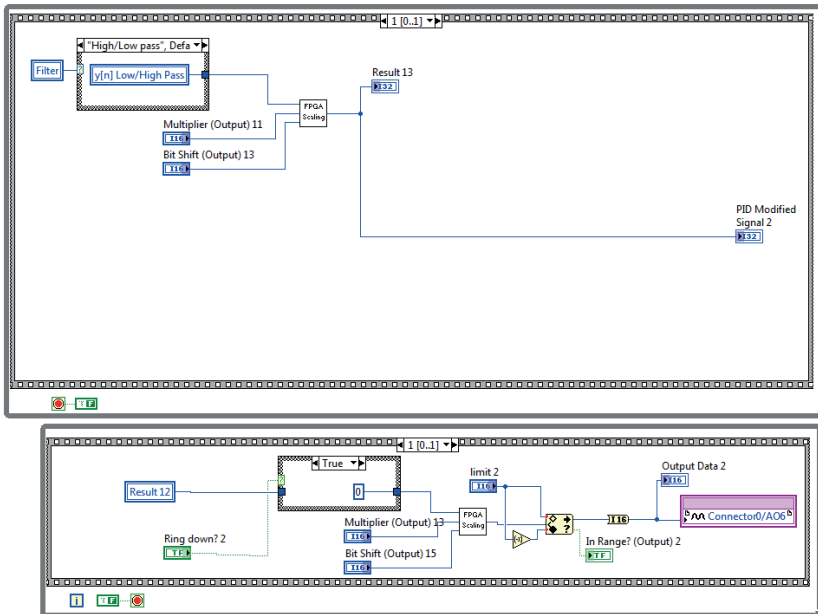
FIGURE B.22: FPGA damping feedback loop wiring diagram. The top loop selects the phase shifted signal from the all-pass filter, and the bottom loop outputs the signal with a scaling factor that applies an inversion.
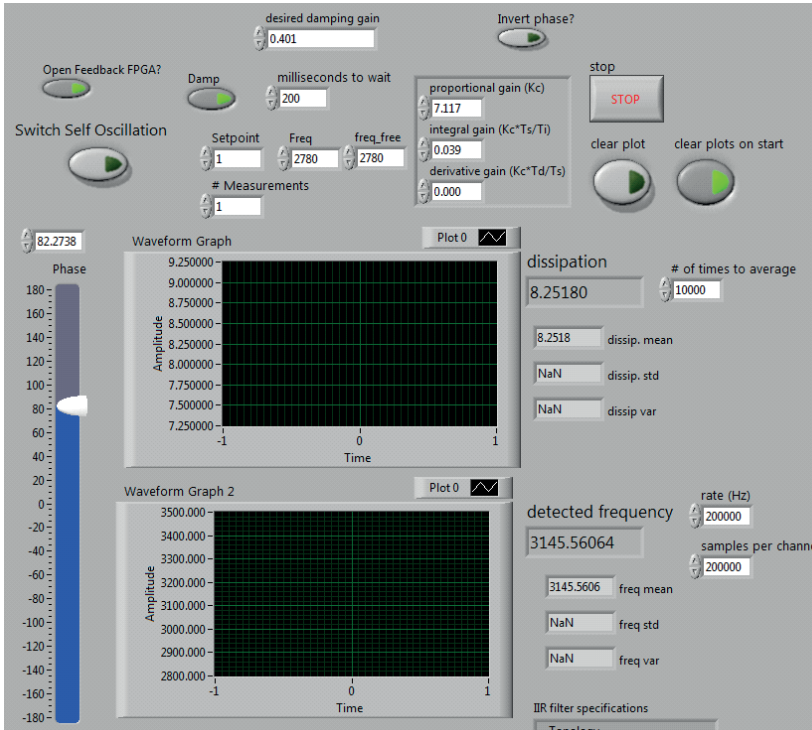
FIGURE B.23: Self oscillation and damping calibration VI front panel.

Appendix C

Supplementary

C.1 Approach curve over superconductor

Figure C.1 shows an approach curve over a superconducting thin film. The cantilever had an InAs nanowire with a 60 nm thick layer of thermally evaporated CaF_2. The superconductor was a $\sim$100 nm tungsten compound $W(CO)_6$ thin film deposited with a focused ion beam over a gold stripline. The quality factor is virtually unaffected until $\sim$10 nm from the surface. The cantilever frequency is also barely shifted until $\sim$15 nm from the surface. This is in good agreement with the reduction of electronic friction from a $1/z$ dependence with metals to $1/z^4$ with superconductors [56].
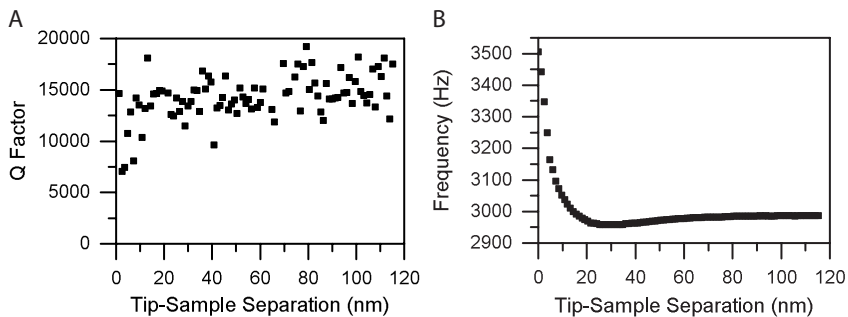
FIGURE C.1: An approach curve over a superconducting surface with an InAs nanowire and a 60 nm layer of calcium fluoride..

C.2 Adiabatic simulation comparison

Figure C.2 shows the agreement between the linear/trapezoid and hyperbolic secant adiabatic pulses. The data form figure 4.13 is plotted with the simulation data from figure 4.15 overlaid as a 'multiply' layer. The adiabatic regime of the simulation is highlighted by a red line, which was matched to the data underneath.

This comparison provides a means of characterizing the RF power of the stripline. This is typically performed by measuring a Rabi oscillation, however the nuclear spin T_1 lifetime tends to be too short. Since the FM deviation is precisely known in both simulation and data, the only free parameter is the x-axis.

C.3 Cantilever mode coupling

Figure C.3 shows mechanical coupling between the fundamental mode (6.5 kHz) and the second flexural mode (150, 870 kHz). The cantilever was
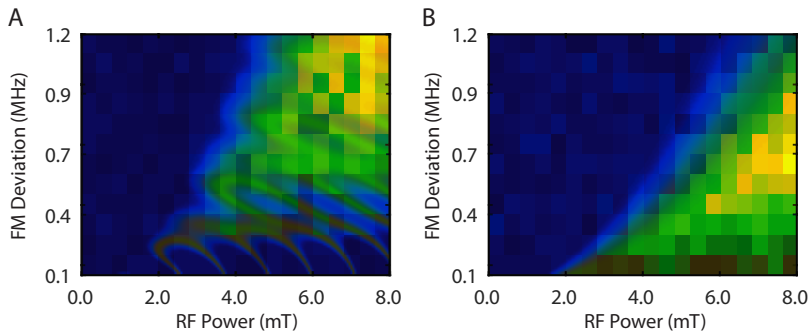
FIGURE C.2: The simulation is displayed over the data as a 'multiply' layer. The x-axis was scaled until the slope of data matched.

positioned $\sim$20 nm above a gold surface, and the z-piezo was oscillated with an amplitude of $\sim$5 nm. This z-oscillation was found to modulate the cantilever spring constant, creating a parametric drive (or pump frequency). The z-piezo oscillation frequency is plotted along the x-axis of the figure. Each data point is the result of 30 ringdown curves, which use an excitation frequency (to the cantilever piezo) plotted along the y-axis. We find our results to agree well with previously reported findings with a doubly clamped beam [102].
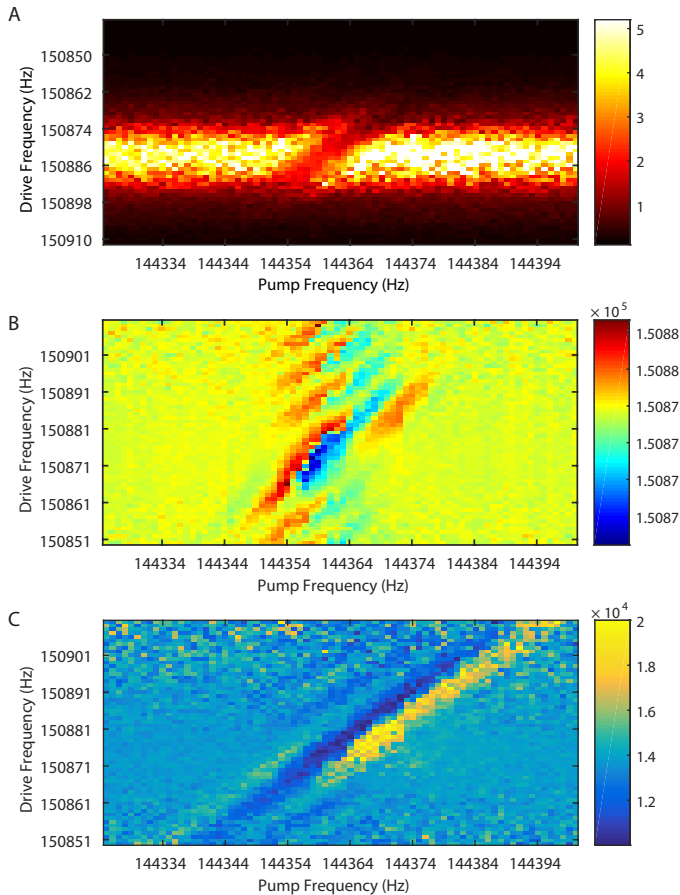
FIGURE C.3: (a) The amplitude (in volts) of the second flexural mode
due to a drive tone. When the z-piezo frequency matched the difference
frequency (144, 354 Hz), then the higher mode was harder to excite and
therefore effectively damped. (b) Plot of the ringdown frequency for
each measurement. The ringdown frequency was 150, 870 Hz, unless
the pump frequency was close to 144, 354 Hz. (c) The quality factor
is also affected within this frequency range. The quality factor of the
fundamental mode was damped from 12000 to 3000. The cantilever
was not mass loaded.

Bibliography

[1] S. Worthy, "High resolution computed tomography of the lungs,"
BMJ, vol. 310, pp. 616+, Mar. 1995.

[2] M. Adhi and J. S. Duker, "Optical coherence tomography–current
and future applications.," *Current opinion in ophthalmology*,
vol. 24, pp. 213–221, May 2013.

[3] P. Mansfield, "Snapshot magnetic resonance imaging (nobel
lecture)," *Angew. Chem.-Int. Edit. Engl.*, vol. 43, p. 5456, 2004.

[4] R. Henson, "Introduction to functional magnetic resonance
imaging: Principles and techniques," *Brain*, vol. 126, p. 2110, Sept.
2003.

[5] P. Glover and P. Mansfield, "Limits to magnetic resonance
microscopy," *Rep. Prog. Phys.*, vol. 65, p. 1489, 2002.

[6] L. Ciobanu, D. A. Seeber, and C. H. Pennington, "3d mr
microscopy with resolution 3.7 μm by 3.3 μm by 3.3 μm," *J.
Magn. Reson.*, vol. 158, p. 178, 2002.

[7] S. Raman, O. F. Lange, P. Rossi, M. Tyka, X. Wang, J. Aramini,
G. Liu, T. A. Ramelot, A. Eletsky, T. Szyperski, M. A. Kennedy,

J. Prestegard, G. T. Montelione, and D. Baker, "NMR Structure Determination for Larger Proteins Using Backbone-Only Data," *Science*, vol. 327, pp. 1014–1018, Feb. 2010.

[8] S. Subramaniam, "Bridging the imaging gap: visualizing subcellular architecture with electron tomography," *Current Opinion in Microbiology*, vol. 8, p. 316, 2005.

[9] L. Schermelleh, R. Heintzmann, and H. Leonhardt, "A guide to super-resolution fluorescence microscopy," *The Journal of Cell Biology*, vol. 190, pp. 165–175, July 2010.

[10] D. Lyumkis, J.-P. Julien, N. de Val, A. Cupo, C. S. Potter, P.-J. Klasse, D. R. Burton, R. W. Sanders, J. P. Moore, B. Carragher, I. A. Wilson, and A. B. Ward, "Cryo-EM Structure of a Fully Glycosylated Soluble Cleaved HIV-1 Envelope Trimer," *Science*, vol. 342, pp. 1484–1490, Dec. 2013.

[11] S. L. Reichow, K. V. Korotkov, W. G. J. Hol, and T. Gonen, "Structure of the cholera toxin secretion channel in its closed state," *Nat Struct Mol Biol*, vol. 17, pp. 1226–1232, Oct. 2010.

[12] J. Frank, M. Radermacher, P. Penczek, J. Zhu, Y. Li, M. Ladjadj, and A. Leith, "SPIDER and WEB: Processing and Visualization of Images in 3D Electron Microscopy and Related Fields," *Journal of Structural Biology*, vol. 116, pp. 190–199, Jan. 1996.

[13] J. A. Sidles, "Noninductive detection of single-proton magnetic resonance," *Appl. Phys. Lett.*, vol. 58, p. 2854, 1991.

[14] C. L. Degen, "Scanning magnetic field microscope with a diamond single-spin sensor," *Appl. Phys. Lett.*, vol. 92, p. 243111, 2008.

[15] M. Poggio and C. L. Degen, "Force-detected nuclear magnetic resonance: Recent advances and future challenges," *Nanotechnology*, vol. 21, p. 342001, 2010.

[16] C. L. Degen, M. Poggio, H. J. Mamin, and D. Rugar, "Role of spin noise in the detection of small ensembles of nuclear spins," *Phys. Rev. Lett.*, vol. 99, p. 250601, 2007.

[17] H. J. Mamin, T. H. Oosterkamp, M. Poggio, C. L. Degen, C. T. Rettner, and D. Rugar, "Isotope-selective detection and imaging of organic nanolayers," *Nano. Lett.*, vol. 9, p. 3020, 2009.

[18] H. J. Mamin, M. Kim, M. H. Sherwood, C. T. Rettner, K. Ohno, D. D. Awschalom, and D. Rugar, "Nanoscale nuclear magnetic resonance with a nitrogen-vacancy spin sensor," *Science*, vol. 339, pp. 557–560, 2013.

[19] T. Staudacher, F. Shi, S. Pezzagna, J. Meijer, J. Du, C. A. Meriles, F. Reinhard, and J. Wrachtrup, "Nuclear magnetic resonance spectroscopy on a (5-nanometer)(3) sample," *Science*, vol. 339, pp. 561–563, 2013.

[20] M. Loretz, S. Pezzagna, J. Meijer, and C. L. Degen, "Nanoscale nuclear magnetic resonance with a 1.9-nm-deep nitrogen-vacancy sensor," *Appl. Phys. Lett.*, vol. 104, p. 33102, 2014.

[21] C. Muller, X. Kong, J. M. Cai, K. Melentijevic, A. Stacey, M. Markham, D. Twitchen, J. Isoya, S. Pezzagna, J. Meijer, J. F. Du, M. B. Plenio, B. Naydenov, L. P. McGuinness, and F. Jelezko, "Nuclear magnetic resonance spectroscopy with single spin sensitivity," *Nature Comm.*, vol. 5, pp. 4703–4703, 2014.

[22] C. L. Degen, M. Poggio, H. J. Mamin, and D. Rugar, "Nuclear spin relaxation induced by a mechanical resonator," *Phys. Rev. Lett.*, vol. 100, p. 137601, 2008.

[23] S. S. Zalesskiy, E. Danieli, B. Blümich, and V. P. Ananikov, "Miniaturization of NMR Systems: Desktop Spectrometers, Microcoil Spectroscopy, and " NMR on a Chip" for Chemistry, Biochemistry, and Industry," *Chem. Rev.*, vol. 114, pp. 5641–5694, June 2014.

[24] A. Kumar and P. A. Bottomley, "Optimizing the intrinsic signal-to-noise ratio of MRI strip detectors," *Magn. Reson. Med.*, vol. 56, pp. 157–166, July 2006.

[25] A. G. Webb, "Radiofrequency microcoils for magnetic resonance imaging and spectroscopy," *Journal of Magnetic Resonance*, vol. 229, pp. 55–66, Apr. 2013.

[26] S. C. Lee, K. Kim, J. Kim, S. Lee, J. H. Yi, S. W. Kim, K. S. Ha, and C. Cheong, "One micrometer resolution NMR microscopy.," *Journal of magnetic resonance (San Diego, Calif. : 1997)*, vol. 150, pp. 207–213, June 2001.

[27] L. Ciobanu, A. G. Webb, and C. H. Pennington, "Magnetic resonance imaging of biological cells," *Progress in Nuclear Magnetic Resonance Spectroscopy*, vol. 42, pp. 69–93, Aug. 2003.

[28] S.-C. C. Lee, K. Kim, J. Kim, J. H. H. Yi, S. Lee, and C. Cheong, "MR microscopy of micron scale structures.," *Magnetic resonance imaging*, vol. 27, pp. 828–833, July 2009.

[29] V. Badilita, K. Kratt, N. Baxan, M. Mohmmadzadeh, T. Burger, H. Weber, D. Elverfeldt, J. Hennig, J. G. Korvink, and

U. Wallrabe, "On-chip three dimensional microcoils for MRI at the microscale," *Lab Chip*, vol. 10, no. 11, pp. 1387–1390, 2010.

[30] J. A. Sidles and D. Rugar, "Signal-to-noise ratios in inductive and mechanical detection of magnetic resonance.," *Physical review letters*, vol. 70, pp. 3506–3509, May 1993.

[31] Y. Tao, J. M. Boss, B. A. Moores, and C. L. Degen, "Single crystal diamond nanomechanical resonators with quality factors exceeding one million," *Nature Comm.*, vol. 5, p. 0, 2014.

[32] D. Rugar, H. J. Mamin, M. H. Sherwood, M. Kim, C. T. Rettner, K. Ohno, and D. D. Awschalom, "Proton magnetic resonance imaging using a nitrogen–vacancy spin sensor," *Nature Nanotechnology*, vol. 10, pp. 120–124, Dec. 2014.

[33] M. S. Grinolds, M. Warner, K. de Greve, Y. Dovzhenko, L. Thiel, R. L. Walsworth, S. Hong, P. Maletinsky, and A. Yacoby, "Subnanometre resolution in three-dimensional magnetic resonance imaging of individual dark spins," *Nat. Nano.*, vol. 9, pp. 279–284, 2014.

[34] K. Y. Yasumura, T. D. Stowe, E. M. Chow, T. Pfafman, T. W. Kenny, B. C. Stipe, and D. Rugar, "Quality factors in micron- and submicron-thick cantilevers," *J. Microelectromech. Syst.*, vol. 9, p. 117, 2000.

[35] B. W. Chui, Y. Hishinuma, R. Budakian, H. J. Mamin, T. W. Kenny, and D. Rugar *Technical Digest of the 12th International Conference on Solid-State Sensors and Actuators (Transducers'03) (IEEE, Piscataway, 2003), p. 1120.*, p. 0.

[36] H. J. Mamin and D. Rugar, "Sub-attonewton force detection at millikelvin temperatures," *Appl. Phys. Lett.*, vol. 79, p. 3358, 2001.

[37] S. Syrenova, C. Wadell, and C. Langhammer, "Shrinking-Hole Colloidal Lithography: Self-Aligned Nanofabrication of Complex Plasmonic Nanoantennas," *Nano Letters*, vol. 14, pp. 2655–2663, May 2014.

[38] H. J. Mamin, M. H. Sherwood, and D. Rugar, "Detecting external electron spins using nitrogen-vacancy centers," *Phys. Rev. B*, vol. 86, p. 195422, 2012.

[39] M. Poggio, C. L. Degen, C. T. Rettner, H. J. Mamin, and D. Rugar, "Nuclear magnetic resonance force microscopy with a microwire rf source," *Appl. Phys. Lett.*, vol. 90, p. 263111, 2007.

[40] W. Zhang and K. L. Turner, "Pressure-dependent damping characteristics of microsilicon beam resonators for different resonant modes," in *Sensors, 2005 IEEE*, pp. 4 pp.+, IEEE, Oct. 2005.

[41] A. N. Cleland, *Foundations of Nanomechanics*. Berlin, Heidelberg: Springer Berlin Heidelberg, 2003.

[42] M. Imboden and P. Mohanty, "Dissipation in nanoelectromechanical systems," *Physics Reports*, vol. 534, p. 89, 2014.

[43] T. D. Stowe, K. Yasumura, T. W. Kenny, D. Botkin, K. Wago, and D. Rugar, "Attonewton force detection using ultrathin silicon cantilevers," *Appl. Phys. Lett.*, vol. 71, pp. 288–290, 1997.

[44] T. R. Albrecht, P. Grütter, D. Horne, and D. Rugar, "Frequency modulation detection using highQ cantilevers for enhanced force microscope sensitivity," *Journal of Applied Physics*, vol. 69, pp. 668–673, Jan. 1991.

[45] D. Rugar, B. C. Stipe, H. J. Mamin, C. S. Yannoni, T. D. Stowe, K. Y. Yasumura, and T. W. Kenny, "Adventures in attonewton force detection," *Applied Physics A: Materials Science & Processing*, vol. 72, pp. S3–S10–S10, Mar. 2001.

[46] D. P. Weber, D. Rüffer, A. Buchter, F. Xue, E. Russo-Averchi, R. Huber, P. Berberich, J. Arbiol, Fontcuberta, D. Grundler, and M. Poggio, "Cantilever Magnetometry of Individual Ni Nanotubes," *Nano Lett.*, vol. 12, pp. 6139–6144, Dec. 2012.

[47] A. Mehlin, F. Xue, D. Liang, H. F. Du, M. J. Stolt, S. Jin, M. L. Tian, and M. Poggio, "Stabilized Skyrmion Phase Detected in MnSi Nanowires by Dynamic Cantilever Magnetometry," *Nano Lett.*, vol. 15, pp. 4839–4844, July 2015.

[48] S. Ghaffari, S. A. Chandorkar, S. Wang, E. J. Ng, C. H. Ahn, V. Hong, Y. Yang, and T. W. Kenny, "Quantum Limit of Quality Factor in Silicon Micro and Nano Mechanical Resonators," *Scientific Reports*, vol. 3, Nov. 2013.

[49] O. Ergincan, G. Palasantzas, and B. J. Kooi, "Influence of surface modification on the quality factor of microresonators," *Physical Review B*, vol. 85, May 2012.

[50] H. Hosaka, K. Itao, and S. Kuroda, "Damping characteristics of beam-shaped micro-oscillators," *Sensors and Actuators A: Physical*, vol. 49, pp. 87–95, June 1995.

[51] A. Gaidarzhy, M. Imboden, P. Mohanty, J. Rankin, and B. W. Sheldon, "High quality factor gigahertz frequencies in nanomechanical diamond resonators," *Appl. Phys. Lett.*, vol. 91, p. 203503, 2007.

[52] T. V. Roszhart, "The effect of thermoelastic internal friction on the Q of micromachined silicon resonators," in *Solid-State Sensor and Actuator Workshop, 1990. 4th Technical Digest., IEEE*, pp. 13–16, IEEE, June 1990.

[53] Q. P. Unterreithmeier, E. M. Weig, and J. P. Kotthaus, "Universal transduction scheme for nanomechanical systems based on dielectric forces," *Nature*, vol. 458, pp. 1001–1004, Apr. 2009.

[54] S. Morita, F. J. Giessibl, E. Meyer, and R. Wiesendanger, eds., *Noncontact Atomic Force Microscopy*. Cham: Springer International Publishing, 2015.

[55] S. Lekkala, J. A. Marohn, and R. F. Loring, "Electric force microscopy of semiconductors: Theory of cantilever frequency fluctuations and noncontact friction," *The Journal of Chemical Physics*, vol. 139, pp. 184702+, Nov. 2013.

[56] M. Kisiel, E. Gnecco, U. Gysin, L. Marot, S. Rast, and E. Meyer, "Suppression of electronic friction on Nb films in the superconducting state," *Nature Materials*, vol. 10, pp. 119–122, Jan. 2011.

[57] B. C. Stipe, H. J. Mamin, T. D. Stowe, T. W. Kenny, and D. Rugar, "Noncontact friction and force fluctuations between closely spaced bodies.," *Physical review letters*, vol. 87, Aug. 2001.

[58] S. Kuehn, R. F. Loring, and J. A. Marohn, "Dielectric fluctuations and the origins of noncontact friction," *Phys. Rev. Lett.*, vol. 96, p. 156103, 2006.

[59] R. García, "Dynamic atomic force microscopy methods," *Surface Science Reports*, vol. 47, pp. 197–301, Sept. 2002.

[60] J. M. Nichol, E. R. Hemesath, L. J. Lauhon, and R. Budakian, "Nanomechanical detection of nuclear magnetic resonance using a silicon nanowire oscillator," *Phys. Rev. B*, vol. 85, p. 054414, 2012.

[61] T. D. Stowe, T. W. Kenny, D. J. Thomson, and D. Rugar, "Silicon dopant imaging by dissipation force microscopy," *Applied Physics Letters*, vol. 75, pp. 2785–2787, Nov. 1999.

[62] S. Maier, O. Pfeiffer, T. Glatzel, E. Meyer, T. Filleter, and R. Bennewitz, "Asymmetry in the reciprocal epitaxy of NaCl and KBr," *Physical Review B*, vol. 75, May 2007.

[63] F. J. Giessibl, S. Hembacher, H. Bielefeldt, and J. Mannhart, "Subatomic features on the silicon (111)-(7x7) surface observed by atomic force microscopy," *Science*, vol. 289, pp. 422–425, 2000.

[64] C. P. Slichter, *Principles of Magnetic Resonance, 3rd edition.* Berlin: Springer, 1990.

[65] B. E. Herzog, D. Cadeddu, F. Xue, P. Peddibhotla, and M. Poggio, "Boundary between the thermal and statistical polarization regimes in a nuclear spin ensemble," *Appl. Phys. Lett.*, vol. 105, p. 043112, 2014.

[66] F. Bloch, "Nuclear induction," *Phys. Rev.*, vol. 70, p. 460, 1946.

[67] T. Sleater, E. L. Hahn, C. Hilbert, and J. Clarke, "Nuclear-spin noise.," *Physical review letters*, vol. 55, pp. 1742–1745, Oct. 1985.

[68] M. A. McCoy and R. R. Ernst, "Nuclear spin noise at room temperature," *Chemical Physics Letters*, vol. 159, pp. 587–593, July 1989.

[69] E. M. Purcell, H. C. Torrey, and R. V. Pound, "Resonance Absorption by Nuclear Magnetic Moments in a Solid," *Physical Review*, vol. 69, pp. 37–38, Jan. 1946.

[70] M. Garwood and L. DelaBarre, "The return of the frequency sweep: designing adiabatic pulses for contemporary NMR.," *Journal of magnetic resonance (San Diego, Calif. : 1997)*, vol. 153, pp. 155–177, Dec. 2001.

[71] D. Rugar, R. Budakian, H. J. Mamin, and B. W. Chui, "Single spin detection by magnetic resonance force microscopy," *Nature*, vol. 430, p. 329, 2004.

[72] R. Budakian, H. J. Mamin, B. W. Chui, and D. Rugar, "Creating order from random fluctuations in small spin ensembles," *Science*, vol. 307, p. 408, 2005.

[73] C. L. Degen, M. Poggio, H. J. Mamin, C. T. Rettner, and D. Rugar, "Nanoscale magnetic resonance imaging," *Proc. Nat. Acad. Sci. U.S.A.*, vol. 106, p. 1313, 2009.

[74] J. Baum, R. Tycko, and A. Pines, "Broadband and adiabatic inversion of a two-level system by phase-modulated pulses.," *Physical review. A*, vol. 32, pp. 3435–3447, Dec. 1985.

[75] B. A. Moores, A. Eichler, Y. Tao, H. Takahashi, P. Navaretti, and C. L. Degen, "Accelerated nanoscale magnetic resonance imaging through phase multiplexing," *Applied Physics Letters*, vol. 106, pp. 213101+, May 2015.

[76] J. M. Nichol, T. R. Naibert, E. R. Hemesath, L. J. Lauhon, and R. Budakian, "Nanoscale fourier-transform magnetic resonance imaging," *Phys. Rev. X*, vol. 3, p. 031016, 2013.

[77] A. Kumar, D. Welti, and R. R. Ernst, "Nmr fourier zeugmatography," *J. Mag. Res.*, vol. 18, pp. 69–83, 1975.

[78] L. Bolinger and J. S. Leigh, "Hadamard spectroscopic imaging (hsi) for multivolume localization," *J. Mag. Res.*, vol. 80, pp. 162–167, 1988.

[79] K. W. Eberhardt, C. L. Degen, and B. H. Meier, "Fast magnetic resonance force microscopy with hadamard encoding," *Phys. Rev. B*, vol. 76, p. 180405, 2007.

[80] T. H. Oosterkamp, M. Poggio, C. L. Degen, H. J. Mamin, and D. Rugar, "Frequency domain multiplexing of force signals with application to magnetic resonance force microscopy," *Appl. Phys. Lett.*, vol. 96, p. 083107, 2010.

[81] J. Kempf and J. A. Marohn, "Nanoscale fourier-transform imaging with magnetic resonance force microscopy," *Phys. Rev. Lett.90,*, vol. 087601, 2003.

[82] See supplemental material at [URL] for details concerning the measurement technique, error propagation, and noise analysis.

[83] H. J. Mamin, C. T. Rettner, M. H. Sherwood, L. Gao, and D. Rugar, "High field-gradient dysprosium tips for magnetic resonance force microscopy," *Applied Physics Letters*, vol. 100, no. 1, pp. –, 2012.

[84] S. Kotler, N. Akerman, Y. Glickman, A. Keselman, and R. Ozeri, "Single-ion quantum lock-in amplifier," *Nature*, vol. 473, pp. 61–65, 2011.

[85] A. Harris, G. Cardone, D. C. Winkler, J. B. Heymann, M. Brecher, J. M. White, and A. C. Steven, "Influenza virus pleiomorphy

characterized by cryoelectron tomography," *Proceedings of the National Academy of Sciences*, vol. 103, pp. 19123–19127, Dec. 2006.

[86] W. H. Organization, "Influenza (Seasonal) Fact sheet." <http://www.who.int/mediacentre/factsheets/fs211/en/>, 2014. [Online; accessed 20-July-2015].

[87] J. K. Taubenberger and D. M. Morens, "The pathology of influenza virus infections.," *Annual review of pathology*, vol. 3, no. 1, pp. 499–522, 2008.

[88] S. Herfst, E. J. A. Schrauwen, M. Linster, S. Chutinimitkul, E. de Wit, V. J. Munster, E. M. Sorrell, T. M. Bestebroer, D. F. Burke, D. J. Smith, G. F. Rimmelzwaan, A. D. M. E. Osterhaus, and R. A. M. Fouchier, "Airborne Transmission of Influenza A/H5N1 Virus Between Ferrets," *Science*, vol. 336, pp. 1534–1541, June 2012.

[89] H. Hu, K. Nigmatulina, and P. Eckhoff, "The scaling of contact rates with population density for the infectious disease models," *Mathematical Biosciences*, vol. 244, pp. 125–134, Aug. 2013.

[90] T. Noda, H. Sagara, A. Yen, A. Takada, H. Kida, R. H. Cheng, and Y. Kawaoka, "Architecture of ribonucleoprotein complexes in influenza A virus particles," *Nature*, vol. 439, pp. 490–492, Jan. 2006.

[91] D. S. Goodsell, "Hemagglutinin," *RCSB Protein Data Bank*, Apr. 2006.

[92] Y. A. Shtyrya, L. V. Mochalova, and N. V. Bovin, "Influenza virus neuraminidase: structure and function.," *Acta naturae*, vol. 1, pp. 26–32, July 2009.

[93] R. J. Russell, P. S. Kerry, D. J. Stevens, D. A. Steinhauer, S. R. Martin, S. J. Gamblin, and J. J. Skehel, "Structure of influenza hemagglutinin in complex with an inhibitor of membrane fusion," *Proceedings of the National Academy of Sciences*, vol. 105, pp. 17736–17741, Nov. 2008.

[94] N. Sriwilaijaroen and Y. Suzuki, "Molecular basis of the structure and function of H1 hemagglutinin of influenza virus.," *Proceedings of the Japan Academy. Series B, Physical and biological sciences*, vol. 88, no. 6, pp. 226–249, 2012.

[95] M. Throsby, E. van den Brink, M. Jongeneelen, L. L. M. Poon, P. Alard, L. Cornelissen, A. Bakker, F. Cox, E. van Deventer, Y. Guan, J. Cinatl, J. Meulen, I. Lasters, R. Carsetti, M. Peiris, J. de Kruif, and J. Goudsmit, "Heterosubtypic Neutralizing Monoclonal Antibodies Cross-Protective against H5N1 and H1N1 Recovered from Human IgM+ Memory B Cells," *PLoS ONE*, vol. 3, pp. e3942+, Dec. 2008.

[96] D. C. Ekiert, G. Bhabha, M.-A. A. Elsliger, R. H. Friesen, M. Jongeneelen, M. Throsby, J. Goudsmit, and I. A. Wilson, "Antibody recognition of a highly conserved influenza virus epitope.," *Science (New York, N.Y.)*, vol. 324, pp. 246–251, Apr. 2009.

[97] D. Greiff, H. Blumenthal, M. Chiga, and H. Pinkerton, "The effects on biological materials of freezing and drying by vacuum sublimation. II. Effect on influenza virus.," *The Journal of experimental medicine*, vol. 100, pp. 89–101, July 1954.

[98] H. C. Overweg, A. M. J. den Haan, H. J. Eerkens, P. F. A. Alkemade, A. L. La Rooij, R. J. C. Spreeuw, L. Bossoni, and T. H. Oosterkamp, "Probing the magnetic moment of FePt micromagnets

prepared by focused ion beam milling," *Applied Physics Letters*, vol. 107, pp. 072402+, Aug. 2015.

[99] B. B. Hsu, S. Y. Wong, P. T. Hammond, J. Chen, and A. M. Klibanov, "Mechanism of inactivation of influenza viruses by immobilized hydrophobic polycations," *Proceedings of the National Academy of Sciences*, vol. 108, pp. 61–66, Jan. 2011.

[100] K. Gerasopoulos, M. McCarthy, E. Royston, J. N. Culver, and R. Ghodssi, "Nanostructured nickel electrodes using the Tobacco mosaic virus for microbattery applications," *Journal of Micromechanics and Microengineering*, vol. 18, pp. 104003+, Oct. 2008.

[101] N. Korkmaz, "Recombinant bacteriophages as gold binding bio-templates.," *Colloids and surfaces. B, Biointerfaces*, vol. 112, pp. 219–228, Dec. 2013.

[102] I. Mahboob, K. Nishiguchi, H. Okamoto, and H. Yamaguchi, "Phonon-cavity electromechanics," *Nat Phys*, vol. 8, pp. 387–392, May 2012.

Bradley A. Moores, M.Sc.

mooresb@phys.ethz.ch | Department of Physics, Otto Stern Weg 1, 8093 Zürich, Switzerland

Education

- **Candidate for Doctor of Philosophy**, Physics

    ETH Zurich, Zurich, Switzerland   2011 – pres.
      Supervisor: Prof. Christian L. Degen

    Massachusetts Institute of Technology (MIT), Cambridge, MA   2010 – 2011
      Supervisor: Prof. Christian L. Degen

- **Master of Science**, Physics

    University of Waterloo, Waterloo, Canada   2008 – 2010
      Supervisor: Prof. Zoya Leonenko (University of Waterloo)
      Co-supervisor: Prof. Lukas M. Eng (Technische Universität Dresden)
      Thesis: Scanning Probe Microscopy Methods to Study Electrostatic Properties
      within Biosystems

- **Bachelor of Science**, Honours Co-operative Physics

    University of Waterloo, Waterloo, Canada   2003 – 2008
      Focus on Biophysics and Computer Science
      Thesis: Binding of amyloid peptides to charged model surfaces

Research Highlights

- Built a Magnetic Resonance Force Microscope (MRFM) capable of 5 nm spatial resolution in 3D

- Developed phase multiplexing protocol for rapid nano-magnetic resonance imaging acquisition

- Imaged samples in 3D including an InAs nanowire and an influenza virus

- Programmed FPGA cantilever/laser feedback controller, FPGA data acquisition protocol for MRFM signals, radiofrequency pulse programs, nanopositioning, and analysis programs

- Characterized surface topography with Atomic Force Microscopy (AFM) and electrical characterization with Kelvin Probe Force Microscopy (KPFM) of biological samples

Awards

- Wiley Prize: Magnetic Resonance in Chemistry Award for researchers under 40 (€500)
  Zurich, Switzerland. Jun 2014.

- Natural Sci. and Eng. Research Council of Canada (NSERC) Postgraduate Scholarship ($63,000)
  Ottawa, Canada. Dec 2010.

- Waterloo Institute for Nanotechnology Fellowship ($10,000)
  Waterloo, Canada. Jan 2010.

- Best Poster, Guelph-Waterloo Physics Institute Poster Session
  Guelph, Canada. Jul 2009.

- 2nd Place Poster, 7th International Symposium on Scanning Probe Microscopy in Life Sciences
  Berlin, Germany. Oct 2008.

- University of Waterloo Graduate Entrance Scholarship ($5,000)
  Waterloo, Canada. Sept 2008.

Research & Work Experience

Ph.D. Student, Chemistry & Physics Departments   2010 – 2015
MIT, Cambridge USA & ETH Zurich, Switzerland
- Built a low temperature (4 Kelvin), high field (6 Tesla) Magnetic Resonance Force Microscope (MRFM) with cantilever detection by laser interferometry
- Programmed feedback controllers, data acquisition programs, and analysis programs using LabVIEW and LabVIEW FPGA
- Developed a multiplexing protocol capable of simultaneously measuring at least 6 statistically polarized nuclear spin signals
- Demonstrated spatial resolution better than 5 nm with nanowire and virus samples
- Developed techniques for attaching samples to micron sized cantilevers
- Simulated experimental conditions using Comsol and Matlab
- Designed and modified high vacuum / low temperature parts using Solids Works

Chief Technical Officer, Startup Company   2012 – 2013
AppParental, Zurich, Switzerland
- Programmed a Java based Android prototype application
- Developed backend server and website interface
- Delivered presentations to potential investors

Masters Student, Physics Department   2008 – 2010
University of Waterloo, Waterloo, Canada
- Modified an Atomic Force Microscope (AFM) to image in Non-Contact mode and Frequency Modulation Kelvin Probe Force Microscopy (KPFM)
- Characterized imaging capabilities of several KPFM methods
- Analyzed lipid monolayer and membrane samples using AFM and KPFM

Research Assistant, Integrative Biology   May – Sept
Hospital for Sick Children, Toronto, Canada   2007
- Interfaced a CTF magnetoencephalography phantom with Matlab and LabVIEW
- Simulated magnetic dipoles distributed over a cortical surface using Matlab
- Modified beamforming algorithm (C/C++) to incorporate spatially correlated sources

GUI Developer, Medical Imaging   May – Sept
Princess Margaret Hospital, Toronto, Canada   2007
- Developed a Matlab graphical user interface for analyzing dynamic contrast-enhanced magnetic resonance images

Research Assistant, Integrative Biology   Sept – Dec
Hospital for Sick Children, Toronto, Canada   2006
- Developed a Matlab program for analyzing functional magnetoencephalography data superimposed on structural magnetic resonance images

Applications Assistant, Research & Development   Sept – Dec
Sensors & Software Inc, Mississauga, Canada   2005
- Performed field and lab testing of ground penetrating radar and GPS equipment
- Developed software to update and manipulate acquired data

Simulation Programmer, Physics Department   Jan – Apr
University of Waterloo, Waterloo, Canada   2005
- Programmed condensed matter Monte Carlo simulations using C++ and Java

Journal Publications

2015   Accelerated nanoscale magnetic resonance imaging through phase multiplexing
BA Moores, A Eichler, Y Tao, H Takahashi, P Navaretti, CL Degen
App. Phys. Lett. **106**, 213101 (2015).

2014   Single-crystal diamond nanomechanical resonators with quality factors exceeding one million
Y Tao, JM Boss, BA Moores, CL Degen
Nature Comm. **5**, 3638 (2014).

2012   Spin properties of very shallow nitrogen vacancy defects in diamond
BK Ofori-Okai, S Pezzagna, K Chang, M Loretz, R Schirhagl, Y Tao, BA Moores, K Groot-Berning, J Meijer, CL Degen
Phys. Rev. B **86**, 081406 (2012).

Synthesis of polymer-like hydrogenated amorphous carbon by fs-pulsed laser induced plasma processing of solid hexane
MJ Wesolowski, B Moores, Z Leonenko, R Karimi, JH Sanderson, WW Duley
Plasma Proc. & Poly. **9** (7), 701-708 (2012).

2011   AFM-assisted fabrication of thiol SAM pattern with alternating quantified surface potential
B Moores, J Simons, S Xu, Z Leonenko
Nanoscale Res. Let. **6** (1), 185 (2011).

Effect of surfaces on amyloid fibril formation
B Moores, E Drolle, SJ Attwood, J Simons, Z Leonenko
PLoS One **6** (10), e25954 (2011).

Polyyne synthesis and amorphous carbon nano-particle formation by femtosecond irradiation of benzene
MJ Wesolowski, S Kuzmin, B Moores, B Wales, R Karimi, AA Zaidi, Z Leonenko, JH Sanderson, WW Duley
Carbon **49** (2), 625-630 (2011).

2010   Kelvin probe force microscopy in application to biomolecular films: Frequency modulation, amplitude modulation, and lift mode.
B Moores, F Hane, LM Eng, Z Leonenko
Ultramicroscopy **110** (6), 708-711 (2010).

Effect of cholesterol on electrostatics in lipid-protein films of pulmonary surfactant.
E Finot, Y Leonenko, B Moores, M Amrein, LM Eng, Z Leonenko
Langmuir **26** (3), 1929-1935 (2010).

2009   Effect of SP-C on surface potential distribution in pulmonary surfactant: Atomic force microscopy and Kelvin probe force microscopy study.
F Hane, B Moores, M Amrein, Z Leonenko.
Ultramicroscopy **109** (8), 968-973 (2009).

Other Publications

2015   Applied Physics Letters Front Cover
BA Moores, A Eichler, Y Tao, H Takahashi, P Navaretti, CL Degen
App. Phys. Lett. **106**, 213101 (2015).

2009   Ultramicroscopy Front Cover
F Hane, B Moores, M Amrein, Z Leonenko
Ultramicroscopy **109** (8), 968-973 (2009).

Conference Presentations

2015   Improving nano-MRI spatial resolution with phase multiplexing (talk)
B Moores, A Eichler, C Degen
APS March Meeting. San Antonio, USA.

2014   Chemically selective spin signal multiplexing with Magnetic Resonance Force Microscopy (talk, Wiley young scientist award)
B Moores, A Eichler, C Degen
Euromar: European Magnetic Resonance Conference. Zurich, Switzerland.

Implementation of NMR pulse sequences for Magnetic Resonance Force Microscopy (talk)
B Moores, A Eichler, C Degen
APS March Meeting. Denver, USA.

2013   Nano-MRI of single virus particles (poster)
B Moores, R Schirhagl, R Kammerer, P Navaretti, Y Tao, C Degen
Swiss NanoConvention. Basel, Switzerland.

2011   Ferromagnetic magnetometry with yittrium iron garnets (poster)
B Moores, C Degen
Black Forest Focus on Soft Matter 6: Mag. Res. Microsystems. Freiburg, Germany.

2010   Amyloid plaque formation on charged surfaces studied by AFM and KPFM (talk)
B Moores, Z Leonenko
37th Northeast Regional ACS Meeting. Potsdam, USA.

AFM and KPFM study of electrostatic interactions between amyloid peptides and modified thiol surfaces (talk)
B Moores, Z Leonenko
Chemical Biophysics Symposium. Toronto, Canada.

2009   Kelvin probe force microscopy in application to organic thin films and lipid monolayers (talk)
B Moores, F Hane, L Eng, Z Leonenko
Materials Research Society Fall Meeting. Boston, USA.

Kelvin probe force microscopy in application to lipid monolayers: frequency modulation, amplitude modulation, and hover mode KPFM (poster)
B Moores, L Eng, Z Leonenko
12th Int. Conf. on Non-Contact Atomic Force Microscopy. New Haven, USA.

Surface effects on amyloid fibril formation (poster)
B Moores, J Simons, Z Leonenko
Chemical Biophysics Symposium. Toronto, Canada.

2008   Formation of amyloid fibrils on model surfaces analyzed by non-contact AFM (poster)
B Moores, J Simons, Z Leonenko
7th International Symposium on SPM in Life Sciences. Berlin, Germany.

Formation of amyloid fibrils on model surfaces analyzed by non-contact AFM (poster)
B Moores, J Simons, Z Leonenko
11th Int. Conf. on Non-Contact Atomic Force Microscopy. Madrid, Spain.

Kinetics of amyloid fibrils analyzed by Atomic Force Microscopy (poster)
B Moores, Z Leonenko
Chemical Biophysics Symposium. Toronto, Canada.

2007   Medical imaging with Superconducting Quantum Interference Devices (SQUIDs) (talk)
B Moores, S Bells, D Cheyne
Canadian Undergraduate Physics Conference. Vancouver, Canada.